



The Scientific Institute for Advanced Training and Studies

**Experimental
and
Theoretical NANOTECHNOLOGY**

Vol. 4, No. 3, 2020

**Yarub Al-Douri
Editor-in-Chief**

e-ISSN: 2590-4132

Honorary Editor: M. Nayfeh (USA)

Editors

S. Abdullah (Malaysia)	H. Ekinçi (Turkey)	M-B Leptit (France)	T. E. Simos (Greece)
O. Alani (UK)	S. El-Safty (Japan)	J. Lui (USA)	J. Sing (Australia)
M. Ameri (Algeria)	Y. P. Feng (Singapore)	R. Nowak (Finland)	P. R. Somani (India)
N. E. Arif (Iraq)	L. Feo (Italy)	S. Radiman (Malaysia)	M. Tanemura (Japan)
V. K. Arora (USA)	M. Henni (UK)	M. V. Reddy (Singapore)	N. Tit (UAE)
M. Al-Jassim (USA)	A.Hui (USA)	A. H. Reshak (Czech Republic)	K. D. Verma (India)
S. Baroni (Italy)	M. R. Johan (Malaysia)	A. Rubio (Spain)	S. Wang (Singapore)
M. Bounoudina (Bahrain)	R. Jose (Malaysia)	M. Rusop (Malaysia)	J. Whitaker (USA)
Z. Cai (USA)	N. Joshi (USA)	P. Ruterana (France)	A.Zaoui (France)
A.Chaudhry (India)	A. H. Jumaa (Iraq)	P. Schwerdtfeger (New Zealand)	D. H. Zhang (Singapore)
N. E. Christensen (Denmark)	M. A. R. Khan (USA)	U.Schwingenschlo egl (Germany)	
D. Chua (Singapore)	R. Khenata (Algeria)		

Contact us

Experimental and Theoretical NANOTECHNOLOGY

Prof. Dr. Yarub Al-Douri; Editor-in-Chief : editor.etn@siats.co.uk

<http://etn.siats.co.uk>

**Experimental and Theoretical
NANOTECHNOLOGY**
<http://etn.sjats.co.uk/>

Experimental and Theoretical NANOTECHNOLOGY

VOL. 4, NO. 3, 2020

e-ISSN 2590-4132

2020

Experimental and Theoretical NANOTECHNOLOGY

Experimental and Theoretical NANOTECHNOLOGY is a multidisciplinary peer-reviewed international journal published four issues a year. It includes specialized research papers, short communications, reviews and selected conference papers in special issues on the characterization, synthesis, processing, structure and properties of different principles and applications of NANOTECHNOLOGY; with focus on advantageous achievements and applications for the specialists in engineering, chemistry, physics and materials science.

Experimental and Theoretical NANOTECHNOLOGY covers and publishes all aspects of fundamental and applied researches of experimental and theoretical nanoscale technology dealing with materials synthesis, processing, nanofabrication, nano probes, spectroscopy, properties, biological systems, nanostructures, nano electronics, nano-optics, nano-mechanics, nano-devices, nano biotechnology, nanomedicine, Nano toxicology within the scope of the journal. Experimental and Theoretical NANOTECHNOLOGY aims to acquire the recent and outstanding researches for the benefit of the human being.

TiO₂ nanorods with CdS quantum dots for optical applications

W. Jie^a, J. Lim^{b,*}, H. Ho^c

^aSchool of Physics, State Key Laboratory of Crystal Materials, Shandong University, Jinan 250100, PR China

^bSchool of Information Science and Engineering, Shandong University, Jinan 250100, PR China

^cDepartment of Physics, Portland State University, Post Office Box 751, Portland, OR 97207-0751, United States

*) E-mail address: limj@sdu.edu.cn

Received: 15/12/2019 / *Accepted:* 28/6/2020 / *Published:* 1/9/2020

We combine CdS semiconductor quantum dots and single-crystalline rutile TiO₂ nanorod arrays to produce a practical quantum dot sensitized solar cell. A facile wet-chemical approach was implemented for growth of this CdS@TiO₂ architecture. Rutile TiO₂ nanorod arrays with lengths of 1–2 mm and diameters of 40–60 nm was synthesized on fluorine-doped tin oxide glass by a hydrothermal process in a titanium tetrachloride precursor solution. CdS quantum dots with a size of 5–10 nm was deposited onto a TiO₂ nanorod surface using an ultrasonic-assisted chemical bath deposition method. The resulting CdS quantum dots and TiO₂ nanorods formed a type-II heterojunction and showed increased absorption over visible light range. Incident photon-to-current conversion efficiencies (IPCE) as high as 85% and power conversion efficiencies of 2.54% were obtained using a polysulfide electrolyte.

Keywords: II-VI; QDs; Optical.

1. INTRODUCTION

Novel approaches to utilize solar energy have attracted great attention world-wide. Being a fast-growing source of clean energy solution, Si-based solar cells could provide ample power at a moderate price; the search for an efficient alternative photovoltaic (PV) system still remains a serious challenge. In order to achieve better efficient use of solar energy, many new PV systems have been introduced, including dye-sensitized solar cells (DSSC), organic solar cells, and multi-junction solar cells. Most of these strategies employ the following working principles: (i) absorption

of a high energy photon and subsequent generation of an electron–hole pair. (ii) Charge separation occurs, so the electrons and holes are separated across a heterojunction and (iii) charges are transported to load. To achieve higher photocurrent efficiency, the loss during each step must be minimized. One classical example is the architecture of a DSSC [1,2]. Light is absorbed by dye pigments on the interface between the semiconducting material and conducting liquid electrolyte, the dye molecules become excited and generate hot electrons, which are subsequently transported by the semiconducting material to the electrode. Another example is the conjugated polymer photovoltaic cells in which two or more photovoltaic materials are blended to form a three-dimensional continuous network structure. In this case the light is absorbed by all materials, and photo-generated electron–hole pairs are quickly separated and transported across the nearby interfacial boundaries. Both organic solar cells [3–6] and multi-junction solar cells [7–9] have been constructed to demonstrate this approach. Despite the success of the above-mentioned solar cells, new material application and architecture configuration still need to be discovered to improve performance and reduce the cost of solar cells.

To improve charge transport, single-crystalline wide band gap materials, such as TiO_2 , can be used as a direct pathway from the light absorbing material to the conducting electrode, thereby increasing the photocurrent efficiency [10]. Single crystalline TiO_2 nanorods grown directly on transparent conductive oxide (TCO) electrodes provide a perfect solution by avoiding particle-to-particle hopping that occurs in poly-crystalline films. In addition, the band gap of TiO_2 provides a suitable substrate for visible light transmission and is an ideal material to form a type-II heterojunction with narrow band gap sensitizing materials such as CdS and CdSe. Moreover, the high stability of TiO_2 in corrosive electrolytes makes it a superior choice when weighed against other wide-gap semiconductors such as ZnO [11].

The solar spectrum, containing photons ranging from 0.5 to 3.5 eV, limits the intrinsic practicality of such wide-gap semiconductors because low-energy photons are not absorbed. In conventional tandem solar cell that consists of wide-gap and narrow-gap semiconducting materials, considerable number of high-energy photons dissipate excess energy in the form of heat in the narrow-gap semiconducting material. The use of quantum dots (QD) such as CdS, CdSe, InP, and PbSe to produce more than one electron–hole pair per single absorbed photon, also known as multiple exciton generation (MEG) [12–15], is a promising solution to enhance absorbance efficiency. In addition to the utilization of the MEG phenomenon, CdS QDs offer the ability to adjust absorption spectra by tuning QD sizes to match the solar spectrum [16,17]. Furthermore; the creation of a type-II heterojunction by growing CdS QDs on the TiO_2 surface greatly enhances charge separation.

To date, CdS@ TiO_2 nanostructured solar cells have been reported by several groups. While most of the reported works were conducted on polycrystalline TiO_2 , [18,19] few works were conducted on TiO_2 single crystalline nanorods [20]. In addition, most growth methods relied on vapor phase techniques [21,22] that require high operating temperatures. Compared to vapor phase techniques, wet-chemical approaches are more suitable for inexpensive mass

production and offer better control over morphology. Recently, there has been several reports on attaching QDs onto various

TiO₂ surfaces using different methods: (i) synthesized QDs attached to TiO₂ surfaces with linker molecules [23,24]; (ii) QDs grown directly onto TiO₂ surfaces using successive ionic layer absorption (SILAR) method [16,25]; (iii) QDs grown directly onto TiO₂ surfaces by chemical bath deposition (CBD) approach [26,27]. With the first method, size of QDs can be more readily controlled and QD obtained are of higher quality compared to other methods; however, due to the low coverage on the electrode surface, low power conversion efficiency is achieved. The latter approaches obtained high coverage of the electrode surface with a nucleation and growth mechanism, but rendering it difficult to control the size distribution of QDs and subsequently unable to adjust absorption of spectra to enhance visible light absorption. We used an ultrasound assisted CBD method, which extensively increased CdS QDs growth speed compared to traditional CBD approach also size distribution is more optimized. In our work, there is negligible redshift with increase of CBD cycles suggesting that size growth of CdS QDs is being impeded while achieving a higher surface coverage.

In this article, we introduce an entirely wet-chemical approach toward building a quantum dot sensitized solar cell (QDSSC) with CdS@TiO₂ architecture. QDSSC structures are fabricated using CdS QD sensitizers and TiO₂ nanorods grown directly on fluorine-doped tin oxide (FTO) substrates. A low temperature (180°C) wet-chemical technique was used to grow ordered TiO₂ nanorod arrays directly on FTO glass followed by a facile ultrasound-assisted chemical bath deposition (CBD) of CdS QDs onto rutile single crystalline TiO₂ nanorods. Using this QDSSC, an IPCE as high as 85% can be obtained in the visible light region with a power conversion efficiency of 2.54%.

2. EXPERIMENTAL

TiO₂ nanorod arrays were grown directly on fluorine-doped tin oxide (FTO) coated glass substrates by the following hydro-thermal method: 35–50 mL of deionized water was mixed with 55–40 mL of concentrated hydrochloric acid (HCl, 36–38% by weight, Sinopharm) to reach a total volume of 90 mL in a stainless steel autoclave with a Teflon container cartridge. The mixture was stirred at ambient conditions for 5 min, and then 300–1000 mL of titanium tetrachloride (TiCl₄, 99.9%, Aladdin) was added. After stirring for another 5 min, FTO substrates (2.3 cm, 8–12 Ω/sq), ultrasonically cleaned for 10 min in a mixed solution of deionized water, acetone, and 2-propanol with volume ratios of 1:1:1, were placed at an angle against the Teflon container wall with the conducting side facing down. The hydrothermal synthesis was conducted at 180 °C for 2 h in an electric furnace. After synthesis, the autoclave was cooled to room temperature under flowing water, which took approximately 5 min. The FTO substrate was taken out, washed extensively with deionized water and allowed to air dry.

CdS QDs were deposited onto the TiO₂ nanorod surface by chemical bath deposition (CBD). Before the CBD process, solutions of 0.5 M cadmium nitrate (Cd(NO₃)₂) and 0.5 M sodium sulfide (Na₂S) were prepared by dissolving Cd(NO₃)₂ in ethanol and Na₂S in methanol. A typical CBD cycle involved dipping the FTO, glass pre-grown with TiO₂ nanorods, in Na₂S

solution for 10 min, rinsing in methanol, then dipping it for another 10 min in $\text{Cd}(\text{NO}_3)_2$, and rinsing again in ethanol. The entire CBD process was carried out under ultrasonic agitation (40 kHz, 60 W) with the TiO_2 -coated substrate facing downward and placed at an angle against the beaker wall.

The samples were characterized by X-ray diffraction (XD-3, PG Instruments Ltd.) with Cu K α radiation ($\lambda=0.154$ nm) at a scan rate of 21 min^{-1} . X-ray tube voltage and current were set at 36 kV and 20 mA, respectively. The morphological and lattice structural information was determined by field emission scanning electron microscopy (FESEM, Hitachi S-4800) and transmission electron microscopy (TEM, JEOL JEM-2100).

CdS quantum-dot sensitized solar cells (QDSSC) were assembled using CdS@TiO_2 structure. Pt counter electrodes were prepared by coating a thin layer of Pt on FTO glass using magnetron sputtering. Then, a 60 mm thick sealing material (SX-1170-60, Solaronix SA) with a 3.3 mm aperture was pasted onto the Pt counter electrodes. The CdS@TiO_2 sample and Pt counter electrode were sandwiched and sealed with the conductive sides facing inward. A redox electrolyte was injected into the space between the two electrodes. In this study, a polysulfide electrolyte was used. The liquid electrolyte was composed of 0.5 M Na_2S , 2 M sulfur and 0.2 M KCl (all from Sinopharm) mixed solution of deionized water and ethanol with volume ratios of 35:65.

A solar simulator (Model 11000A, Abet Technologies) with an AM1.5 filter was used to illuminate the working solar cell at light intensity of 1 sun (100 mW/cm^2). A sourcemeter (2400, Keithley) was used for electrical characterization during the measurements. The incident photon-to-current conversion efficiency (IPCE) measurements were carried out with a custom measurement system consisting of a 150 W Xe lamp (LSH-X150, Zolix), monochromator (7ISW30, 7-Star) and a sourcemeter (2400, Keithley). The measurements were carried out without bias illumination with respect to a calibrated OSI standard silicon solar photodiode. UV–visible transmission spectra of the prepared samples were analyzed using a UV–visible spectrometer (TU-1900, PG Instruments, Ltd.).

3. RESULTS AND DISCUSSION

3.1 Growth of single-crystalline rutile TiO_2 nanorods

It is known that wet-chemical techniques are preferred as an ideal process for growing nanostructured materials because the particle size, morphology, and structure can be easily controlled by adjusting preparation parameters. Also, single-crystalline materials are easily obtained through hydrothermal approach. Ordered TiO_2 nanostructures with different morphologies, such as nanoparticles [28], nano-wires [29], and nanotubes [30], have been synthesized by different hard-template methods. Alternative wet-chemical techniques for crystalline TiO_2 growth and morphology control are also an interesting and promising subject.

In our study, we found that the morphology of the TiO_2 nanorods could be adjusted to preferred conditions by varying solution acidity and precursor concentration. The decrease in nanorod diameter and density is evident with an increase in solution acidity and decrease in precursor

concentration (Fig. 1). At a low concentration of titanium tetrachloride (TiCl_4) precursor, slim rod (0.3 mL) and thick rod (0.4 mL) crystals are obtained (Fig. 1a and b). When the concentration of TiCl_4 is increased to 0.5 M, the formation of long thick rods with diameters of 100–300 nm and lengths up to 5 mm (Fig. 1c and d) is observed. When the quantity of precursor was increased to 1.0 mL, a continuous network of TiO_2 , consisting of densely packed TiO_2 nanorods, was observed (Fig. 1e). When the volume ratio of hydrochloric acid and deionized water was decreased from 40:50 (Fig. 1a) to 35:55 (Fig. 1f), the TiO_2 nanorod diameter increased dramatically.

To fully utilize the advantage of the TiO_2 nanorod arrays for better light absorbance, a suitable nanorod spacing and diameter must be determined; the density of TiO_2 nanorods should be maximized while preserving enough space for CdS quantum dot deposition. Smaller nanorod diameters are desirable for increasing the sensitized surface area per unit substrate area, which enhances light absorption. The optimal performance was found with a TiO_2 nanorod growth solution composed of 340 mL TiCl_4 , 40 mL hydrochloric acid, and 50 mL deionized water, reaching a total volume of 90 mL.

TiO_2 nanorods were successfully grown on FTO-coated glass substrates at 180 °C for 2 h. Field emission scanning electron microscopy (FESEM) images of top and cross-sectional views are shown (Fig. 2a and b). The images at different locations and viewing angle reveal that the entire surface of the FTO-coated glass substrate is uniformly covered with ordered TiO_2 nanorods. Fig. 2d shows a high magnification FESEM image of the nanorods, which are typically 40–60 nm in diameter and 1–2 mm in length. The density of nanorods is typically 20 nanorods/ mm^2 with an average spacing of 200 nm. The nanorods are tetragonal in shape with square top facets consisting of many small grids. X-ray diffraction (XRD) patterns show that the TiO_2 grown on the FTO-coated glass substrates have a tetragonal rutile structure [SI 1]. Compared to powdered rutile TiO_2 XRD patterns, the (002) diffraction peak was significantly enhanced, and some diffraction peaks including (101), (110), and (211) were absent, which indicates that the TiO_2 nanorods are highly oriented with respect to the substrate surface normal and that the TiO_2 nanorods grow in the (001) direction with the growth axis perpendicular to the substrate surface. A TEM image and a corresponding selected area electron diffraction (SAED) pattern indicate high crystallinity of the TiO_2 nanorods (Fig. 2c). The reason that the hydrothermal growth method delivers rutile phase instead of other phases, such as anatase and brookite, could be attributed to the small lattice mismatch between FTO and rutile. Both rutile and SnO_2 have near identical lattice parameters with $a = 4.594$, $c = 2.958$ and $a = 4.737$, $c = 3.185$ for TiO_2 and SnO_2 , respectively, making the epitaxial growth of rutile TiO_2 on FTO film possible. On the other hand, anatase and brookite have lattice parameters of $a = 3.784$, $c = 9.514$ and $a = 5.455$, $c = 5.142$, respectively. The production of these phases is unfavorable due to a very high activation energy barrier which cannot be overcome at the low temperatures used in this hydrothermal reaction.

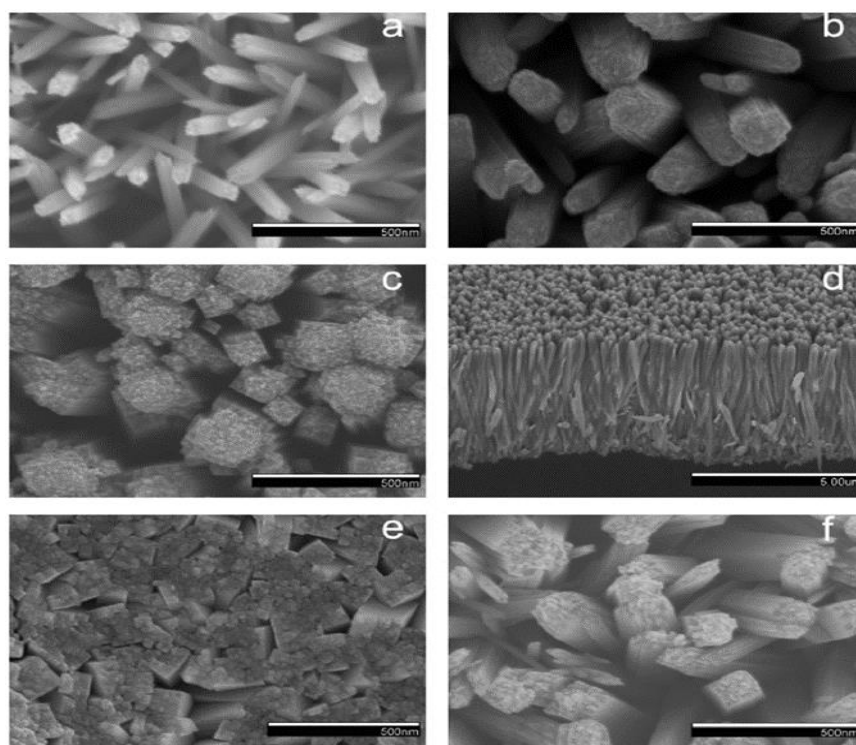


Figure 1 FESEM images of TiO_2 nanorods grown at 180 °C for 2 h with different amounts of titanium tetrachloride in static solutions of 40 mL hydrochloric acid and 50 mL deionized water: (a) 0.3 mL, (b) 0.4 mL, (c) 0.5 mL top view, (d) 0.5 mL cross-sectional view, (e) 1.0 mL of titanium tetrachloride, (f) 0.3 mL of titanium tetrachloride in a solution of 35 mL hydrochloric acid and 55 mL deionized water.

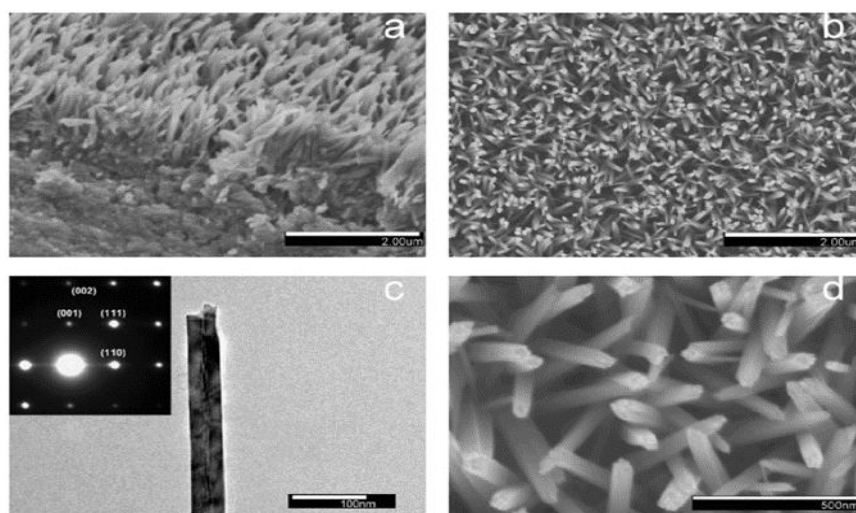


Figure 2 FESEM images of TiO_2 nanorods; (a) cross-sectional view, (b) top view, (d) high magnification view. (c) TEM image of a single-crystalline TiO_2 nanorod and corresponding SAED pattern.

3.2 Deposition of CdS quantum dots

Compared to conventional bulk semiconductors, the relaxation rate of photo-generated excitonic states in quantum dots is much slower due to a ‘phonon bottleneck’ effect, which has been observed in quantum dots by a research group at NREL [31], allowing MEG to become dominant in QDs. Also, to increase utilization of photon energy in the visible light region, the band gap of the semiconducting material used for QD sensitization must fall within the range of 0.5 eV–3.5 eV. CdS was chosen as an ideal system for sensitization because the MEG phenomenon in CdS QDs has been well-studied [32–34]. CdS quantum dots were deposited onto the surface of TiO₂ nanorods by chemical bath deposition (CBD) under ultrasonic environment in alcohol solvents. It is noteworthy that the deposition rate of the CdS assembled in the alcohol system is much higher than in aqueous solutions [35]. Figs. 3a–b and c–d show typical FESEM and TEM images of the CdS QDs deposited onto TiO₂ nanorods. The CdS QDs are typically 5–10 nm in diameter with uniform coverage of the TiO₂ nanorod surface. Selected area electron diffraction (SAED) of the CdS coated TiO₂ nanorod (Fig. 3c) shows clear spot diffraction patterns due to the high crystallinity of the tetragonal rutile TiO₂ nanorod, as well as rings characteristic of the greenockite CdS QDs. To obtain a thick layer of CdS QDs for better XRD characterization, CdS QDs were deposited onto bare glass substrates for more than 10 CBD cycles. XRD patterns of an as-deposited CdS QD layer also indicate a crystalline hexagonal greenockite structure [SI 2].

The advantage of our synthetic method is that the CdS quantum dots make direct contact with the TiO₂ nanorod surface. The CdS QDs form a firm connection on the TiO₂ nanorods with a type-II heterojunction that greatly enhances charge transport, charge separation, and overall photocurrent efficiency of our solar device. Also, CBD under ultrasonic agitation greatly enhanced the speed of CdS quantum dot deposition. SEM images are presented for CdS deposition with and without ultrasonic assistance after 5 CBD cycles [SI 3]. The improved performance of CdS QDSSC Enhanced absorption of visible light by the CdS@TiO₂ structure was confirmed by UV–visible spectroscopy (Fig. 4a). The CdS@TiO₂ structure showed a higher absorption coefficient compared to bare TiO₂ nanorods over the entire visible light spectrum. The evident increase in light absorption after CBD of CdS QDs is evident around 400 nm and 540 nm. The CdS@TiO₂ showed an apparent increase in absorption of the visible light ranging from 400 to 550 nm. This increase in absorption is mainly due to the layer of CdS QDs deposited onto the TiO₂ nanorod, as this absorption edge is close to the band gap of CdS ($E = 2.45$ eV).

Fig. 4b shows UV–visible transmission spectroscopy obtained from the CdS@TiO₂ samples prepared through various CBD cycles. Increased visible light absorption was observed with increase in CBD cycle, indicating an increased amount of CdS deposition. Compared to other works, the redshift of the absorption edge and onset position with increased CBD cycle is negligible with increased CBD cycle implying the size growth of CdS QDs is impeded with ultrasound agitation. In the first few CBD process, TiO₂ nanorod surface is not completely covered by CdS QDs; after 5 CBD cycles CdS QD layer thickness growth become dominant and surface is fully covered with a layer of CdS. Low coverage of the TiO₂ surface give rise to a low light absorption resulting in low

efficiency; on the other hand, excess of CdS QDs hinders both charge transport and diffusion of the electrolyte also increases the recombination of photoexcited carriers in the interfacial area between the QD consequently resulting in low overall efficiency [36].

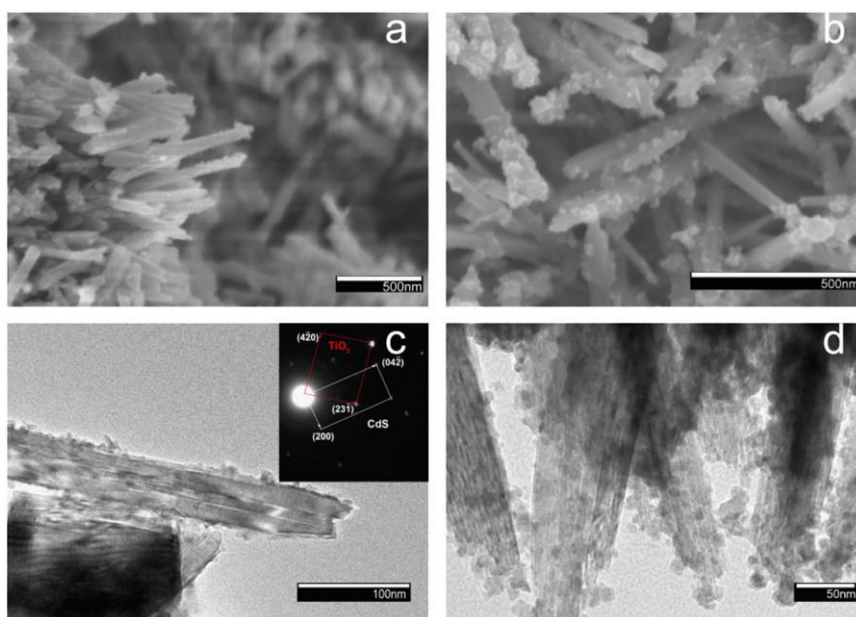


Figure 3 FESEM images of (a) cross-sectional and (b) top view of CdS QD coated TiO₂ nanorods. (c) TEM image of a CdS QD coated TiO₂ nanorod and corresponding SAED pattern. (d) TEM image of CdS QDs deposited onto TiO₂ nanorods.

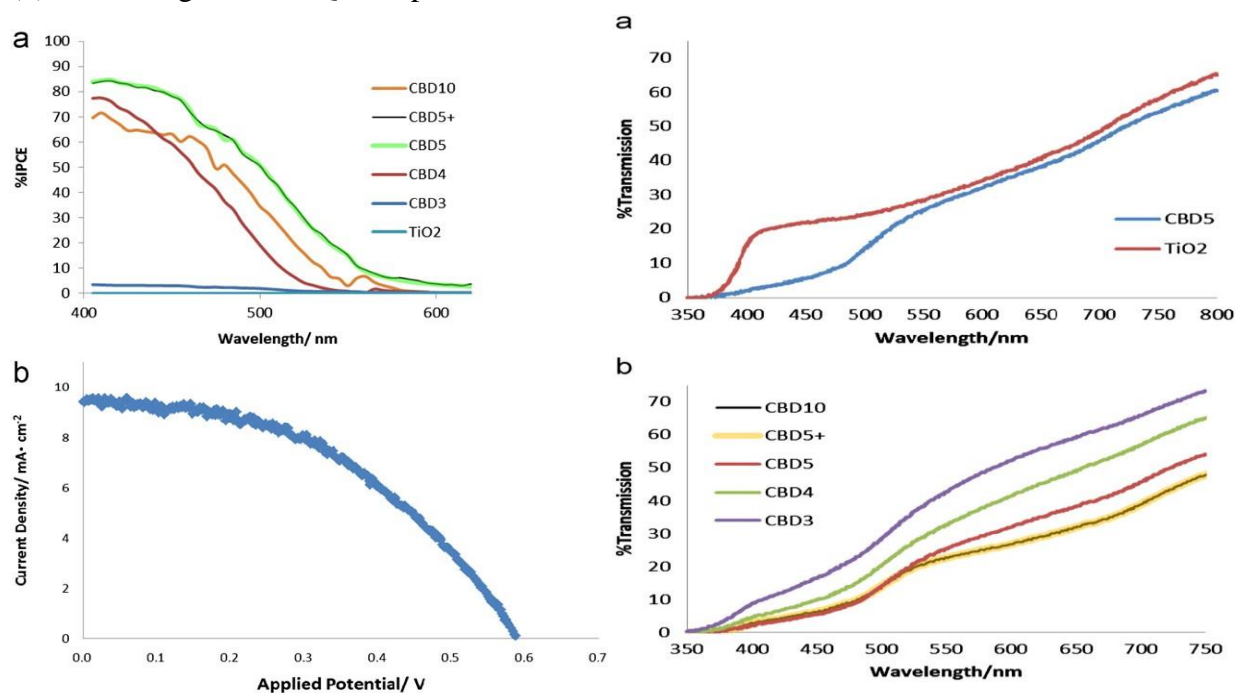


Figure 4 (a) UV–visible transmission spectra of bare TiO₂ nanorod arrays (red) and CdS QD coated TiO₂ nanorod arrays (blue). (b) UV–visible transmission spectra of CdS QD coated TiO₂ nanorod arrays obtained after various CBD cycles.

The incident photon to current conversion efficiencies (IPCE) obtained from QDSSCs assembled using various electrodes prepared through different CBD cycles are shown in Fig.

5a. By using the S/S^{2-} redox couple electrolyte, IPCE values as high as 85% can be obtained for wavelength in the visible light region with 5 CBD cycles. An increase in CBD cycles is followed by an increase in IPCE over the entire visible light region, implying that the CdS QDs play a major role in photon- to-electron conversion. After 5 CBD cycles, the IPCE drops slightly and when reaching 10 CBD cycle, IPCE drops even lower especially in the 400–500 nm visible light region where CdS QDs play a major role in modifying absorption spectra. The photocurrent–voltage (I – V) curves of the QDSSC were measured under one sun illumination (AM1.5, 100 mW/cm²). An maximum efficiency of 2.54% was obtained with a CdS@TiO₂ sample prepared with 5 CBD cycles (Fig. 5b). Compared with the reported results, the efficiency of CdS QDSSCs obtained using single crystalline TiO₂ nanorods is higher than using conventional mesoporous TiO₂ films (1.84%) [37]; the efficiency of CdS QDSSC acquired through wet-chemical approaches showed higher performance than CVD equivalents (1.51%) [38]. This may be attributed to better size control of CdS QDs and optimized adhesion between the CdS QDs and TiO₂ nanorods. CdS QDSSCs constructed through this wet-chemical approach showed superior performance compared to recent reports [36–38].

Although the efficiency obtained with this CdS QDSSC is still low compared with Graetzel Cells using dye sensitizers, Fig. 5 (a) IPCE spectra of CdS QD coated TiO₂ nanorod arrays obtained after various CBD cycles. (b) Current–voltage (I – V) characteristics of CdS QD coated TiO₂ nanorod arrays obtained after 5 CBD cycles. the CdS QDSSCs presented in our work provide advantages that are not available in DSSCs. First, the use of quantum dots offers the ability to adjust absorption spectra by tuning CdS QD sizes. Second, the photochemical stability of CdS quantum dots is more desirable compared to organic dyes. Third, exploiting the multiple exciton generation (MEG) effect with CdS QDs offers the opportunity to surpass the Shockley– Queisser limit [39]. This study opens a possibility to use a 3D nanostructured material with a facile wet-chemical approach for QDSSC studies. In the present study, the low efficiency of the CdS QDSSC is limited by narrow-range absorption of CdS QDs in the visible light region and the low transport efficiency of the S/S^{2-} redox couple. By applying sensitizing materials with narrower band gaps and a more efficient redox couple electrolyte, higher cell efficiency could be achieved.

4. CONCLUSIONS

Single-crystalline TiO₂ nanorod arrays with practical length (1–2 mm) and density (20 nanorods/mm²) were successfully grown on fluorine-doped tin oxide (FTO) glass substrates by a facile hydrothermal approach. CdS quantum dots with a size of 5–10 nm was deposited onto a TiO₂ nanorod surface using ultrasound assisted chemical bath deposition (CBD). The CdS@TiO₂ heterojunction showed a notable increase in visible light absorption, enhanced incident photon-to-current conversion efficiency (IPCE) as high as 85% can be obtained for wavelength in the visible light region. Quantum-dot sensitized solar cells (QDSSC) constructed with CdS@TiO₂ structures operated at 2.54% power conversion efficiency. The performance of CdS QDSSCs is approaching the efficiencies of dye-sensitized solar cells (DSSC), providing an alternative solution in solar cell design and fabrication.

References

- [1] Ali H. AL-Hamdani, Mohammed A.R. Hussein, Aya H. Makki, *Experimental and Theoretical NANOTECHNOLOGY* 3 (2019) 1
- [2] M. Gratzel, *Nature* 414 (2001) 338
- [3] M.J. Currie, J.K. Mapel, T.D. Heidel, S. Goffri, M.A. Baldo, *Science* 321 (2008) 226
- [4] B. Eva, C.K. Frederik, *Solar Energy Materials and Solar Cells* 91 (2007) 954
- [5] G. Serap, N. Helmut, S.S. Niyazi, *Chemical Reviews* 107 (2007) 1324
- [6] Y.J. Cheng, S.H. Yang, C.S. Hsu, *Chemical Reviews* 109 (2009) 5868
- [7] R.R. King, *Nature Photonics* 2 (2008) 284
- [8] W. Guter, J. Schone, S.P. Philipps, M. Steiner, G. Siefer, A. Wekkeli, E. Welser, E. Oliva, A.W. Bett, F. Dimroth, *Applied Physics Letters* 94 (2009) 223504
- [9] J. Geisz, S. Kurtz, M.W. Wanlass, J.S. Ward, A. Duda, D.J. Friedman, J.M. Olson, W.E. McMahon, T.E. Moriarty, J.T. Kiehl, *Applied Physics Letters* 91 (2007) 023502
- [10] B. Liu, E.S. Aydil, *Journal of the American Chemical Society* 131 (2009) 3985
- [11] K.S. Leschkie, R. Divakar, J. Basu, E. Enache-Pommer, J.E. Boercker, C.B. Carter, U.R. Kortshagen, D.J. Norris, E.S. Aydil, *Nano Letters* 7 (2007) 1793
- [12] L.M. Peter, D.J. Riley, E.J. Tull, K.G.U. Wijayantha, *Chemical Communications* 10 (2002) 1030
- [13] A.J. Nozik, *Chemical Physics Letters* 457 (2008) 3
- [14] A. Luque, A. Marti, A.J. Nozik, *MRS Bulletin* 32 (2007) 236
- [15] P.V. Kamat, *Journal of Physical Chemistry C* 112 (2008) 18737
- [16] D.R. Baker, P.V. Kamat, *Advanced Functional Materials* 19 (2009) 805
- [17] S.K. Haram, B.M. Quinn, A.J. Bard, *Journal of the American Chemical Society* 123 (2001) 8860
- [18] G.K. Mor, K. Shankar, M. Paulose, O.K. Varghese, C.A. Grimes, *Nano Letters* 6 (2006) 21
- [19] K. Zhu, N.R. Neale, A. Miedaner, A.J. Frank, *Nano Letters* 7 (2007) 69
- [20] H. Wang, Y.S. Bai, H.Z.H. Zhang, Zhang, J.H. Li, L. Guo, *Journal of Physical Chemistry C* 114 (2010) 16451
- [21] J.J. Wu, C.C. Yu, *Journal of Physical Chemistry B* 108 (2004) 3377
- [22] C. Weng, K.F. Hsu, K.H. Wei, *Chemistry of Materials* 16 (2004) 4080
- [23] A. Kongkanand, K. Tvrdy, K. Takechi, M. Kuno, P.V. Kamat, *Journal of the American Chemical Society* 130 (2008) 4007
- [24] I. Robel, V. Subramanian, M. Kuno, P.V. Kamat, *Journal of the American Chemical Society* 128 (2006) 2385
- [25] V. Gonza'lez-Pedro, X. Xu, I. Mora-Sero', J. Bisquert, *ACS Nano* 4 (2010) 5783
- [26] T. Toyoda, K. Oshikane, D. Li, Y. Luo, Q. Meng, Q. Shen, *Journal of Applied Physics* 108 (2010) 114340
- [27] T. Sugimoto, X. Zhou, A. Muramatsu, *Journal of Colloid and Interface Science* 259 (2003) 43
- [28] C. Lee, Y.M. Sung, T.G. Kim, H. Choi, *Applied Physics Letters* 91 (2007) 113104
- [29] J.L. Blackburn, D.C. Selmarten, A.J. Nozik, *Journal of Physical Chemistry B* 107 (2003) 14154
- [30] Y. Wada, H. Kuramoto, J. Anand, T. Kitamura, T. Sakata, H. Mori, S. Yanagida, *Journal of Materials Chemistry* 11 (2001) 1936
- [31] P.H. Mugdur, Y.J. Chang, S.Y. Han, Y.W. Su, A.A. Morrone, S.O. Ryu, T.J. Lee, C.H. Chang, *Journal of the Electrochemical Society* 154 (2007) 482
- [32] Y.J. Shen, Y.L. Lee, *Nanotechnology* 19 (2008) 045602

- [33] H. Chang, Y.L. Lee, *Applied Physics Letters* 91 (2007) 053503
- [34] S. Hachiya, Y. Onishi, Q. Shen, T. Toyoda, *Journal of Applied Physics* 110 (2011) 054319
- [35] Y.L. Lee, C.H. Chang, *Journal of Power Sources* 185 (2008) 584
- [36] C. Lee, T.G. Kim, W. Lee, S.H. Han, Y.M. Sung, *Crystal Growth and Design* 9 (2009) 4519
- [37] W. Shockley, H.J. Queisser, *Journal of Applied Physics* 32 (1961) 510

Solar energy harvesting efficiency of nano-antennas

B. D. Buschow, H. Rio*

Katholieke Universiteit Leuven, ESAT/TELEMIC, Kasteelpark Arenberg 10, B-3001
Leuven, Belgium

*) E-mail address: hrio@esat.kuleuven.be

Received: 8/1/2020 / *Accepted:* 15/5/2020 / *Published:* 1/9/2020

The radiation efficiency of nano-antennas is a key parameter in the emerging field of IR and optical energy harvesting. This parameter is the first factor in the total efficiency product by which nano-antennas are able to convert incident light into useful energy. This efficiency is investigated in terms of the metal used as conductor and the dimensions of the nano-antenna. The results set upper bounds for any possible process transforming light into electrical energy. These upper bounds are the equivalent of the theoretical upper bounds for the efficiency of conventional solar cells. Silver shows the highest efficiencies, both in free space and on top of a glass (SiO₂) substrate, with radiation efficiencies near or slightly above 90%, and a total solar power harvesting efficiency of about 60–70%. This is considerably higher than conventional solar cells. It is found that fine-tuning of the dipole dimensions is crucial to optimize the efficiency. © 2012 Elsevier Ltd. All rights reserved.

Keywords: Harvesting; Energy; Solar; Nano-antenna.

1. INTRODUCTION

Solar energy is expected to deliver a considerable contribution to the solution of human kind's energy problem. At this moment, 90% of the solar cells in the market are based on crystalline silicon wafers. The disadvantage of this technology is the lower efficiency by which the transformation of energy from optical frequencies to low frequencies is performed. Typical efficiencies are in the order of 20–30%. With these efficiencies, if human kind's energy need would be fully satisfied by present day solar cells, the required area would be about 400,000 km². Assuming that only 10% of the energy need would be provided by solar energy harvesting, it is easily seen that doubling the efficiency of solar panels corresponds to

an area of 20,000 km². This is more than half the area of a country like Belgium. The efficiency of solar energy harvesting is a matter of high interest. In recent years, the idea of using nano-rectennas (nano-antenna or nantenna+rectifier) to harvest solar energy has been suggested. It is claimed that the efficiency of this type of topology may be much larger. The figures mentioned go from a staggering 90% [1], to a more “down-to-earth” 30–40% [2]. It is suggested that the circuits themselves can be made of a number of different conducting metals, and the nano-antennas can be printed on thin, flexible materials like polyethylene, a very cheap and common plastic.

In this paper, to the knowledge of the authors for the first time, realistic numbers are presented for the maximum efficiencies that can be reached with nano-antenna technology. These numbers are based on a detailed study of a single antenna topology, the basic dipole, for a range of different metals and different sizes. The total efficiency of nano-rectennas consists of two parts. The first part is the efficiency by which the light is “captured” by the nano-antenna and brought to its terminals. Due to reciprocity, this efficiency is the same as the efficiency by which the antenna is able to convert input power given at its terminals into radiation. This efficiency is thus the radiation efficiency Z^{rad} of the antenna. Although this efficiency has been very well studied for traditional antennas, the in-depth characterization of this parameter has not yet been addressed in the nano-antenna research community. To start with, in by far most papers on nanoantennas known to the authors, only gold is considered as metal. Concerning topologies, some information can be found [3,4]. However, Gao [3] considers only two structures of the same length and a very rough Drude model is used in the FDTD solver used, fitting the experimental material parameter data. It can be proven that this affects the efficiencies considerably. Huang [4] uses only a single frequency. The second part is the efficiency by which the captured light is transformed into low frequency electrical power by the rectifier. At lower frequencies, rectifying circuits are common, but at IR and optical frequencies and in combina. Although nano-photonics, and especially plasmonics, is a rapidly growing research field [6], the more in depth study of nano-antennas as such has emerged quite recently [9–16]. Following a quite different path, but also quite promising in the area of photovoltaics is the study of the use of so-called nano-wires and nano-tubes, as investigated for example, by the group of Lieber [17–19]. A recent review article concerning nanostructures for efficient light absorption and photovoltaics is [20].

2. FROM INCIDENT WAVE TO RECEIVED POWER

Both the transmitting and receiving process can easily be described by a very simple equivalent circuit. In receive mode, see Fig. 1, V_{open} is the voltage generated by the receiving antenna at its open terminals. V_{rec} is the voltage seen at the terminals when a current is flowing to the rectifier. This current generates power in the resistors R_{ant} and R_{loss} . The power in the loss resistor P^{loss} is the power actually dissipated in the metal of the antenna. The useful power is the power going to the impedance of the rectifier Z_{rec} . This power is with nano-antennas, efficient rectification is a real. Note that there is also power that is challenge. A very interesting new technique to realize this transformation has very recently been introduced. M.W. Knight [5] and colleagues have made an optical nano- antenna that also works as a photodetector capable of converting light into either current or voltage. This was done by growing rod-like arrays of gold nano-antennas directly onto a silicon surface—so creating a metal–semiconductor (or Schottky) barrier formed at the antenna–semiconductor

inter- face. The efficiency of the two steps combined was 0.01%. This very low figure is in sharp contrast with the efficiencies mentioned by Kotter [1] and Service [2], and it illustrates the long way still to go before real practical use can be made of solar energy harvesting with nano-antennas.

This paper considers the first step only, the capturing of the IR and optical waves and the transport of the energy embedded in these waves to the terminals of the nano- antenna. It may be clear that the intrinsic radiation efficiency of nano-antennas is a crucial factor in the energy harvesting debate. A three-fold increase in net energy yield would give enormous advantages if applied at a large scale. It is essential to point out that the interaction between light and nano-antennas in the frequency bands considered can still be analyzed with a high degree of accuracy using classical electromagnetic theory [3,7,8]. The fact that at this small scale, no quantum effects have to be taken into account is really a crucial observation. It means that the concept of an “antenna”, a device able to transmit and receive electromagnetic waves rather than particles, still works. Basically, the coupling between an electromagnetic (light-) wave and a nano-antenna (a so-called nantenna) is thus the same as it is at microwave frequencies, and can be studied in the same way.

Actually scattered, or in other words “received and re- radiated” by the antenna. The maximal power going to the rectifier for a given incident field is under matching conditions. It is easily checked that under matching conditions the ratio of the power given to the rectifier in case of losses ($R_{loss} \neq 0$) and the power given to it in case of no losses ($R_{loss} = 0$) is exactly the radiation efficiency. Since the purpose of this paper is to derive upper bounds for the efficiencies, these optimal matching conditions will be assumed at all frequencies considered. However, note that matching the antenna and the rectifier is a challenge in its own, see [4]. Most solar radiation is in the visible and the near-infrared wavelength region (Fig. 2). In order to form an alternative to state-of-the-art solar cells, nano-antennas have to be designed for this part of the spectrum. Since the material properties in these bands may vary a lot with frequency, studies in the lower frequency bands, as already discussed in literature [1], may be useful to build up necessary know-how, but do not necessarily offer the solutions for the concrete problems at hand in the IR and optical frequency range.

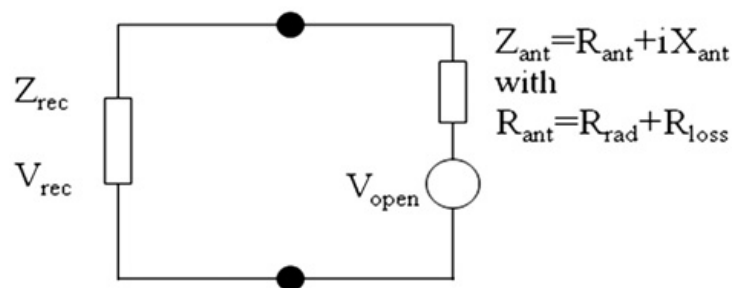


Figure 1 Equivalent circuit for a receiving nano-antenna.

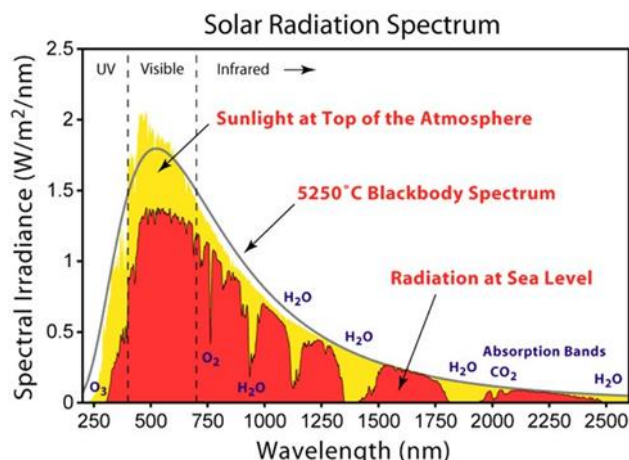


Figure 2 The solar spectrum. The major part of the energy is located in the visible and the near-infrared band. The contribution to the total energy of the part above 1500 nm is very small.

Having the specific application of solar energy harvesting in mind, a new parameter is proposed to characterize the antenna:

the total harvesting efficiency. Modeling techniques, i.e. the Finite Difference Time Domain technique (FDTD). Benchmarking of the simulation tool against measurements was done as part of previous studies [8,25], and will not be repeated here. For a gold monomer topology with three different lengths, extinction cross sections of arrays of $50 \times 50 \text{ nm}^2$ with 2 nm pitch were measured using a Fourier transform infrared spectrometer equipped with a microscope. The agreement found between simulations and measurements in [25] is excellent. The main conclusion of the benchmarking is that both solvers yield very similar results, and correspond quite well with the measurements. There is only a slight frequency shift.

The dipole topology studied in this paper is depicted in Fig. 3. This topology is sensitive mainly to an electric field polarized in its longitudinal direction. Its reaction to this field is strongly depending on its size and the metal used. Any excitation of this dipole will excite two plasmons propagating in opposite directions and interfering with each other. This is clearly illustrated in Fig. 4, where the longitudinal current on an Aluminum dipole evaluated just below the top surface is depicted for different lengths of the dipole in free space. The dipole is considered in transmit mode and is excited in the middle. The wave effect is obvious. It is clearly seen that the excitation in the middle generates a plasmonic wave, which reflects at the end, causing interference. This explains the constant distance of the null (in dark blue) from the ends of the dipole. From the current pattern the wavelength of the plasmon inside the dipole is found to be around 160 nm. It is also seen where l is the wavelength, $Z^{rad}(l)$ is the radiation efficiency of the nano-antenna as a function of the wavelength, and P is Planck's law for black body radiation at the length of the dipole determines the amplitude of the current. In Fig. 4 the largest currents are found for the dipoles of length 100 nm and 320 nm, where a clear resonance occurs. In Fig. 5 efficiencies obtained with MoM and FDTD are where T is the absolute temperature of the black body (in K), h is Planck's constant (6.626×10^{-34} Js), c is the speed of light in vacuum (3×10^8

m/s), and k is the Boltzmann constant ($1.38 \cdot 10^{-23}$ J/K). In the case of solar energy harvesting, the temperature T is the temperature of the surface of the sun. The values calculated with (2) have to be considered upper bounds since practical solar radiation is filtered by the atmosphere. However, they provide an excellent figure of merit for the nano-antenna topologies investigated.

Although material properties at these frequencies are well-known, to date, as far as the authors know, no systematic analysis or measurement campaigns have been done in the area of nano-dipoles concerning the use of different materials. Also, very scarce information is available on radiation efficiencies of these structures. This work reports on a systematic numerical study of the radiation efficiency of IR and optical nano-dipoles for five different metals. No Drude model is used but the experimental values of the material parameters are used directly. The solver used in this work is based on the solution of volumetric integral equations with the Method of Moments (MoM) [21,22]. Following the advice given by Vasylychenko [23], it was first benchmarked against another solver and against measurements. The second solver is well-known in the optical research community [24]. It uses a totally different compared for a 250 nm long gold dipole. It is seen that there is an excellent agreement. The main target of this paper is to derive upper bounds for the efficiencies that can be reached for any possible process by which the IR and optical energy can be transformed.

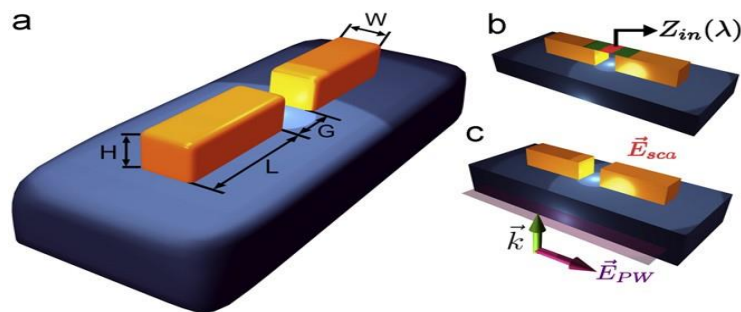


Figure 3 The dipole model studied. (a) w and H are set equal to 40 nm and the gap G is fixed at 10 nm, which is the same value as used in [3]. (b) The dipole as transmitting antenna with a model for the feeding structure located in the gap. (c) The dipole as receiving antenna excited by a plane wave, which is the case of interest.

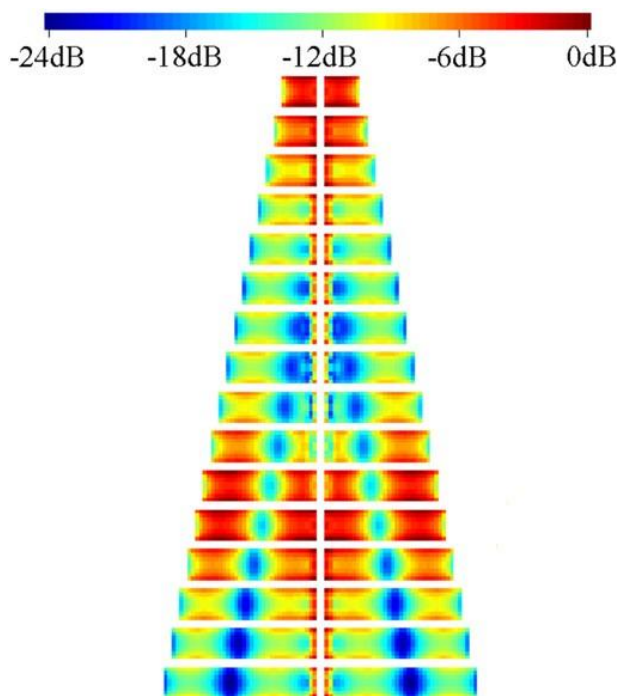


Figure 4 Current distribution on an Al dipole for lengths varying between 100 and 400 nm in steps of 20 nm. Width and height are 40 nm.

The frequency is 1000 THz and the excitation are a constant current applied in the gap. The interference patterns and resonances of the plasmonic waves can be clearly seen.

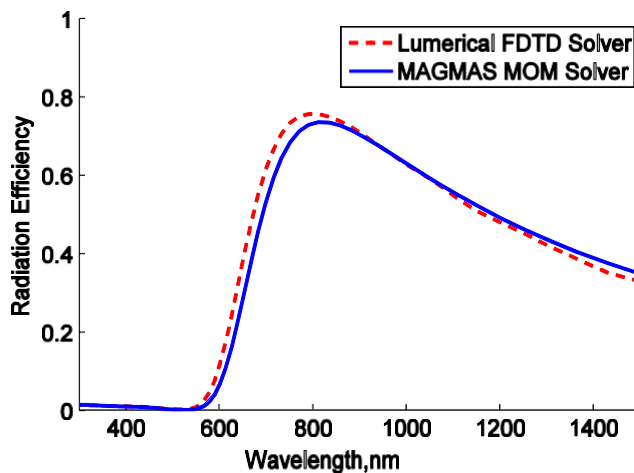


Figure 5 Comparison between FDTD and MoM for a gold dipole, $L=250$ nm.

These upper bounds are the equivalent of the theoretical efficiency upper bounds for conventional solar cells. This is done for five metals, including the most popular ones used in plasmonics. It is evident that our techniques can also be used for other metals.

3. EFFICIENCIES IN VACUUM

The results of a first comprehensive study of the antenna are given in Fig. 6. There, efficiencies are given for silver, gold, aluminum, copper, and chromium, respectively, not taking into account the effect of any substrate layer. The permittivity of the materials used in the simulations is obtained through experimental ellipsometry. They are presented in Fig. 7. Both the radiation efficiencies as a function of wavelength, and the total harvesting efficiency are given. The results are revealing. It is clearly seen that chromium is not suited at all for energy harvesting. The maximum efficiency is in the order of 20%. Copper reaches efficiencies in the order of 60–70%, but the bandwidth is rather limited. This is reflected in the total efficiency which reaches a maximal value of about 30% for a dipole length of ca. 300 nm. The same is observed for gold, the material most used in this area. Its efficiencies are a bit higher than for copper, in the order of 70–80%, but the total efficiency reaches a maximum of about 35% for a dipole length also of 300 nm. Aluminum performs quite well and reaches efficiencies of 60–70% around 500–600 THz, which is in the middle of the visible range. Also, it shows reasonable efficiency values over the whole frequency band considered (200–1000 THz), in the order of 20–50%, yielding total efficiency values of about 50% for a whole range of dipole lengths. The highest values are obtained for silver. In the lower region of the band considered, silver is by far superior over all other metals. It reaches efficiencies over 80–90% in a remarkably wide band. Only at higher frequencies, aluminum outclasses silver. The maximal total harvesting efficiency reached by silver is 65.4% at a dipole length of 200 nm. Note also that clearly the frequency dependency of the efficiencies is totally different for the different metals, due to the specific frequency dependency of their complex permittivity. Also, since the efficiency is strongly depending on the imaginary part of the permittivity (corresponding to conductivity), the use of a proper value in the calculations is mandatory. Simple Drude models that may result in serious errors, up to about 100% [3], are incapable of providing a good prediction of the efficiency.

4. EFFICIENCIES ON A SUBSTRATE LAYER

Since nano-dipoles have to be fabricated on a supporting layer, in a second study, the effect of a glass substrate is investigated. Also, for the glass substrate the measured permittivity's are used in the analysis. For the frequency range considered this permittivity is almost constant and about 2.1. The efficiencies as a function of frequency (or free space wavelength) for different thicknesses of the substrate are plotted in Fig. 8. It is clearly seen that the substrate does have a major effect. The efficiencies obtained are in most cases lower than in case a substrate is not present. Only for very large thicknesses (in principle going to infinity), both the efficiencies as a function of wavelength and the total efficiencies recover to reach about the same values as in the case without substrate. This observation does not pose a problem since the substrate layers used in practice are indeed very thick compared to the wavelength. The total efficiencies on a half space of substrate material are 61.6% for silver, 34.3% for gold, 50.3% for aluminum, 29.5% for copper, and 9.4% for chrome. This lowering effect is caused by the interference of the field waves reflected at the interfaces of the substrate. This is clearly illustrated in Fig. 9, where for three materials and for two selected frequencies, the efficiency is given as a function of the substrate thickness.

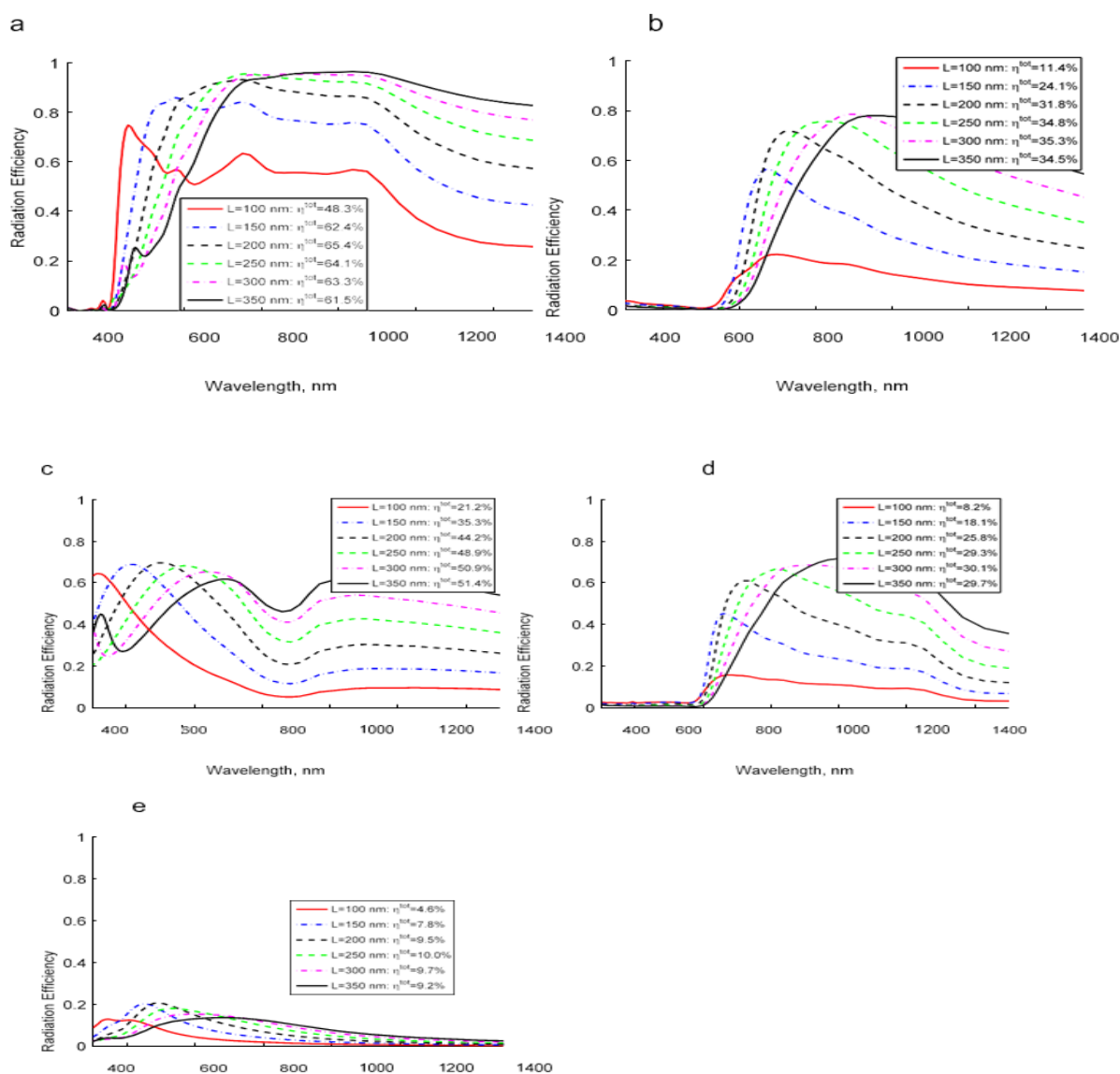


Figure 6 Radiation efficiency of nano-dipole as a function of free space wavelength and dipole length: (a) silver, (b) gold, (c) aluminum, (d) copper, and (e) chromium.

The relation between the radiation efficiency and the thickness clearly shows an oscillating behavior. Studying Fig. 9 in more detail it can be seen that the oscillation is governed only by the frequency and is independent of the material of the dipole. Also, the period of the oscillation is about 400 nm in the first graph and about 350 nm in the second graph. This clearly proves that the effect is caused by the either constructive or destructive interference of the waves reflected at the two boundaries of the glass substrate. Also, the specially shaped peaks can be explained. This behavior stems from the fact that the glass substrate is actually a dielectric slab waveguide. The introduction of a new propagating mode in this waveguide with increasing thickness of the substrate goes along with an extra power loss. This effect generates the discontinuity in the derivative of the efficiency function. For a certain thickness the surface wave is maximally. It is possible to approximately assess any arbitrary material

with respect to its harvesting capabilities. For this, we need to separate the effect of the plasmonic waves traveling along the dipole, and consequently the complex interferences, from the effect of the material. This is easily done for an elementary dipole antenna in free space, i.e. a dipole with very short length with respect to the wave-length. For such an antenna the radiated power is proportional to the square of the dipole moment excited and the efficiency is minimal. The major conclusion of this second study is that (1) the presence of a substrate overall decreases the efficiencies, and (2) considering the same thickness of the glass, again silver is by far superior over the other materials. Note that this expression confirms the fact that the imaginary part of the permittivity always has to be negative, as observed in Fig. 7. Keeping the electrical volume of the dipole constant and small, it is easily seen that the efficiency becomes dependent only on the permittivity. From a material perspective, the key issue is to get the ratio.

5. EXTRACTION OF THE EFFECT OF THE MATERIAL PROPERTIES

It is worthwhile to explain these results from a physical point of view. Through (2), the total harvesting efficiency is completely determined by the radiation efficiency, which is a function of frequency/wavelength. The key issue is to try to reach the highest efficiencies around 500 nm, where the solar irradiance is the largest. This can be done by choosing the proper dipole length. The reason is that this length is one of the main factors that determines the response of the dipole. However, the properties of the material also have a strong effect on the response. That explains why a different optimal length is found for different materials. Also, efficiency is totally depending on losses, and losses are determined by the imaginary part of the permittivity. imaginary part with respect to the real part of the permittivity, or, when the real part approaches 1, for a very large imaginary part. Expression (7) is illustrated in Fig. 10 for the five metals considered while the electrical volume is kept constant at $k^3V = 1$. This means that a different dipole size at each frequency is used in order to remove the effect of the topology itself. The strong dependency of the efficiency on the permittivity is clearly visible. The steep rise around 400 nm and 600 nm, for Ag on the one hand and Au and Cu on the other hand, is also clearly seen in the efficiency curves given in Figs. 6 and 8, but modulated there by the plasmonic waves and resonance. Fig. 10 reveals why silver outclasses the other materials, and why aluminum is a good alternative. They keep a high efficiency in the whole frequency band of importance.

6. CONCLUSION

In this study upper bounds are derived for the efficiencies by which energy can be harvested from the sun using nanoantenna technology. To this goal, the parameter “total harvesting efficiency” is introduced. Both dipoles in free space and on a glass, substrate are considered. For silver nano-dipoles, a maximum of about 60–70% is found. It is an open question whether it is possible to construct alloys with even lower losses at plasmonic frequencies, and thus higher efficiencies. A simple approximating formula is derived to assess the intrinsic harvesting capabilities of a material. Several challenges remain. Silver is more susceptible to oxidation, which can completely destroy its superiority, and which is one of the reasons why gold is so popular in this field. This can be solved by embedding it within the glass substrate,

which requires to develop alternative fabrication

References

- [1] D.K. Kotter, S.D. Novak, W.D. Slafer, P. Pinhero, Solar nantenna electromagnetic collectors, in: 2nd International Conference on Energy Sustainability, August 2008, Jacksonville, Florida, USA, pp. 10
- [2] M. Namdar, Sh. Kh. Asl, *Experimental and Theoretical NANOTECHNOLOGY* 3 (2019) 9
- [3] H. Gao, K. Li, F. Kong, H. Xie, J. Zhao, *Progress in Electromagnetics Research* 104 (2010) 313
- [4] J.-S. Huang, T. Feichtner, P. Biagioni, B. Hecht, *Nano Letters* 9 (5) (2009) 1897
- [5] M.W. Knight, H. Sobhani, P. Norlander, N.J. Halas, *Science* 332 (2011) 354
- [6] S. Lal, S. Link, N.J. Halas, *Nature Photonics* 1 (2007) 641
- [7] P. Muhlschlegel, H.J. Eisler, O.J.F. Martin, B. Hecht, D.W. Pohl, *Science* 308 (5728) (2005) 1607
- [8] G.A.E. Vandenbosch, V. Volski, N. Verellen, V.V. Moshchalkov, *Radio Science* 46 (2011) 547
- [9] T. Ishi, J. Fujikata, K. Makita, T. Baba, K. Ohashi, *Japanese Journal of Applied Physics* 44 (12–15) (2005) 364
- [10] A. Alu, N. Engheta, *Physical Review Letters* 101 (2008) 043901
- [11] A. Alu' 1, N. Engheta, *Physical Review B* 78 (2008) 195111
- [12] F.J. Gonzalez, et al., *Journal of Infrared Physics and Technology* 52 (2009) 48
- [13] J. Li, A. Salandrino, N. Engheta, *Physical Review B* 79 (2009) 195104
- [14] T. Kosako, Y. Kadoya, H.F. Hofmann, *Nature Photonics* 4 (2010) 312
- [15] D. Gevaux, *Nature Photonics* 1 (2007) 90
- [16] J. Alda, J. Rico-Garcia, J.M. Lopez-Alonso, G. Boreman, *Nanotechnology* 16 (2005) S230
- [17] B. Tian, C.M. Lieber, *Pure and Applied Chemistry* 83 (2011) 2153
- [18] Y. Dong, B. Tian, T. Kempa, C.M. Lieber, *Nano Letters* 9 (2009) 2183
- [19] B. Tian, T.J. Kempa, C.M. Lieber, *Chemical Society Reviews* 38 (2009) 16
- [20] R. Yu, Q. Lin, S.-F. Leung, Z. Fan, *Nano Energy* 1 (1) (2012) 57
- [21] M. Vrancken, G.A.E. Vandenbosch, *IEEE Transactions on Antennas and Propagation* 51 (10) (2003) 2778
- [22] Y. Schols, G.A.E. Vandenbosch, *IEEE Transactions on Antennas and Propagation* 55 (4) (2007) 1086
- [23] A. Vasylychenko, Y. Schols, W. De Raedt, G.A.E. Vandenbosch, *IEEE Antennas and Propagation Magazine* 51 (2009) 23
- [24] K. -O. Ong, J. Cheong, -F. Heong, *Experimental and Theoretical NANOTECHNOLOGY* 4 (2020) 11
- [25] F. Pelayo, G. De Arquer, V. Volski, N. Verellen, G.A.E. Vandenbosch, V.V. Moshchalkov, *IEEE Transactions on Antennas and Propagation* 59 (2011) 987

**Experimental and Theoretical
NANOTECHNOLOGY**

<http://etn.sciats.co.uk/>

Synthesis and characterization of ZnO nanoflowers under temperature effect

W. Smith¹, A. Becker², L. Harison^{1,*}

¹Micro Materials Ltd, Ellice Way, Wrexham LL13 7YL, UK

²Department of Materials Science, Universidad Politécnica de Madrid, 28040 Madrid, Spain

*) Email: lharris@micromaterials.co.uk

Received: 18/2/2020 / Accepted: 4/6/2020 / Published: 1/9/2020

Synthesis of flower-shaped ZnO nanostructures composed of hexagonal ZnO nanorods was achieved by the solution process using zinc acetate dihydrate and sodium hydroxide at very low temperature of 90 °C in 30 min. The individual nanorods are of hexagonal shape with sharp tip, and base diameter of about 300–350 nm. Detailed structural characterizations demonstrate that the synthesized products are single crystalline with the wurtzite hexagonal phase, grown along the [0 0 0 1] direction. The IR spectrum shows the standard peak of zinc oxide at 523 cm⁻¹. Raman scattering exhibits a sharp and strong E₂ mode at 437 cm⁻¹ which further confirms the good crystallinity and wurtzite hexagonal phase of the grown nanostructures. The photoelectron spectroscopic measurement shows the presence of Zn, O, C, zinc acetate and Na. The binding energy ca. 1021.2 eV (Zn 2p_{3/2}) and 1044.3 eV (Zn 2p_{1/2}), are found very close to the standard bulk ZnO binding energy values. The O 1s peak is found centered at 531.4 eV with a shoulder at 529.8 eV. Room-temperature photoluminescence (PL) demonstrate a strong and dominated peak at 381 nm with a suppressed and broad green emission at 515 nm, suggests that the flower-shaped ZnO nanostructures have good optical properties with very less structural defects.

Keywords: Synthesis; Characterization; ZnO.

1. INTRODUCTION

Controlled synthesis of semiconductor nanostructures in terms of size and shape has been strongly motivated as the properties can be tailored by shape and size and novel applications can be investigated dependent on their structural properties [1–4]. Among various semiconductor nanostructures, variety of nanostructures of ZnO has been investigated presenting it as a richest family of nanostructures [5]. With a wurtzite hexagonal phase, ZnO have a direct band gap of 3.37 eV with the larger exciton binding energy (60 meV), possesses a wide range of technological applications including transparent conducting electrodes of solar cells, flat panel displays, surface acoustic devices, UV lasers and chemical and biological sensors [6–10]. Various methods such as thermal evaporation [11], hydrothermal process [12], cyclic feeding chemical vapor deposition [13], chemical vapor deposition (CVD) [14], metal–organic CVD [15], etc. have been applied to grow nanostructures of ZnO. In addition to these, solution method can produce such structures, without using metal catalyst or templates, with better crystal quality preferably at lower growth temperature; as well it works out to be an easier and economical process.

Zhang et al. reported synthesis of flower-shaped, snowflakes, prism, prickly spheres and rod-like morphologies using $\text{Zn}(\text{OH})_4^{2-}$ or $\text{Zn}(\text{NH}_3)_4^{2-}$ as a precursor solutions (prepared in various solvents such as *n*-heptane, ethanol, water, etc.) at 180 °C for 13 h in a Teflon-lined autoclave [16]. Gao et al. reported the formation of flower-like ZnO nanostructures on silicon substrate at 95 °C in 60 min, by the thermolysis of ethylenediamine–zinc complex with the assistance of hexamethylenetetramine in a laboratory Pyrex glass bottle with polypropylene autoclavable screw caps with the filling ratio of 80% [17]. Umetsu et al. reported the synthesis of ZnO nanostructures with the assistance of artificial peptides, at room temperature. They researched that the peptides can assist in the homogeneous assembly of ZnO nanoparticles into unique flower-like morphologies [18]. Hocheplied et al. also synthesized the flower-shaped pom-pom-like particles from temperature-driven ammonia decomplexation at 85 °C in a 1 l water-jacketed thermostated reactor, stirred mechanically by a four-blade propeller at 500 rpm [19]. Yang et al. presented the synthesis of flower-shaped, disk and dumbbell-like ZnO structures by the assistance of capping molecules such as citric acid and poly vinyl alcohol. These structures were grown into Teflon-lined stainless-steel autoclaves at 200 °C in 20 h [20]. In all the results reported above, the nanostructures were either grown using capping molecules and/or additives at higher temperatures (95–200 °C) requiring higher growth time. In this paper we described the synthesis of flower-shaped ZnO nanostructures via solution process using the zinc acetate dihydrate and NaOH only as a source material at 90 °C for 30 min. We found this method to be a simple, cost effective, and convenient route to obtain larger quantity of nanostructured zinc oxide. The synthesized products were elucidated in terms of their structural, chemical and optical properties.

2. EXPERIMENTAL DETAILS

Synthesis was carried out by solution process at 90 °C using zinc acetate dihydrate and sodium hydroxide (NaOH), as source materials. All the chemicals were purchased from Aldrich Chemical Corporation and used without further purification. For synthesis, 6.57 g zinc acetate dihydrate ($\text{ZnAc}_2 \cdot 2\text{H}_2\text{O}$) was dissolved in 100 ml of de-ionized water under stirring at room temperature. Simultaneously, 3 M sodium hydroxide solution was added drop wise while stirring it continuously, resulting in a white milky precipitate. Before refluxing the solution, pH was measured as 13.2 by the expandable ion analyzer (EA 940, Orian). The solution was then transferred in a three-necked refluxing pot and refluxed at 90 °C for 30 min. The refluxing temperature was measured and controlled by k-type thermocouple and a PID temperature controller. While refluxing, the pH of the solution was not measured or controlled. After refluxing, the white powder was washed with methanol several times, dried at room temperature and was examined in terms of their structural, chemical and optical properties.

General morphologies and detailed structural characterizations were obtained using field emission scanning electron microscopy (FESEM). For SEM observation, the powder was uniformly sprayed on carbon tape. In order to avoid charging while observation, the powder was coated with thin platinum layer (10 nm). For the transmission electron microscopic measurement, powder was sonicated in ethanol for 10 min there by dipping copper grid in the solution and drying at room temperature. The crystallinity and crystal phases were determined by X-ray powder diffractometer (XRD) with Cu K α radiation (1.54178 Å) with Bragg angle ranging from 2 θ = 20° to 65°. The quality and composition of the synthesized flower-shaped ZnO nanostructures were characterized by the Fourier transform

infrared (FTIR) spectroscopy in the range of 400–4000 cm^{-1} . The surface states were analyzed by X-ray photoelectron spectroscopy (XPS, AXIS-NOVA, Kratos Inc.). Optical properties were analyzed by the UV–vis, Raman scattering and room temperature photoluminescence measurements.

3. RESULTS AND DISCUSSIONS

3.1 Detailed structural characterization of the flower-shaped ZnO nanostructures

Fig. 1 shows the general scanning electron morphologies of the synthesized structures. Fig. 1(a) and (b) shows the low magnification FESEM images whereas Fig. 1(c) and (d) presents the high magnification images of the grown

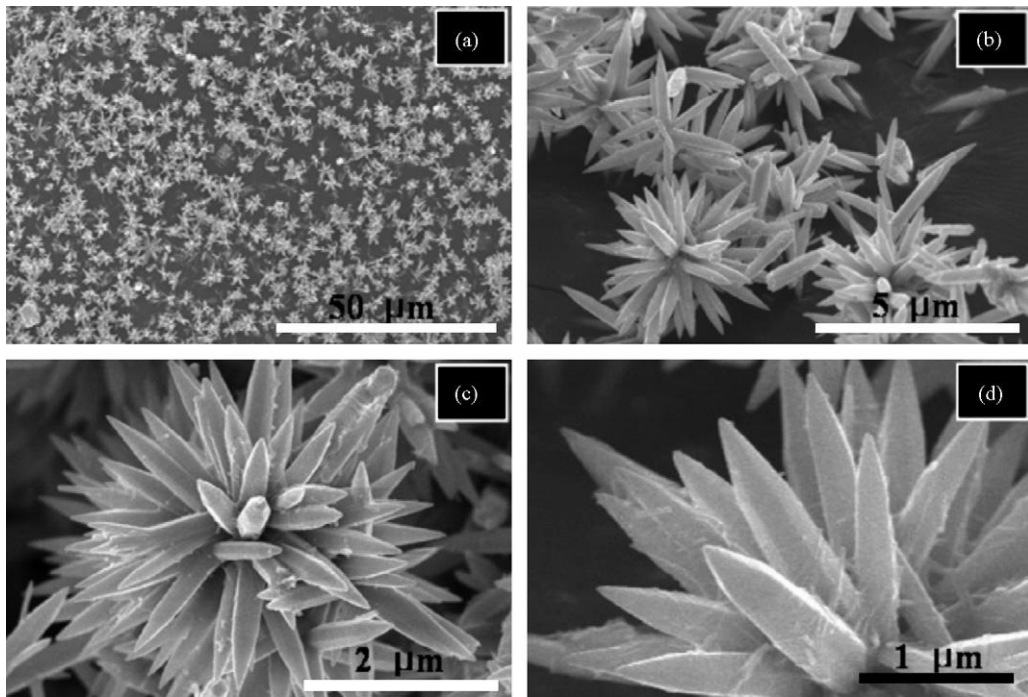


Figure 1 (a and b) Low and (c and d) high magnification FESEM images of flower-shaped ZnO nanostructures seen composed of hexagonal ZnO nanorods.

products. The images clearly reveal the flower-shaped structures that are composed of hexagonal nanorods. Magnified image shows that flower-shaped structures are constituted by the accumulation of several hundreds of sharp-tipped hexagonal ZnO nanorods. The typical diameters of these individual nanorods are in the range of 300–350 nm with the length of 2–4 μm . All the nanorods are seen originated from a single centre arranging them in a spherical shape exhibiting flower-like morphologies. The rod tip appears sharp with wide hexagonal-bases (Fig. 1(d)). The size of full array of a flower-shaped structure is in the range of 5–6 μm .

Fig. 2 presents the X-ray diffraction pattern of synthesized powder. All of the indexed peaks in the obtained spectrum are well matched with that of bulk ZnO (JCPDS Card No. 36–1451) which confirms that the synthesized powder is single crystalline and possesses a wurtzite hexagonal structure. No other peak related to impurities was

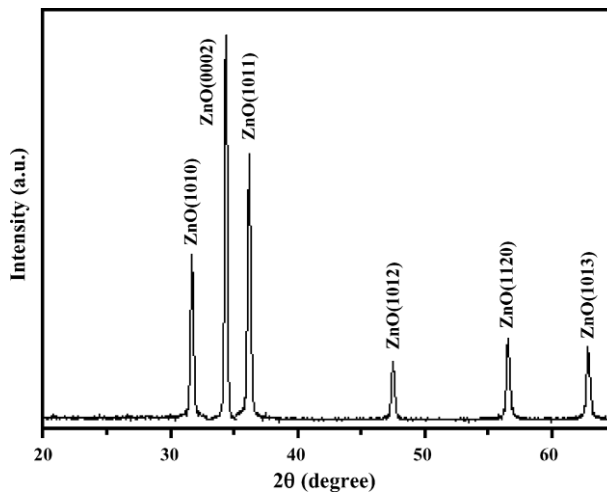


Figure 2 Typical X-ray diffraction (XRD) pattern synthesized nanostructure: the indexed peaks correspond to the wurtzite hexagonal phase.

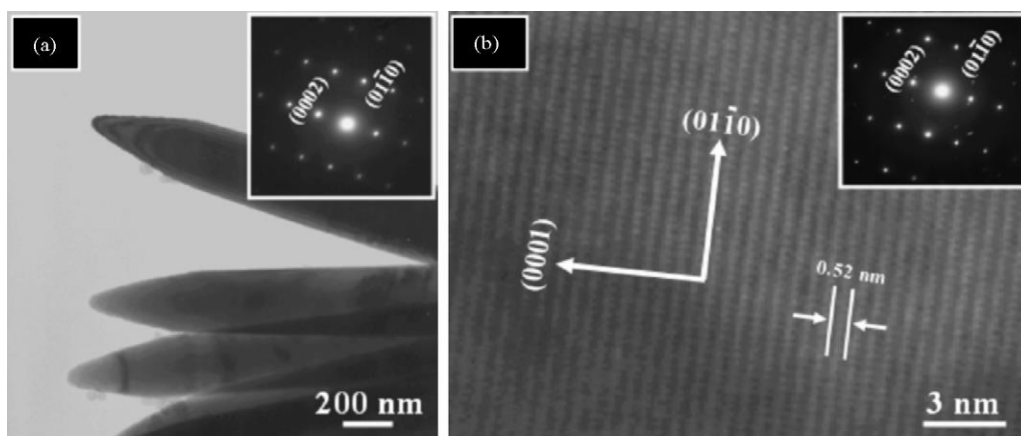


Figure 3 (a) Low magnification TEM image of the grown ZnO nanorods with their corresponding SAED pattern (inset). (b) HRTEM image showing the difference between two lattice fringes, which is about 0.52 nm. Corresponding SAED pattern (inset) is consistent with the HRTEM observation.

detected in the spectrum within the detection limit of the X-ray diffraction, which further confirms that the synthesized powders are pure ZnO. Additionally, higher intensity and narrower spectral width of ZnO (0 0 0 2) peak, compared to other observed ZnO peaks in the spectrum affirms the growth in *c*-axis direction.

Further structural characterization was carried out by the transmission electron microscopy (TEM) equipped with the selected area electron diffraction (SAED) setup. Fig. 3(a) shows the low magnification TEM image of the ZnO nanorods grown in the flower-shaped structures. The sharp tips and wider bases are clearly evident from this image. The base diameters are in the range of 300–350 nm. The corresponding SAED pattern obtained from the shown nanorods confirmed that the synthesized products are single crystalline and grew along the [0 0 0 1] direction (shown as inset in Fig. 3(a)). Fig. 3(b) shows the high resolution TEM (HRTEM) image of a nanorod. The lattice fringes between two adjacent planes is about 0.52 nm which is equal to the lattice constant of the ZnO which further indicate that the obtained structure have a wurtzite hexagonal phase and are preferentially grown along the *c*-axis [0 0 0 1] direction. The corresponding SAED pattern (inset in Fig. 3(b)) is consistent with the HRTEM observation.

The composition and quality of the product was analyzed by the FTIR spectroscopy. Fig. 4 shows the FTIR spectrum which was acquired in the range of 400–4000 cm^{-1} . The band at 523 cm^{-1} is correlated to zinc oxide [21]. The bands at 3200–3600 cm^{-1} correspond to O–H mode of vibration and the stretching mode of vibration of C–O is observed at 1431 and 1652 cm^{-1} . Fig. 5 shows the room temperature UV–vis absorption spectrum of the synthesized powder. A broad band was observed in the spectrum at 373 cm^{-1} which is a characteristic band for the wurtzite hexagonal pure ZnO. No other peak was observed in the spectrum confirms that the synthesized products are ZnO only [22].

The sample was also characterized by X-ray photoelectron spectroscopy (XPS) in order to understand chemical bonding state of element; the corresponding spectra are presented as Fig. 6. The peak positions were referenced to carbon at 284.6 eV. Fig. 6(a) shows the wide scan spectrum of the sample, where peaks of Zn, O, C, zinc acetate and Na were detected. The presence of C can be due to the atmospheric contamination and ambient exposure of the sample, whereas Na peak is due to the sodium hydroxide used while synthesis. The presence of zinc acetate peak indicates that the acetate compound remained on the surface, probably due to low temperature synthesis. We expect that annealing of the powder will remove acetate. Fig. 6(b) and (c) shows the narrow scan spectra for Zn 2p and O 1s regions, respectively. The doublet spectral lines of Zn 2p are observed at the binding energy of 1021.2 eV (Zn 2p_{3/2}) and 1044.3 eV (Zn 2p_{1/2}), which are very close to the standard bulk ZnO binding energy values [23]. The O 1s peak is found centered at 531.4 eV with a shoulder at 529.8 eV. The core level O 1s spectrum, fitted with Gaussian–Lorentz distribution (70:30 ratio) with Shirley type base line is shown in Fig. 6(c). The O 1s peak is found built-up of sub-peaks at 529.25, 531.2 and 532.2 eV. The peak with low binding energy (529.25 eV) corresponds to the O–H surface adsorbed group. The peak centered at 532.2 eV is attributed to O²⁻ in the oxygen vacancies on the ZnO structure, whereas the peak at 531.2 eV is correlated to ZnO [24].

The expected growth process of the flower-shaped ZnO nanostructures composed of hexagonal nanorods can be explained by the initial precipitation of the Zn(OH)₂. The formed Zn(OH)₂ dissolves to a considerable extent in water

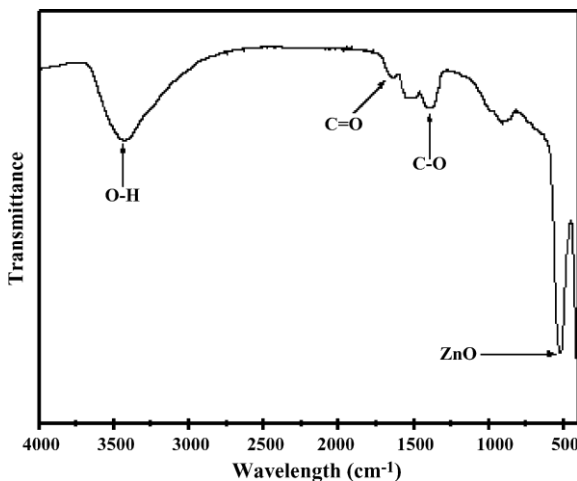


Figure 4 Typical FTIR spectrum of the synthesized nanostructure.

to form the Zn²⁺ and OH⁻ ions. Therefore, as the concentration of these Zn²⁺ and OH⁻ ions exceeds the critical value, the precipitation of ZnO nuclei starts. The transformation of the Zn(OH)₂ precipitates into the ZnO crystals proceed through these simple reactions:

The Zn(OH)₂ precipitates are more soluble as compared to the ZnO precipitates, hence the formed Zn(OH)₂ precipitate tends to produce continuously Zn²⁺ and OH⁻ ions which form the ZnO nuclei (I). The formed ZnO nuclei are expected to be the building blocks for the formation of the final products (II). Therefore, the ZnO nuclei concentration increases arranging themselves in a flower-shaped structure, due to surface energy.

The hexagonal nanorods with six defined facets arose to maintain the minimum surface energy as to keep the symmetry of the crystal structure (wurtzite ZnO). It is well known that the radii of newly formed crystal increase linearly with time after nuclei formation. As the new crystals grow, phase boundaries also increase at a given speed and eventually touch each other, forming the base of structure. Once base is formed, growth rate starts to decrease along the transverse direction and growth in the radial direction continues being the top surface an energetically favored surface.

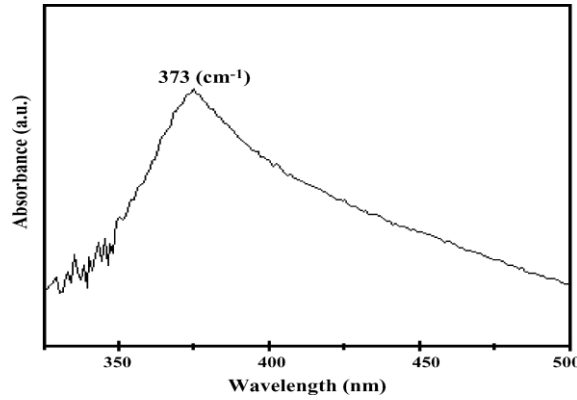


Fig. 5. Typical UV–vis spectrum of the synthesized nanostructure.

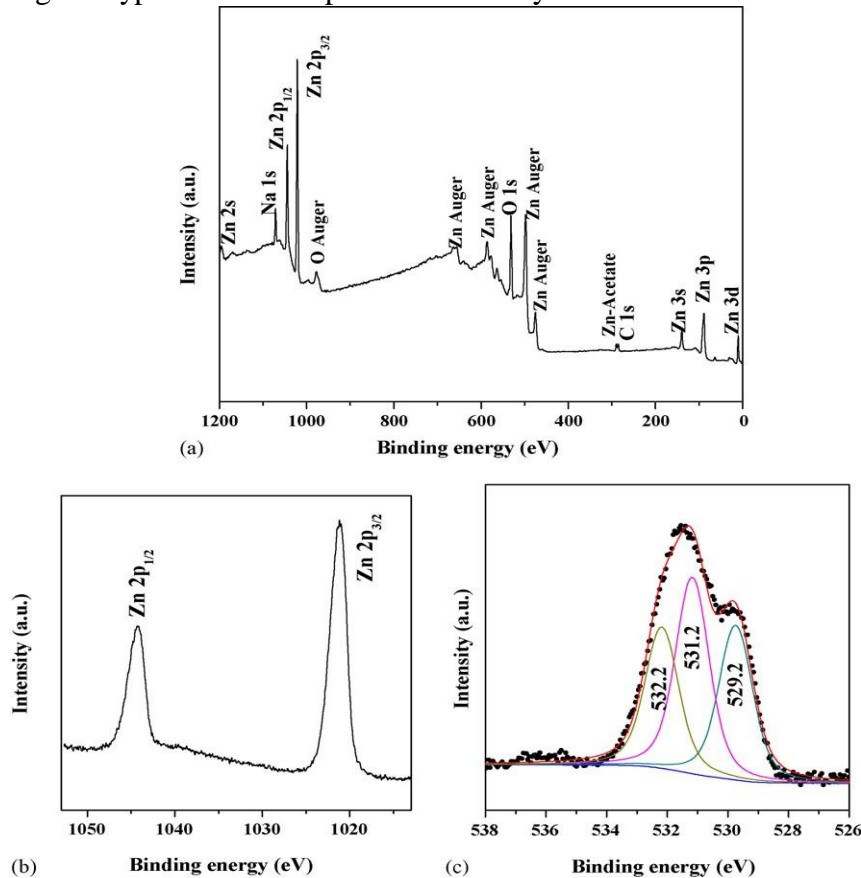


Figure 6 Photoelectron spectra of the synthesized powder: (a) wide scan survey, (b) core level spectrum for Zn 2p region and (c) core level O 1s spectrum, fitted with Gaussian–Lorentz distribution (70:30 ratio) with Shirley type base line.

Additionally as the ZnO is a polar crystal, where zinc and oxygen atoms are arranged alternatively along the *c*-axis and the top surfaces is Zn-terminated (0 0 0 1) while the bottom surfaces are oxygen-terminated (0 0 0 $\bar{1}$). The Zn- (0 0 0 1) is catalytically active while the O- (0 0 0 $\bar{1}$) is inert [25]. Therefore, the top surface would be energetically active. This will then help in growing in the radial direction once the nuclei are formed. The formation of tip at the edge is correlated to the different growth

velocities in different growth planes, as explained below.

The growths are also dependent upon the growth velocities of different growth planes in the ZnO crystals. Laudise and Ballman reported that the higher the growth rate, the quicker the disappearance of plane, which leads to the pointed shape in end of the *c*-axis [26]. In ZnO, the growth velocities of the ZnO crystals in different directions are $[0\ 0\ 1] > 0\ 1\ \bar{1}\ \bar{1} > 0\ 1\ \bar{1}\ 0 > 0\ 1\ \bar{1}\ 1 > 0\ 0\ 0\ \bar{1}$, under hydrothermal conditions [27]. Therefore, the (0 0 1) plane, the most rapid growth rate plane, disappears which leads to the pointed shape in an end of the (0 0 1) plane. Moreover, the $0\ 0\ 0\ \bar{1}$ plane has the slowest growth rate which leads to the plain shape in another end. In our synthesized nanostructures, all the observed nanorods have pointed tips with the flat down surfaces which is consistent with the growth habit of ZnO crystals.

3.2 Optical properties of the flower-shaped ZnO nanostructures

The optical properties of the synthesized flower-shaped ZnO nanostructures were observed by the Raman scattering and room-temperature photoluminescence measurements. The Raman spectra are sensitive to the crystal quality,

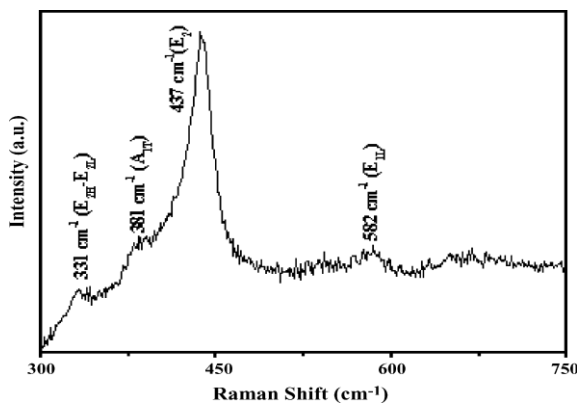


Figure 7 Typical Raman spectrum of the synthesized nanostructure.

structural defects and disorders of the grown products. With a wurtzite hexagonal, ZnO with two belongs to the C⁴

formula units per primitive cell. The primitive cell includes two formula units in which all the atoms are occupying the 2b sites of the C_{3v} symmetry. Group theory predicts, at the G point of the Brillouin zone, there is an existence of following optic modes: $G = A_1 + 2B_1 + E_1 + 2E_2$. The A_1 , E_1 and E_2 modes are Raman active. Furthermore, the A_1 and E_1 are infrared active and splits into longitudinal optical (LO) components and transverse optical (TO) components [28]. Fig. 7 shows the Raman spectrum of the synthesized powder. A sharp and strong peak at 437 cm^{-1} is observed which is attributed to the optical phonon E_2 mode of the ZnO and a characteristic Raman active peak for the wurtzite hexagonal phase of ZnO [29]. Furthermore, two very small peaks at 331 and 381 cm^{-1} are also observed in the spectrum which are assigned to be as $E_{2H}-E_{2L}$ (multi phonon process) and A_{1T} modes, respectively. Additionally, a very suppressed and short peak at 582 cm^{-1} is seen in the spectrum and attributed as E_{1L} mode [30,31]. The origination of E_{1L} mode in the Raman scattering is because of the impurities and structural defects (oxygen vacancies and Zn interstitials) of the synthesized products. Therefore, the presence of high intensity E_2 mode with the suppressed and very short E_{1L} peak in the Raman scattering indicate that the synthesized flower-shaped ZnO nanostructures are good in crystal quality and possesses the wurtzite hexagonal crystal structure.

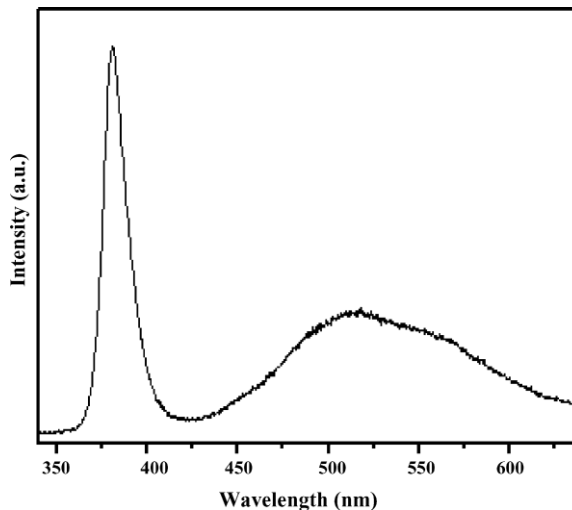


Figure 8 Room-temperature photoluminescence (PL) spectrum of the synthesized nanostructures acquired using a He–Cd laser-line with an excitation wavelength of 325 nm.

Fig. 8 shows the room-temperature photoluminescence spectrum of the synthesized powder. An intense, sharp and dominated peak at 380 nm in the UV region and a suppressed and broad band at 515 nm are observed. The UV emission, also called as near band edge emission, generated by the free-exciton recombination while the green emission, also known as deep level emission, appeared because of the impurities and structural defects in the deposited structures. The green emission is because of the recombination of electrons in single occupied oxygen vacancies in ZnO while the UV emission is because of the recombination of a photogenerated hole with an electron occupying the oxygen vacancies. Generally, high crystalline quality ZnO shows a

dominated UV emission with a weak green emission. Bagnall et al. reported that the crystal quality of the deposited ZnO is an important factor for the high UV emission and hence betterment in the crystal quality (less structural defects and impurities such as oxygen vacancies and zinc interstitials) may enhance the intensity of UV emission [32]. In our case, the near band edge emission is dominated over the deep level emission, which indicates that the grown nanostructures are good in crystal quality and exhibiting a good optical property.

4. CONCLUSIONS

Synthesis of flower-shaped ZnO nanostructures composed of hexagonal ZnO nanorods was achieved by the solution process using zinc acetate dihydrate and sodium hydroxide at low temperature, i.e. 90 °C in 30 min. Detailed structural characterizations demonstrate that the synthesized products are single crystalline with the wurtzite hexagonal phase, grown in the *c*-axis direction. The sharp tips and wider bases are clearly evident from SEM/TEM images. The base diameters are in the range of 300–350 nm. A photoelectron spectroscopic measurement shows the presence of Zn, O, C, zinc acetate and Na. The doublet spectral lines of Zn 2p are observed at the binding energy of 1021.2 eV (Zn 2p_{3/2}) and 1044.3 eV (Zn 2p_{1/2}), which are very close to the standard bulk ZnO binding energy values. The O 1s peak is found centered at 531.4 eV with a shoulder at 529.8 eV. The UV–vis, Raman scattering and room-temperature photoluminescence measurements indicate that the synthesized products are single crystalline ZnO exhibiting a good optical property.

References

- [1] Arafa H. Aly, Ahmed Mehaney, Shrouk Eid, *Experimental and Theoretical NANOTECHNOLOGY* 3 (2019) 19
- [2] W.J.E. Beek, M.M. Wienk, R.A.J. Janssen, *Adv. Mater.* 16 (2004) 1009
- [3] W.J.E. Beek, M.M. Wienk, M.K. Emerink, X. Yang, R.A.J. Janssen, *J. Phys. Chem. B* 109 (2005) 9505
- [4] Y. Xia, P. Yang, Y. Sun, Y. Wu, B. Mare, B. Gates, Y. Yin, F. Kim, H. Yan, *Adv. Mater.* 15 (2003) 323
- [5] Z.L. Wang, *Mater. Today* 7 (2004) 26
- [6] P. Zu, Z.K. Tang, G.K. Wong, M. Kawasaki, A. Ohtomo, H. Koinuma, Y. Segawa, *Solid State Commun.* 103 (1997) 459
- [7] D.M. Bangall, Y.G. Chen, Z. Zhu, T. Yao, *Appl. Phys. Lett.* 70 (1997) 2230
- [8] Y.C. Kong, D.P. Yu, B. Zhang, W. Fang, S.Q. Feng, *Appl. Phys. Lett.* 78 (2001) 407
- [9] Y. Li, G.W. Meng, L.D. Zhang, F. Philip, *Appl. Phys. Lett.* 76 (2000) 2011
- [10] K. Omichi, K. Kaiya, N. Takahashi, T. Nakamura, S. Okamoto, H. Yamamoto, *J. Mater. Chem.* 11 (2001) 262
- [11] H. Huang, Y. Wu, H. Feick, N. Tran, E. Weber, P. Yang, *Adv. Mater.* 13 (2001)

- [12] Y. Wang, M. Li, *Mater. Lett.* 60 (2006) 266
- [13] A. Umar, S. Lee, Y.S. Lee, K.S. Nahm, Y.B. Hahn, *J. Cryst. Growth* 277 (2005) 479
- [14] C.L. Wu, Li Chang, H.G. Chen, C.W. Lin, T.F. Chang, Y.C. Chao, J.K. Yan, *Thin Solid Films* 498 (2006) 137
- [15] J.Y. Park, H. Oh, J.-J. Kim, S.S. Kim, *J. Cryst. Growth* 287 (2006) 145
- [16] J. Zhang, et al. *Chem. Mater.* 12 (2002) 4172
- [17] X. Gao, X. Li, W. Yu, *J. Solid State Chem.* 178 (2005) 1139
- [18] M. Umetsu, M. Mizuta, K. Tsumoto, S. Ohra, S. Takami, H. Watanabe, I. Kumagaiand, T. Adschiri, *Adv. Mater.* 17 (2005) 2571
- [19] J.F. Hochepped, A.P.A. Oliveira, V.G. Ferrol, J.F. Tranchant, *J. Cryst. Growth* 282 (2005) 156a
- [20] H. Zhang, D. Yang, D. Li, X. Ma, S. Li, D. Que, *Cryst. Growth Des.* 5 (2005) 547
- [21] W. Lili, W. Youshi, S. Yuanchang, W. Huiying, *Rare Metals* 25 (2006) 68
- [22] Y.H. Ni, X.W. Wei, J.M. Hong, Y. Ye, *Mater. Sci. Eng. B* 121 (2005) 42
- [23] B. Vincent Crist, *Handbook of Monochromatic XPS Spectra: The Elements and Native Oxides*, John Wiley & Sons, England, 2000, p. 510
- [24] http://srdata.nist.gov/xps/bind_e_detail_indv.asp?ID1=22608
- [25] P.X. Gao, Z.L. Wang, *J. Phys. Chem. B* 108 (2004) 7534
- [26] R.A. Laudise, A.A. Ballman, *J. Phys. Chem.* 64 (1960) 688
- [27] W.J. Li, E.W. Shi, M.Y. Tian, B.G. Wang, W.Z. Zhong, *Sci. China E* 28 (1998) 212
- [28] T.C. Damen, S.P.S. Porto, *B. Tell, Phys. Rev.* 142 (1966) 142
- [29] Y.J. Xing, Z.H. Xi, Z.Q. Xue, X.D. Zhang, J.H. Song, R.M. Wang, J. Xu, Y. Song, S.L. Zhang, D.P. Yu, *Appl. Phys. Lett.* 83 (2003) 1689
- [30] M. Rajalakshmi, A.K. Arora, B.S. Bendre, S. Mahamuni, *J. Appl. Phys.* 87 (2000) 2445
- [31] K. Vanheusden, C.H. Seager, W.L. Warren, D.R. Tallant, J.A. Voigt, *J. Appl. Phys.* 79 (1996) 7983
- [32] D.M. Bagnall, Y.F. Chen, Z. Zhu, T. Yao, S. Koyama, M.Y. Shen, T. Goto, *Appl. Phys. Lett.* 73 (1998) 1038

Optical and structural of Nanocrystalline CdS

A. Kumar, R. Vasantha*

School of Mechanical Engineering, Kalinga Institute of Industrial Technology (KIIT),
Deemed to be University, Bhubaneswar 24, Odisha, India

*) Email: vasaritha@yahoo.co.in

Received: 3/3/2020 / Accepted: 4/7/2020 / Published: 1/9/2020

Nanocrystalline CdS thin films have been deposited using precursors with different thiourea concentration onto glass substrates by sol-gel spin coating method. The crystalline nature of the films has been observed to be strongly dependent on thiourea concentration and annealing temperature. The CdS films are found to be nanocrystalline in nature with hexagonal structure. The grain size is found to be in the range of 7.6 to 11.5 nm depending on the thiourea concentration and annealing temperature. The high-resolution transmission electron microscopy (HRTEM) results of the CdS films prepared using cadmium to thiourea molar ratio of 0.3:0.3 indicate the formation of nanocrystalline CdS with grain size of 5 nm. Fourier transform infrared (FTIR) analysis shows the absorption bands corresponding to Cd and S. The optical study carried out to determine the band gap of the nanostructured CdS thin films shows a strong blue shift. The band gap energy has been observed to lie in the range of 3.97 to 3.62 eV following closely the quantum confinement dependence of energy on crystallite radius. The dependence of band gap of the CdS films on the annealing temperature and thiourea concentration has also been studied. The photoluminescence (PL) spectra display two main emission peaks corresponding to the blue and green emissions of CdS.

Keywords: Sol-gel; CdS; HRTEM, Nanocrystalline.

1. INTRODUCTION

CdTe thin film solar cells are usually fabricated as hetero-structures because of the short absorption length and difficulty in forming a shallow thin film junction with a high conductivity surface layer [1]. The hetero-junction partner or the window material to CdTe should have a large band gap and good lattice and electron affinity match to minimize interface states and avoid deleterious conduction band spikes. Among the various heterojunction window materials available today, CdS is the one, which is most extensively studied and is

best suited for CdTe solar cells [2]. Capoen et al. [3] have reported that CdS nanoparticles have low refractive index compared to the bulk due to the quantum confinement effect and have also stated that the CdS layers exhibit wave guiding properties. CdS is one of the most important II-VI semiconductor compounds possessing excellent optical properties. A tremendous amount of effort has been devoted to the synthesis and study of optical properties of CdS related nanoparticles and quantum dots [4]. The quantum dots are considered as promising candidates for optoelectronic applications including light emitting diodes [5] and optically pumped high power blue lasers [6]. Various concepts have been proposed for the use of nanostructured materials in solar energy conversion [7] Quantum dots can be used as frequency converters to match the spectrum of the incoming radiation to the spectral efficiency of the solar cell [8]. Devi et al. [9] have reported that the grain size and band gap of CdS depend on the molar ratio of Cd and S used in the preparation of CdS. Ramaiah et al. [10] have reported that higher sulphur concentration increases the grain size and decreases the band gap of CdS. The behavior of CdS quantum dots depending on the quantum confinement effect presents in the material. The quantum size effect is theoretically classified into two types: one is the exciton confinement effect and the other is the independent confinement effect of electron and hole. When the radius of the microcrystal is sufficiently larger than the exciton Bohr radius, the exciton confinement effect occurs. On the other hand, when the radius is comparable or smaller than the exciton Bohr radius, the independent confinement of electrons and holes takes place [11].

CdS thin films have been prepared by different workers using various techniques such as brush plating [12], pulsed laser deposition [13], physical vapor deposition [14], chemical bath deposition [15], spray pyrolysis [16], successive ionic layer adsorption and reaction [17], screen printing [18]. The sol-gel technique is extensively studied as a matrix material method to produce nanocomposites because it gives a higher specific surface area, superior homogeneity and purity, better microstructural control of metallic particles, narrow pore size and uniform particle distribution. In addition, the sol-gel method also offers several other advantages, such as low temperature processing, possibility of coating on large area substrates and most importantly cost-effective. In this paper, we report about the effect of thiourea concentration and annealing temperature on the structural properties, surface morphology and optical properties of the CdS nanocrystalline thin films prepared using sol gel spin coating method.

2. EXPERIMENTAL

In the present study, CdS particles were embedded in polyethylene glycol-based solution. A polyethylene glycol (PEG 400, Merck) sol was prepared by mix X-ray diffraction (XRD) studies were carried out on the prepared CdS films using Panalytical x-ray diffractometer (Netherlands), and high-resolution transmission electron microscopy (HRTEM) images of the prepared CdS films were recorded using a Philips TECNAI F20 microscope (USA). The surface morphology of the films was studied by scanning electron microscopy (SEM) using a Hitachi S-500 microscope (Japan). The chemical composition of the samples was determined using an energy dispersive x-ray analysis (EDX) spectrometer attached to the scanning electron microscope, and Fourier transform infrared (FTIR) spectrum was recorded using a Shimadzu spectrometer (Japan). The optical properties were studied using the absorbance spectrum recorded by spectrophotometer (JASCO V-570), and the photoluminescence spectra were recorded using the Cary Eclipse WinFLR photoluminescence device (USA).

3. RESULTS AND DISCUSSION

In the preparation of CdS thin films by solution growth method, the film growth can take place by one of the following methods [19,20]. One is the cluster by cluster mechanism described as follows: in the ammonia-thiourea system, S^{2-} ions are released by the alkaline hydrolysis of thiourea and Cd^{2+} ions are released by dissociation of the corresponding ammonia complexes. As soon as the product of the free S^{2-} and Cd^{2+} ion concentration exceeds the solubility product of CdS, the precipitation of CdS takes place. The other method is the ion by ion mechanism which consists of the following three steps: (i) the reversible adsorption on the substrate surface of dihydroxo-diamino cadmium, (ii) the adsorption of thiourea by the formation of a metastable complex, (iii) the formation of CdS and site regeneration by the metastable complex decomposition. Generally, the formation of CdS films is observed to take place by ion mechanism.

Table 1 Interplanar distance (d) values of (002) crystal plane of CdS thin films.

Solution Cd:S	Thin film Cd:S	Annealing temperature/ $^{\circ}$ C	Experimental, d/nm	CdS hexagonal (JCPDS 6-314)	
				d/nm	(hkl)
0.3:0.3	1.0:0.66	250	0.336	0.336	(002)
		450	0.339		
0.3:0.4	1.0:0.75	250	0.338		
		450	0.339		
0.3:0.6	1.0:0.92	250	0.336		
		450	0.336		

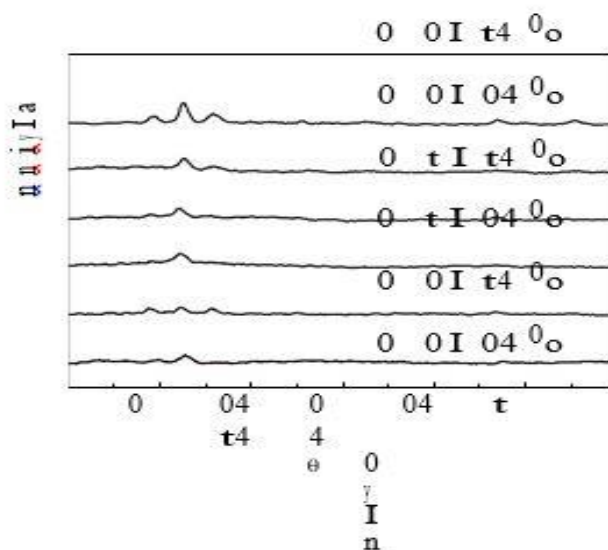


Figure 1 XRD patterns of annealed CdS films deposited Cd:S molar ratio of 0.3:0.3, 0.3:0.4 and 0.3:0.6.

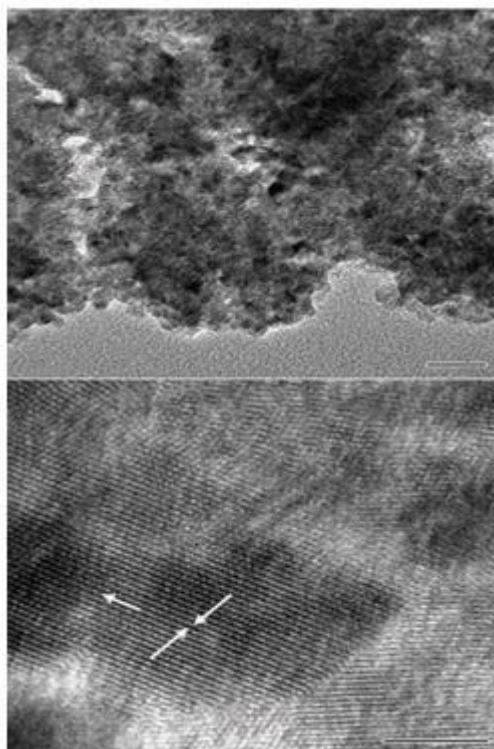


Figure 2 HRTEM images of annealed CdS film prepared using Cd:S molar ratio of 0.3:0.3.

CuK α radiation. Figure 1 shows the XRD patterns of CdS thin films prepared using three different thiourea concentrations (0.3, 0.4 and 0.6 mol/L) and annealed at 250 and 450° C for 45 min. Peaks are observed at 24.63, 26.26, 28.02 and 43.5 deg. corresponding to the (100), (002), (101) and (110) planes of the hexagonal phase of CdS. The intensity of the peaks is observed to increase as the ratio of Cd/S is decreased. Additional peak corresponding to unreacted Cd or S has not been observed. For comparison, the obtained interplanar spacing (d) values of CdS films along with Joint Committee on Powder Diffraction Standards (JCPDS) data are given in Table 1. The lattice parameter values a and c have been calculated to be 0.441 and 0.672 nm, respectively, and these values are in agreement with the JCPDS data (6-314). The crystallite size has been determined from the width of the XRD peak at 26.26 deg. using Scherrer's equation [22] and is listed in Table 1. With the increase of temperature and thiourea concentration, there is an increase in the intensity of the peak, and this is due to the improvement in the crystalline nature of the films. The grain size is found to be in the range of 7.6 to 14.5 nm.

Figure 2 shows the HRTEM images of CdS prepared using a sulphur concentration of 0.3 mol/L and annealed at a temperature of 250° C. The image clearly shows lattice fringes corresponding to hexagonal CdS phase. The interplanar lattice spacing of the planes seen is 0.357 nm corresponding to the (100) plane of hexagonal phase. The HRTEM image gives a grain size of about 5 nm and this is in agreement with XRD results. This confirms the formation of nanocrystalline CdS films with particle size lying in the quantum dot range.

SEM is a convenient technique to study the surface morphology of thin films. Figure 3 shows the surface morphology of CdS thin films prepared using three different thiourea concentrations (0.3, 0.4 and 0.6 mol/L) and annealed at 250° C. A large number of cavities seen in the images may be due to the prolonged drying resulting in the evaporation of the solvent. Evaporation of the solvent from the gel film affects the film morphology. A sol film is required to have a sufficient fluidity for some time during the drying process to form macroporous structure. Evaporation rate of the gel film is determined mainly by transport rate of the top surface of the film and is in dependent of the film thickness [23]

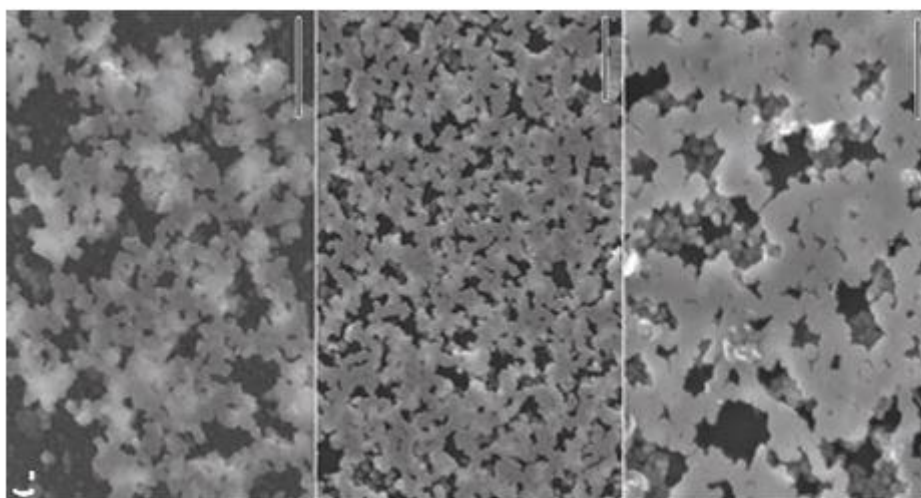


Figure 3 SEM images of 250° C annealed CdS films prepared using Cd:S molar ratio 0.3:0.3 (a), 0.3:0.4 (b) and 0.3:0.6 (c).

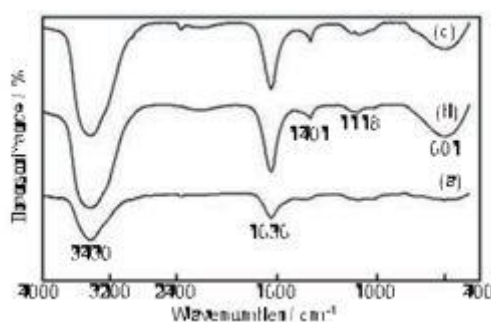


Figure 4 FTIR spectrum of 450° C annealed CdS films: (a) Cd:S=0.3:0.3, (b) Cd:S=0.3:0.4, (c) Cd:S=0.3:0.6

Generally during the film formation, PEG interacts with Cd²⁺ ions and self-assembles through cross-linking and polymerization to form ordered inorganic/polymer composites. As a result, in the SEM pictures, we see the nanostructured inorganic matrix with CdS nanoparticles and their agglomerates. The distribution of Cd²⁺ cations in the polymer chains is a result of the

interaction of the Cd²⁺ ions with the functional groups of PEG. The morphology observed may be due to the rearrangement of the polymer chains at molecular level that occurs due to the interaction between lone electron pairs belonging to oxygen atoms from the functional groups of PEG and the metal ions. Kajihara and Yao [24] have reported that decomposition of PEG is the reason for the variation of macroscopic morphology.

EDX analysis carried out to study the composition of the films revealed that the Cd/S ratio in the grown films increased with increasing Cd/S concentration ratio in the solution as expected. The composition of the prepared CdS films is shown in Table 1. Figure 4 shows the FTIR spectrum of 450° C annealed CdS films (Cd:S=0.3:0.3, 0.3:0.4, 0.3:0.6). The absorption band present at 3430 cm⁻¹ is due to OH stretching vibration of water molecules. The band at 1636 and 1401 cm⁻¹ results from aromatic C-C stretches. The γ (SO₂) stretching mode at 1118 cm⁻¹ is also observed, confirming the successful incorporation of the sulfonic group [25]. The band at 601 cm⁻¹ corresponds to the Cd-S stretching.

Optical absorbance spectra of the CdS thin films have been recorded in the wavelength range 300–1800 nm. It is well known that for semiconductor particles with radius less than the bulk Bohr exciton radius, there is a blue shift in the absorption edge due to the quantum size effect [22]. Excitons have an average physical separation between the electron and hole, referred to as the exciton Bohr radius, and this physical distance is different for each material. In bulk, the dimension of the semiconductor crystal is much larger than the exciton Bohr radius, allowing the exciton to extend to its natural limit.

However, if the size of a semiconductor crystal becomes small enough, i.e., it approaches the size of the materials exciton Bohr radius, then the electron energy levels can no longer be treated as continuous and they must be treated as discrete. This situation of discrete energy levels is called quantum confinement, and under these conditions, the semiconductor material ceases to resemble bulk, and instead can be called a quantum dot. This has large repercussions on the absorptive and emissive behavior of the semiconductor material. Because the electron energy levels of quantum dots are discrete rather than continuous, the addition or subtraction of just a few atoms to the quantum dot has the effect of altering the boundaries of the band gap. Changing the geometry of the surface of the quantum dot also changes the band gap energy due to the small size of the dot and the effects of quantum confinement. The band gap in a quantum dot will always be energetically larger; therefore, we refer to the radiation from quantum dots to blue shift reflecting the fact that electrons must fall a greater distance in terms of energy and thus produce radiation of a shorter and therefore a blue wavelength. The size dependence of the electronic structure of the lowest exciton states in CdS quantum dots is mainly determined by two terms: the spin-orbit interaction and the electron-hole (e-h) exchange interaction. Matrix elements of the spin-orbit interaction are constant and the e-h exchange interaction increases as the quantum dot radius decreases. Two opposite limits can be considered: small and large dots. For small quantum dots, the e-h exchange interaction is much larger than the spin-orbit coupling, and for large quantum dots, the e-h exchange interaction is much smaller than the spin-orbit coupling.

Table 2 Particle size of CdS films obtained from XRD pattern and blue shift of optical band gap

Solution Cd:S	Annealing temperature/ ^o C	E _g /eV	Particle size from blue shift/nm	Particle size from XRD/nm
0.3:0.3	250	3.97	7.58	7.6
450		3.90	7.75	9.3
0.3:0.4	250	3.89	7.78	9.8
450		3.78	8.09	11.7
0.3:0.6	250	3.75	8.18	12.2
450		3.62	8.66	14.5

4. CONCLUSION

Nanostructured CdS thin films have been deposited using different Cd/S concentration ratio. The XRD analysis indicates that the films are nanocrystalline in nature with hexagonal structure and the grain size is found to be less than 10 nm indicating the formation of CdS quantum dots. The particle size has been calculated using the blue shift of the optical band gap caused by quantum confinement and is shown in Table 2. The particle size is found to lie in the range of 7.58 to 8.66 nm. The strong and weak confinements occur from the small and large grains present in the sample, respectively. The blue shift suggests strong quantum confinement. The optical band gap values of 3.97 to 3.62 eV obtained from strong confinement could be due to the small size of grains. The formation of CdS nanoparticles can be also confirmed by photoluminescence (PL) spectroscopy, because CdS nanoparticles exhibit light-emitting due to quantum confinement effects arising due to the formation of very small CdS particles. The next stage of work is the optimization of the size of CdS particles for quantum dot solar cell applications.

References

- [1] Bisma Bilal, Suhaib Ahmed, Vipin Kakkar, Experimental and Theoretical NANOTECHNOLOGY 3 (2019) 33
- [2] C. Ferekides and J. Britt: Sol. Energy Mater. Sol. Cells 35 (1994) 255
- [3] C. Capoen, T. Gacoin, J. M. Nedelec, S. Turrell, M. Bouazaoui, J. Mater. Sci., 36 (2001) 2565
- [4] A. Blanco, C. Lopez, R. Mayoral, H. Miguez, F. Meseguer, A. Mitsud, J. Herrero, Appl. Phys. Lett. 73 (1998) 178
- [5] V. Tasco, M.T. Todaro, M.D. Giorgi, R. Cingolani, P. Passaseo, J. Ratajczak, J.W. Katcki, Appl. Phys. Lett. 84 (2004) 4155
- [6] Q. Darugar, W. Qian, M.A. EI-Sayed, Appl. Phys. Lett. 88 (2006) 261108
- [7] P. Oelhafen, A. Schuler: Sol. Energy 79 (2005) 110
- [8] W.G.J.H.M. Van Sark, A. Meijerink, R.E.I. Schropp, J.A.M. Van Roozmalen, E.H. Lysen, Sol. Energy Mater. Sol. Cells 87 (2005) 395
- [9] R. Devi, P. Purkayastha, P.K. Kalita, B.K. Sarma: Bull. Mat. Sci. 30 (2007) 123
- [10] K.S. Ramaiah, A.K. Bhatnagar, R.D. Pilkington, A.E. Hill, R.D. Tomlinson, J. Mater.

Sci. Mater. Elec- tron. 11 (2000) 269

[11] H. Nasu, J. Matsuoka, Kamiya: J. Non-Cryst. Solids 178 (1994) 148

[12] K.R. Murali, S. Kumaresan and J. Joseph Prince, J.Mater. Sci. Mater. Electron. 18 (2007) 487

[13] X.L. Tong, D.S. Jiang, W.B. Hu, Z.M. Liu, M.Z.Luo, Appl. Phys. A, 2006, 84, 143.

[14] R.W. Birkmire, B.E. McCandless, S.S. Hegedus, Sol. Energy, 1992, 12, 45.

[15] B. Pradhan, A.K. Sharma, A.K. Ray, J. Cryst.Growth, 2007, 304, 388.

[16] P. Raji, C. Sanjeeviraja, K. Ramachandran, Bull.Mater. Sci., 2005, 28, 233.

[17] Y.A. Kalandaragh, M.B. Muradov, R.K. Mammedov, A. Kaodayari J. Cryst. Growth 305 (2007) 175

[18] D. Patidar, R. Sharma, N. Jani, T.P. Sharma, N.S. Saxena, Bull. Mater. Sci. 29 (2006) 21

[19] J.M. Dona, J. Herrero, J. Electrochem. Soc. 144 (1997) 408

[20] R. Ortega-Borges, D. Lincol, J. Electrochem. Soc. 140 (1993) 3464

[21] I. Kaur, D.K. Pandya, K.L. Chopra, J. Elec- trochem. Soc. 127 (1980) 943

[22] M. Maleki, M.S. Ghamsari, Sh. Mirdamadi, R.Ghasemzadeh, Semicond. Phys., Quantum Electron. Optoelectron. 10 (2007) 30

[23] K. Kajihara, K. Nakanishi, K. Tanaka, K. Hirao, N. Soga, J. Am. Ceram. Soc. 81 (1998) 2670

[24] K. Kajihara, T. Yao, J. Sol-Gel Sci. Technol. 17 (2000) 173

[25] T.P. Martin, H. Schaber: Spectroc. Acta Pt. A- Molec. Biomolec. Spectr. 38 (1980) 655

Optical properties of reduced graphene oxide sheets

*J-S. Lim, Z-H. Jim**

Nano Materials and System Lab, Department of Mechanical, Engineering, Jeju National University, Jeju 690-756, South Korea

*) Email: jimzh@jejunu.ac.kr

Received: 8/4/2020 / Accepted: 7/8/2020 / Published: 1/9/2020

In this paper, we are investigating the Raman and photoluminescence properties of reduced graphene oxide sheets (rGO). Moreover, graphene oxide (GO) sheets are synthesized using Hummer's method and further reduced into graphene sheets using D-galactose. Both GO and rGO are characterized by UV-vis spectroscopy, X-ray diffraction (XRD), X-ray photoelectron spectroscopy (XPS) and Thermogravimetric (TGA) analysis. Raman analysis of rGO shows the restoration of graphitic domains in GO after reduction. The photoluminescence of rGO showed emission in the UV region which is blue shifted along with luminescent quenching as compared to GO. This blue shift and quenching in photoluminescence arise due to the newly formed crystalline sp² clusters in rGO which created percolation pathways between the sp²

Clusters already present.

Keywords: GO; Analysis; Optical.

1. INTRODUCTION

Graphene is a single sheet of carbon atoms tightly packed into a two-dimensional (2D) honeycomb lattice [1]. Graphene sheets are of significance in fundamental and applied science due to their exceptional electronic, tunable band gap, high mobility, mechanical, and thermal properties [2, 3]. These unique properties of graphene are promising for applications in various fields such as nanoelectronics, nanocomposites, gas sensors, batteries and hydrogen storage [4, 5]. In this regard, an outstanding challenge is to integrate photonic and band-gap manipulation. Since graphene has no band gap, photoluminescence is not expected from relaxed charge carriers [6], but it can be made luminescent mainly by two ways viz. (i) by cutting into ribbons and quantum dots [7] and (ii) by physical or chemical treatments [8]. Previous report on graphene nanoribbons with various band gaps exhibited no photoluminescence [9]. Some of the reports show that graphene can be made luminescent by oxygen plasma treatment [10]. Similarly, chemically synthesized graphene oxide (GO) exhibits a broad photoluminescence where the electronic structure has been modified [11]. GO is basically insulating and highly disordered compared to the crystalline graphene. But the availability of various oxygen-

containing functional groups with both sp^2 and sp^3 carbon sites made them attractive towards synthesis of large-scale production of graphene by suitable reduction kinetics. The band gap of GO can be tunable by varying the oxidation level [12]. Even though GO is formed from the oxidation of graphite, still it have some sp^2 carbon atoms in its structure. The density-functional studies on GO show the presence of graphitic domains in the GO which produce quantum confinement effects in GO [13]. The property of graphene can be altered by suitable reduction process of GO by controlling the fractions of sp^2 to sp^3 clusters and resulting in transition from insulator to semiconductor and to a metal [14]. Therefore, it is expected that the optical properties of the graphene sheets can be tuned by the reducing GO into reduced graphene oxide sheets (rGO) by altering the sp^2 to sp^3 ratio.

In these aspects, we are investigating the optical properties of reduced graphene oxide sheets using Raman and photoluminescence spectroscopy. The GO nanosheets are synthesized according to Hummer's method and are successfully reduced using D-galactose into rGO nanosheets. The use of D-galactose is due to its non-toxicity over the conventional chemical reducing agents such as hydrazine and hydrazine hydrate and also in order to avoid agglomeration of graphene sheets [15, 16]. Both GO and rGO are characterized using physico-chemical techniques and their photoluminescence properties before and after reduction are discussed in detail.

2 EXPERIMENTAL

2.1 Synthesis of graphene oxide

GO was synthesized by harsh oxidation of graphite powder using the modified Hummer's method which results in a brownish colloidal suspension [17]. Briefly, the expandable graphite powders (2 g) were stirred in 98% H_2SO_4 (35 mL) for 2 h. Subsequently, $KMnO_4$ (6 g) was gradually added to the above solution while keeping the temperature less than $20^\circ C$. The mixture was then stirred at $35^\circ C$ for 2 hours. The resulting solution was diluted by adding 90 mL of water under vigorous stirring and a dark brown suspension was obtained. The suspension was further treated by adding 30% H_2O_2 solution (10 mL) and 150 mL of distilled water. The resulting graphite oxide suspension was washed by repeated centrifugation, first with 5% HCl aqueous solution and then with distilled water until the pH of the solution becomes neutral. The GO nanostructures were obtained by adding 160 mL of water to the resulting precipitate and sonicated well to attain a uniform suspension of GO.

2.2 Synthesis of reduced graphene oxide

The rGO was synthesized from GO using an eco-friendly method by employing galactose as a reducing agent. Briefly, galactose (0.4 g) is gradually added to the aqueous solution of GO (0.5 mg/mL) and is treated by constant stirring for 30 min, resulting in a color change from brown to black. Then, 0.2 mL of ammonia is added to the solution and it is allowed to heat at $70^\circ C$ for 1 hour. Finally, the black precipitate of rGO obtained was centrifuged at an rpm of 5000 and washed three times with deionized water.

2.3 Characterization

The UV-vis spectroscopy was performed using Hewlett Packard HP-8453 spectrophotometer. The phase purity and crystallinity of the GO and rGO were determined by X-ray diffraction (XRD) recorded on X-ray diffractometer system (D/MAX 2200H, Bede 200, Rigaku Instruments C). The X-ray photoelectron spectroscopy (XPS) measurements were carried out on ESCA 2000 VG Microtech systems. The Raman spectra were recorded with a RENISHAW (M005-141) Raman system with laser frequency of 514 nm as excitation source. The laser spot size was 1 μm , and the power at the sample was below 10 mW, in order to avoid laser-induced heating. Thermogravimetric analysis (TGA) was carried out using Perkin-Elmer instrument. Photoluminescence (PL) spectra of GO and rGO were measured by Cary Eclipse Fluorescence Spectrophotometer.

3. RESULTS AND DISCUSSION

In this work, GO was synthesized according to the modified Hummer's method and their characterization were discussed in detail in our previous report [17]. The reduction reaction of graphene oxide into graphene sheets was monitored by the color change from brown into black as shown in the inset of Fig. 1(a) followed by the UV-vis spectroscopy. The black color of the rGO material suggested the re-graphitization of the exfoliated GO by the removal of oxygenated functional groups. Figure 1(a) depicts the UV-vis spectra of the GO, showing a sharp absorption peak at 226 nm, which is attributed to the $\pi-\pi^*$ of the C-C aromatic rings [18]. After the reduction of GO, the absorption peak was red shifted towards into 272 nm due to the formation of rGO. This is in agreement with previous reports on rGO [19]. The significant red shift in rGO is due to the increased electron concentration, structural ordering and consistent with the restoration of sp^2 carbon atoms [20].

Figure 1(b) shows the XRD pattern of graphite, GO and rGO, respectively. The diffraction peak of pure graphite is found around 26° [21]. After successful oxidation, the diffraction peak of GO shifted towards $2\theta = 10^\circ$ which is mainly due to the oxidation of graphite and the corresponding interlayer spacing was 0.85 nm [22]. The reduction of graphene oxide into rGO is also confirmed by the XRD pattern of rGO which shows a broad diffraction peak at $2\theta = 26^\circ$ corresponding to the interlayer spacing of 0.35 nm. The complete disappearance of a peak at $2\theta = 10^\circ$ of the GO and the formation of new broad peak at $2\theta = 26^\circ$ further supports that the graphene oxide is completely reduced into rGO [16]. Figure 2 shows the TEM image of the reduced graphene oxide showing sheet-like morphology which is transparent and wrinkled at the edges. The removal of oxygenated functional groups from GO after reduction into graphene is studied by XPS technique as shown in Fig. 3. XPS of GO exhibits the following peaks: at 284.8, 285.55, 286.8 and 288.65 eV, corresponding to the C-C in the aromatic rings, hydroxyl, epoxy and carbonyl

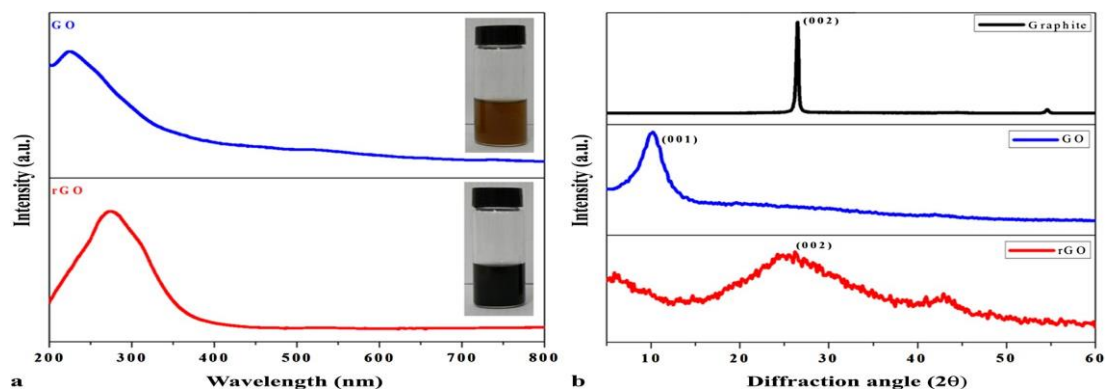


Figure 1 (a) UV-vis spectra of GO and rGO. The photographs correspond to the water dispersed GO and rGO. (b) XRD pattern of graphite, GO and rGO.

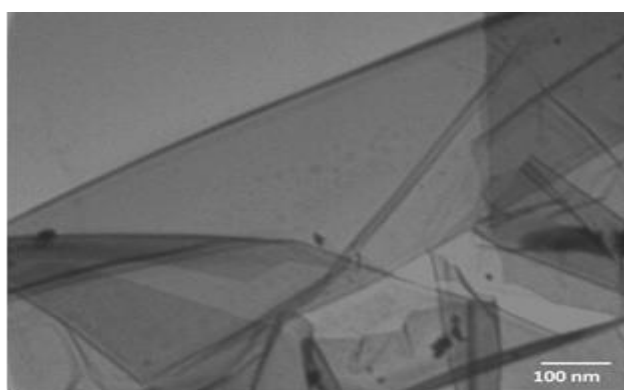


Figure 2 TEM image of synthesized rGO showing sheet-like morphology.

groups, respectively [24]. During the reduction reaction, the hydroxyl, carbonyl and epoxy groups in GO were effectively reduced by D-galactose. In the XPS of rGO, only the peak due to the C–C bond at 284.8 eV is preserved and all the intensities of other peaks related to the bonding between the carbon and the oxygen such as hydroxyl, epoxy and carbonyl are relatively decreased, strongly suggests the removal of the oxygenated functional groups [23].

Raman spectroscopy has been a major experimental technique to study the bonding nature of various carbon materials. In order to further characterize the reduction reaction and to study the nature of sp^2 domains, Raman analyses were performed on the reduced GO and compared with GO as shown in Fig. 4(a) and 4(b). The Raman spectra of graphite show a strong G peak at 1570 cm^{-1} due to the first order scattering of E_{2g} mode [25]. The Raman spectra of graphene oxide show that the G peak is shifted towards 1595.89 cm^{-1} due to the oxygenation of graphite [26]. In addition to this, a broadened D peak at 1350 cm^{-1} also appeared due to the reduction in size of *in plane* sp^2 domains in graphite induced by the creation of defects, vacancies and distortions of the sp^2 domains after complete oxidation [27].

After reduction of graphene oxide, the G peak is shifted towards lower wave number (1591.41

cm^{-1}) compared to that of GO, which agrees with the previous reports [28]. This shift was attributed to the recovery of hexagonal network of carbon atoms with defects. The D peak intensity is increased in rGO compared to that of GO suggesting that the reduction process modified the structure of GO with defects [29]. However, the decrease in FWHM of the D peak in rGO is due to the increase in average size of the sp^2 clusters [30]. The $I(\text{D})/I(\text{G})$ ratio are used to evaluate the average size of the sp^2 cluster in the graphene materials. The corresponding $I(\text{D})/I(\text{G})$ ratio of GO and rGO are measured as 0.8 nm and 0.9 nm, respectively. In order to determine the average size of the sp^2 clusters in GO and rGO, we employed the Tuinstra and Koenig relation, which relates the ratio of D and G peak into the crystallite size as follows [31]:

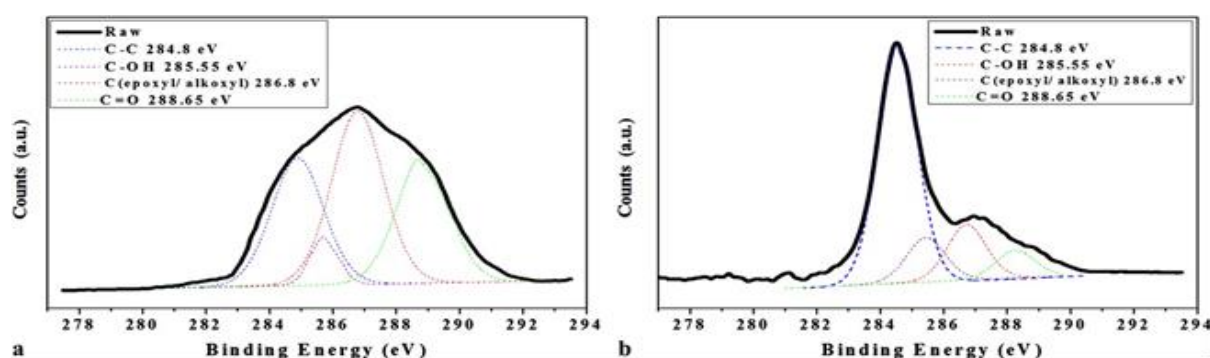


Figure 3 X-ray photoelectron spectra of (a) GO and (b) rGO.

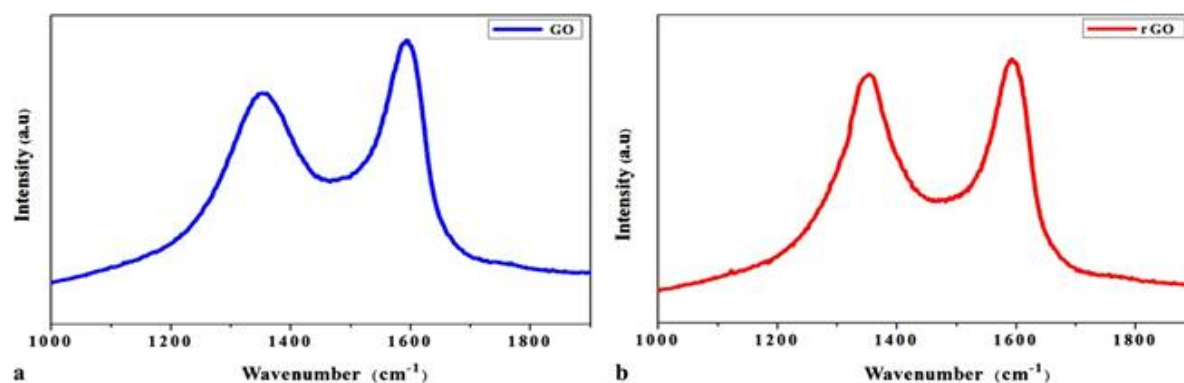


Figure 4 Raman spectra of (a) GO and (b) rGO.

where $I(\text{D})$ is the intensity of the D peak, $I(\text{G})$ is the intensity of the G peak, $C(\lambda)$ is the wavelength dependent prefactor and L_a is the average crystallite size of sp^2 domains. The average sizes of the sp^2 clusters in GO and rGO were found as 5.28 and 4.57 nm, respectively. The decrease in average size of sp^2 clusters is due to the formation of new sp^2 clusters which are smaller in size compared to the ones present in GO before reduction [15, 26].

The thermal stability of the rGO is studied using thermo gravimetric analysis and compared with the GO and the pre-cursor graphite as shown in Fig. 5. The TGA analysis of graphite shows the high thermal stability of graphite even at 1000°C . Since GO is thermally unstable, it starts

losing the mass from 100°C due to the removal of moisture content. The major mass loss occurs at 200°C due to the removal of oxygen-containing functional groups such as CO, CO₂ and H₂O vapors. In case of rGO, already the oxygen-containing functional groups were removed during the reduction process, yielding a better thermal stability than the GO. The TGA of rGO shows the removal of water content at 100°C.

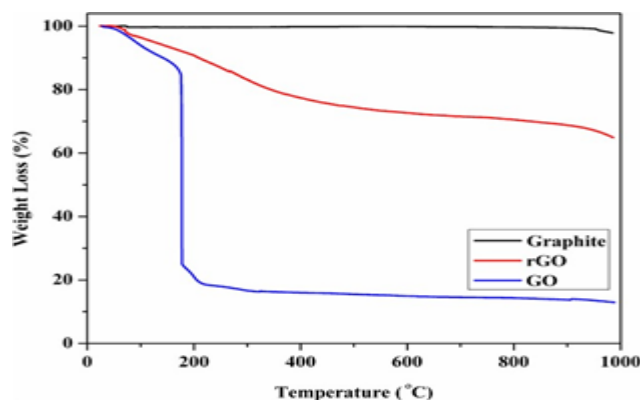


Figure 5 Thermogravimetric analysis of graphite, GO and rGO.

This is well in agreement with the previous report on reduced graphene sheets [26]. All these results suggest that graphene oxide is reduced into graphene sheets by using D- galactose as a reducing agent.

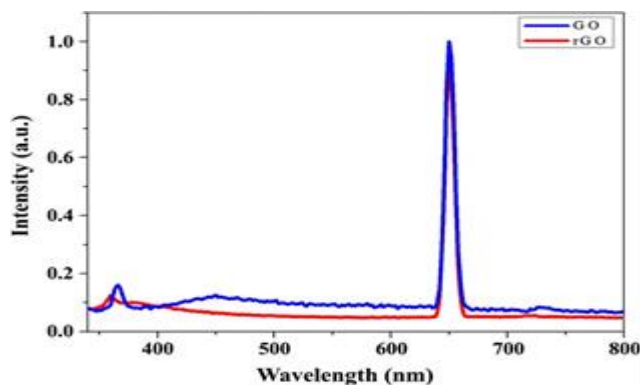


Figure 6 Photoluminescence spectra of GO and rGO.

The study on the optical properties of graphene sheets is an important aspect for its application in photonics [32]. The oxidation of graphite causes the formation of graphitic islands in GO which produces a disruption of the π -network and thus opens up a band gap in the electronic structure [33]. Figure 6 shows the photoluminescence spectra of GO and rGO nanosheets recorded using an excitation wavelength of 325 nm. The PL spectrum of GO shows a sharp emission peak in the near ultraviolet UV region at 365 nm corresponding to the band emission of GO. The unusual strong intensity at 650 nm is not due to the GO sample but due to the overlap of the second-order emissions associated to the excitation wavelength [14]. The UV emission in GO is due to the oxidation of graphite which produce various sizes of crystalline graphitic sp^2 clusters surrounded by amorphous sp^3 matrix in GO which act as a high tunnel

barrier resulting in the creation of band gap in GO. PL response of graphene oxide in the low energy region has been reported earlier recently [34]. The PL spectrum of rGO nanosheets also exhibits a sharp emission at 650 nm due to the overlap of the second-order emissions as similar in GO. This second-order emission was verified by using a range of excitation wave-length (325, 400 and 500 nm). The near band emission is quenched and blue shifted (359 nm) after the reduction process. The intensity of the PL emission of rGO is reduced by half compared to GO after the reduction process shows the quenching in PL emission. Although the mechanism of light emission from rGO still unclear and remains unexplored, the quenching of PL quantum yields is possibly due to the following reason. The quenching of PL in rGO is due to the removal of functional groups which is due to the restoration of more number of sp^2 clusters in the graphene sheet after reduction. The newly formed sp^2 clusters in rGO can provide percolation pathways between sp^2 clusters already present. Thus, the reduction of GO results in formation of zero gap regions in the rGO sheets with some of the functional groups remains still unreduced even after the reduction process. This ensures that the ratio of the zero gap sp^2 clusters is comparatively high enough to the sp^3 clusters in the rGO sheets resulting in quenching of photoluminescence due to weak carrier confinement. This is supported by our XPS spectra [Fig. 3] and Raman spectra [Fig. 4] of the rGO sheets. Hence with our results, we can believe that the photoluminescence in GO and rGO depends on the size or length scale of the graphitic regions (sp^2 domains) and the oxidized regions (sp^3 domains). In this regard, it is much needed to investigate more the levels of oxidized and unoxidized region in both GO and rGO since no straightforward relationship exists.

4 CONCLUSIONS

In conclusion, rGO sheets are synthesized from GO using D- galactose and are characterized using physical and chemical methods. The studies on XPS show the existence of small fractions of oxygenated functional groups in the rGO sheets even after reduction. Raman analysis shows the formation of new sp^2 clusters in rGO sheets. Moreover, the obtained rGO sheets exhibited quenching in PL emission spectra and are blue shifted due to increased sp^2 clusters after reduction.

References

- [1] K.S. Novoselov, A.K. Geim, S.V. Morozov, D. Jiang, M.I. Katsnelson, I.V. Grigorieva, S.V. Dubonos, A.A. Firsov, *Nature* 438 (2005) 197
- [2] S.V. Morozov, K.S. Novoselov, M.I. Katsnelson, F. Schedin, D.C. Elias, J.A. Jaszczak, A.K. Geim, *Phys. Rev. Lett.* 100 (2008) 016602
- [3] V. Gunasekaran, S.-J. Kim, *Curr. Appl. Phys.* 82 (2011) 547
- [4] G. Lu, L.E. Ocola, J. Chen, *Appl. Phys. Lett.* 94 (2009) 083111
- [5] D.R. Lenskia, M.S. Fuhrer, *J. Appl. Phys.* 110 (2011) 013720
- [6] C.H. Lui, K.F. Mak, J. Shan, T.F. Heinz, *Phys. Rev. Lett.* 105 (2010) 127404

- [7] X. Li, X. Wang, L. Zhang, S. Lee, H. Dai, *Science* 319 (2008) 1229
- [8] S. Park, R.S. Ruoff, *Nat. Nanotechnol.* 4 (2009) 217
- [9] M.Y. Han, B. Ozyilmaz, Y. Zhang, P. Kim, *Phys. Rev. Lett.* 98 (2007) 206805
- [10] T. Gokus, R.R. Nair, A. Bonetti, M. Bohmler, A. Lombardo, K.S. Novoselov, A.K. Geim, A.C. Ferrari, A. Hartschuh, *ACS Nano* 3 (2009) 3963
- [11] G. Eda, Y.Y. Lin, C. Mattevi, H. Yamaguchi, H.A. Chen, I.-S. Chen, C.-W. Chen, M. Chhowalla, *Adv. Mater.* 22 (2010) 505
- [12] H.K. Jeong, M.H. Jin, K.P. So, S.C. Lim, Y.H. Lee, *J. Phys. D, Appl. Phys.* 42 (2009) 065418
- [13] S. Saxena, T.A. Tyson, E. Negusse, *J. Phys. Chem. Lett.* 1 (2010) 3433
- [14] S. Shukla, S. Saxena, *Appl. Phys. Lett.* 98 (2011) 073104
- [15] C. Zhu, S. Guo, Y. Fang, S. Dong, *ACS Nano* 4 (2010) 2429
- [16] S.Gao, F. Liu, Y. Liu, N. Ma, Z. Wang, X. Zhang, *Chem. Mater.* 22 (2010) 2213
- [17] K. Karthikeyan, R. Mohan, S.-J. Kim, *Appl. Phys. Lett.* 98 (2011) 244101
- [18] K.S. Vasu, B. Chakraborty, S. Sampath, A.K. Sood, *Solid State Commun.* 150 (2010) 1295
- [19] L. Zhang, J. Liang, Y. Huang, Y. Ma, Y. Wang, Y. Chen, *Carbon* 47 (2009) 3365
- [20] Naser Al-Falahy, Omar Y. K. Alani, *Experimental and Theoretical NANOTECHNOLOGY* 3 (2019) 45
- [21] L. Zhang, X. Li, Y. Huang, Y. Ma, X. Wan, Y. Chen, *Carbon* 48 (2010) 2367
- [22] E.C. Salas, Z. Sun, A. Luttge, J.M. Tour, *ACS Nano* 4 (2010) 4852
- [23] J. Zhang, H. Yang, G. Shen, P. Cheng, J. Zhang, S. Guo, *Chem. Commun.* 46 (2010) 1112
- [24] A. Lerf, H. He, M. Forster, J. Klinowski, *J. Phys. Chem. B* 102 (1998) 4477
- [25] G. Eda, M. Chhowalla, *Adv. Mater.* 22 (2010) 2392
- [26] S. Stankovich, D.A. Dikin, R.D. Piner, K.A. Kohlhaas, A. Kleinhammes, Y. Jia, Y. Wu, S.T. Nguyen, R.S. Ruoff, *Carbon* 45 (2007) 1558
- [27] M. Baraket, S.G. Walton, Z. Wei, E.H. Lock, J.T. Robinson, P. Sheehan, *Carbon* 48 (2010) 3382
- [28] V.C. Tung, M.J. Allen, Y. Yang, R.B. Kaner, *Nat. Nanotechnol.* 4 (2009) 25
- [29] I.K. Moon, J. Lee, R.S. Ruoff, H. Lee, *Nat. Commun.* 1 (2010) 1
- [30] C. Mattevi, G. Eda, S. Agnoli, S. Miller, K.A. Mkhoyan, O. Celik, D. Mastrogiovanni, G. Granozzi, E. Garfunkel, M. Chhowalla, *Adv. Funct. Mater.* 19 (2009) 1
- [31] F. Tuinstra, J.L. Koenig, *J. Chem. Phys.* 53 (1970) 1126
- [32] K.N. Kudin, B. Ozbas, H.C. Schniepp, R.K. Prudhomme, I.A. Aksay, *R. Car, Nano Lett.* 8 (2007) 36
- [33] F. Bonaccorso, Z. Sun, T. Hasan, A.C. Ferrari, *Nat. Photonics* 4 (2010) 611
- [34] Z. Luo, P.M. Vora, E.J. Mele, A.T.C. Johnson, J.M. Kikkawa, *Appl. Phys. Lett.* 94 (2009) 111909



Preparation, analysis and characterization of ITO nanostructures

C. Deke*, E. P. Petrik

Supramolecular and Nanostructured Materials Research Group of the Hungarian Academy of Sciences, University of Szeged, Aradi vértanúk tere 1, 6720 Szeged, Hungary

*) Email: c.deke@chem.u-szeged.hu

Received: 1/1/2020 / Accepted: 10/5/2020 / Published: 1/9/2020

Conductive and highly transparent indium tin oxide (ITO) thin films were prepared on photosensitive glass substrates by the combination of sol-gel and spin-coating techniques. First, the substrates were coated with amorphous Sn-doped indium hydroxide, and these amorphous films were then calcined at 550°C to produce crystalline and electrically conductive ITO layers. The resulting thin films were characterized by means of scanning electron microscopy, UV-Vis spectroscopy, X-ray photoelectron spectroscopy and spectroscopic ellipsometry. The measurements revealed that the ITO films were composed of spherical crystallites around 20 nm in size with mainly cubic crystal structure. The ITO films acted as antireflection coatings increasing the transparency of the coated substrates compared to that of the bare supports. The developed ITO films with a thickness of 170–330 nm was highly transparent in the visible spectrum with sheet resistances of 4.0–13.7 k Ω /sq. By coating photosensitive glass with ITO films, our results open up new perspectives in micro- and nanotechnology, for example in fabricating conductive and highly transparent 3D microreactors.

Keywords: Analysis; Characterization; ITO; Nanostructure.

1. INTRODUCTION

By virtue of its excellent optical and electrical properties, indium tin oxide (ITO) is one of the most extensively studied transparent conductive oxides [1]. ITO thin films with high transmittance in the visible spectral range and with low resistivity have previously been prepared by several methods, such as sputtering [2], spray pyrolysis [3], chemical vapor deposition [4], electron-beam evaporation [5], screen printing [6], pulsed-laser deposition [7],

and the sol–gel process [8]. The sol–gel method is a popular technique to produce high-quality thin films as it has a number of advantages, such as relatively low cost, a need for only simple equipment, and a high degree of control over the chemical composition of the resulting metal oxides. Sol–gel-based ITO films can be prepared either by the deposition of coating solutions [9] or from sols containing colloids [10]. In the coating solutions, the precursors are not hydrolyzed before the film deposition step [11]. In this case, after film deposition, the resulting, partially hydrolyzed precursors transform to ITO upon calcination. The coating solutions are frequently used to prepare ITO films, but they contain inorganic ions of the precursors, which could be unfavorable during calcination. Sols (or colloidal dispersions) containing ITO [12] or other types of nanoparticles (e.g. indium tin hydroxide, ITH) can also be used for thin-film preparation [10]. ITH sols are generally synthesized by the hydrolysis of InCl_3 or $\text{In}(\text{NO}_3)_3$ and SnCl_4 in aqueous medium [13]. Since the hydrolysis and condensation of the precursors result in colloidal particles, the undesired ions (Cl^- and NO_3^-) can be removed from the media of the sol by washing or use of dialysis. Another advantage of the sol-based process is that the morphology or crystal phase of the ITO particles can be controlled via the synthesis temperature and pH. Sol–gel-based films are usually prepared on a glass or quartz substrate by dip- or spin-coating techniques. During film deposition, the medium of the sol evaporates and subsequently a metal oxide/hydroxide xerogel film is formed [10]. The as-prepared layers are often amorphous,

and heat treatment at 500–550°C is therefore necessary to obtain crystalline and conductive ITO films. This heat treatment is an important step because it causes particle sintering, which leads to a decrease in the electrical resistance of the ITO layers. For sol preparations, the well-known hydro [14] and solvothermal [15] methods can also be employed. These synthesis methods, with the application of elevated temperature and pressure, can produce ITO nanoparticles directly instead of ITH [16].

In a recent study [10], we presented a short survey of the preparation of ITO films with well-controlled layer thickness (~40–1160 nm) by applying a combination of sol–gel and dip-coating methods. The adhesive ITH sols applied allowed the rapid preparation of high-quality ITO films. It was revealed that the sheet resistance of the ITO films was significantly lower when the ITH sols contained polyvinylpyrrolidone (PVP). In another study [17], we demonstrated a novel concept through which to achieve embedded 3D conductive and completely transparent structures in glass microchips by using a combination of femtosecond laser microfabrication and a sol–gel method. The application of ITO coatings on photosensitive glass can be a breakthrough toward the further exploitation of microchip technology by fabricating microchips with novel features. The idea relies on the wide-ranging applicability and sensitivity of ITO films of value for sensitive biochemical analysis and biological, chemical, and medical inspections based on the development of highly functional microdevices. Photosensitive glass (under the trade name Foturan®) has all of the unique properties of traditional glass (e.g. transparency, hardness, chemical, etc.) and is an excellent material with which to embed hollow microchannels and other complicated 3D structures by using femtosecond laser direct writing [18–20]. Moreover, Foturan glass can withstand thermal treatment at 550°C, which is a requirement for the production of sintered, conductive ITO films.

In the present study, we report on the preparation of sol–gel-based ITO thin films on photosensitive glass from PVP-containing amorphous ITH sol through use of spin-coating

method and subsequent calcination. The structural, optical and electrical properties of the resulting ITO thin films are reported and the effects of the aging time on the crystallinity and crystal phase composition are discussed.

2. EXPERIMENTAL DETAILS

2.1 Synthesis of ITH sols

1.1727 g of $\text{InCl}_3 \cdot 4\text{H}_2\text{O}$ and 0.1402 g of $\text{SnCl}_4 \cdot 5\text{H}_2\text{O}$ were dissolved in 100 ml of deionized water, and the precursors were hydrolyzed at room temperature by the addition of 2.0 ml of 25% NH_3 solution during intensive stirring. The resulting dispersion was centrifuged and the sediment obtained was washed with water and subsequently with ethanol. After the washing procedure, a stable sol was prepared by redispersion of the sediment in 25 ml of ethanol with the addition of PVP in a final concentration of 0.1 w/v%. This sol was designated ITH-NA. The ITH-A sol was prepared as previously reported [10]. In this synthesis the aqueous dispersion of the as-prepared precipitate was dialyzed against deionized water until the conductivity had decreased below $1 \mu\text{S cm}^{-1}$. The dialysis was continued for a further 3 days, during which the precipitate was aged. After dialysis, the dispersion was centrifuged and the sediment obtained was washed with ethanol. Finally, the resulting precipitate was dispersed in 50 ml of ethanol with the addition of PVP as described above.

2.2 Preparation of ITH and ITO thin films

ITH thin films were prepared on Foturan glass substrates (10 × 10 × 2 mm) by the spin-coating method. 50 μl of ITH-NA or ITH-A sol was dropped onto the substrate rotating with 3000 rpm and the as-prepared layer was subsequently dried for 30 s in the spin-coater. To prepare multi-layer films the above deposition step was applied again with the desired number of repetitions. To obtain ITO thin films, the deposited ITH layers were calcined for 30 min in air at 550°C in a preheated furnace.

2.3 Characterization

Thermogravimetric (TG) investigations were carried out in air with a TGA/SDTA 851e (Mettler Toledo) derivatograph at a heating rate of 5°C min^{-1} . X-ray diffraction (XRD) patterns were collected on a Bruker D8 Advance diffractometer equipped with a Göbel mirror. The measurements were made in θ - θ configuration using $\text{CuK}\alpha$ radiation. The operating voltage and current were 40 kV and 40 mA, respectively. Transmission electron microscopy (TEM) images were obtained with a Philips CM-10 electron microscope at an accelerating voltage of 100 kV. Scanning electron microscopy was performed with a Hitachi S-4700 FE-SEM cold-field emission electron microscope operated at 5 kV. UV-Vis spectrophotometry was performed with an Ocean Optics Chem2000-UV-VIS diode array spectrophotometer at wavelengths in the range 250–800 nm.

The X-ray photoelectron spectroscopy (XPS) was carried out with VG ESCALAB 250 spectrometer (Thermo Fisher Scientific K.K.) using monochromatic Al K X-ray radiation. The X-ray gun was operated at 200 W (15 kV, 13.3 mA). The C 1s binding energy of adventitious carbon was used as energy reference; it was taken at 284.8 eV.

Ellipsometry measures the complex reflection ratio ($\rho \tan(\Psi) e^{i\Delta}$, where Ψ and Δ are the ellipsometric angles), the ratio of the reflection coefficients of light polarized parallel and perpendicular to the plane of incidence [21]. By sensitively measuring phase changes of the light passing through the deposited layers, ellipsometry has a sensitivity of 0.1 nm and 0.0001 in the thickness and the refractive index, respectively. However, as it is an indirect method, the accuracy depends on the choice of an appropriate optical model. The ellipsometric measurements were performed with a Woollam M-2000DI rotating compensator spectroscopic ellipsometer in the wavelength range 400–800 nm, at angles of incidence ranging from 50° to 70°. A microspot was used to avoid backside reflection from the transparent substrate. The refractive index of the bare Foturan substrate was determined by using the multiple-angle spectra with backside roughening.

The sheet resistance of ITO films was determined by four-point probe measurements with a Keithley 2400 source-meter and a cylindrical four-point probe head (Jandel Engineering Ltd). The tip array was linear with a probe spacing of 1.0 mm. The 100-micron radius tips were made of tungsten carbide. The spring load was 60 g per tip. The sheet resistance (R_s) was calculated via the following relationship: $R_s = \pi / \ln 2 \times (V/I)$ where V and I are the voltage and the current, respectively.

3. RESULTS AND DISCUSSION

3.1 Structure, morphology and surface composition

ITO thin films were prepared by a combination of conventional sol-gel and spin-coating techniques. In the first part of the procedure, indium tin hydroxide (ITH) sol was synthesized, while in the second step ITH thin films were prepared by a spin-coating. Finally, the ITH films were calcined at 550°C. To synthesize ITH, the precursors (InCl_3 and SnCl_4) were hydrolyzed in aqueous medium by the addition of NH_3 solution until the pH reached 9. Following the hydrolysis of In^{3+} and Sn^{4+} and the condensation of the resultant hydroxide species, the hydrous gel obtained was subsequently washed with water and ethanol. Before the washing procedure, the precipitate was not left to age which is a significant difference as compared with our previously reported synthesis [10].

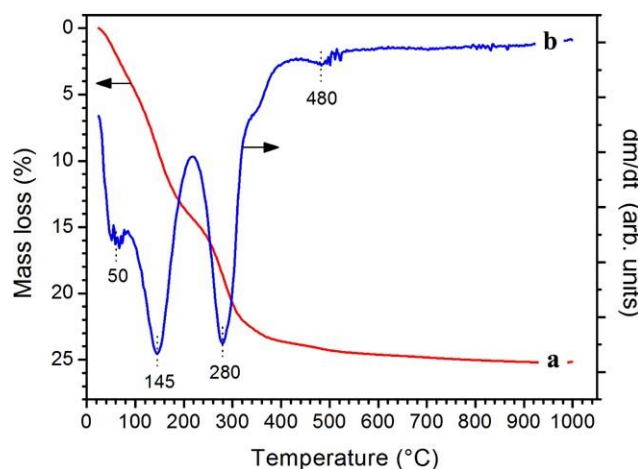


Figure 1 (a) TG and (b) DTG curves of ITO-NA xerogel dried at 50 °C.

As we presented earlier, the electric resistance of ITO films can be decreased by the addition of PVP to the ITH sol [10]. After the washing procedure, therefore the gel was dispersed ultrasonically in ethanol, and PVP was added to the sol in final concentration of 0.1 w/v%. The solid content of the sol was 3.5 w/v%. To obtain ITH xerogel powder, the ethanol was evaporated from the sol at 50°C. The thermogravimetric (TG) curve of the ITH-NA xerogel obtained is presented in Fig. 1, curve a. The total mass loss in the range 25–1000°C was 25.2%. The differential thermogravimetric (DTG) curve (Fig. 1, curve b) exhibited minima at 50, 150, 280, 350 and 480°C. Two main processes can be distinguished; the first (25–215°C) is due to dehydration, while the mass loss above 215°C is assigned to the dehydroxylation of ITH and the decomposition of PVP. In the interval 550–1000°C, the xerogel lost its residual OH groups, which caused only a minor mass loss (0.7%). Since total mass loss of the xerogel without PVP was 19.9%, the PVP content of the ITO-NA xerogel was 5.3%. It should be noted that the total mass loss of the previously synthesized aged ITH xerogel [10] was slightly lower, which may be due to the higher drying temperature (80°C) applied prior to the TG analysis. The XRD patterns of the ITH-NA powder both before and after calcination are displayed in Fig. 2. The XRD pattern of the sample dried at 50°C (Fig. 2, curve a) did not contain any peaks, which indicates that the ITH-NA was amorphous. However, the ITH-A sample was nanocrystalline, as reported previously [10]. In contrast with ITH-NA, the ITH-A xerogels consisted of cubic $\text{In}(\text{OH})_3$ and orthorhombic InOOH crystal phases. It should be noted that the nature of the medium during the aging process is of crucial importance for the crystal phase evolution. When the as-prepared precipitate (hydrous gel) was subsequently washed with ethanol, the ITH did not become crystalline even after several months of storage. We therefore conclude that the aging of the gel in an aqueous medium favors the formation of nanocrystalline ITH.

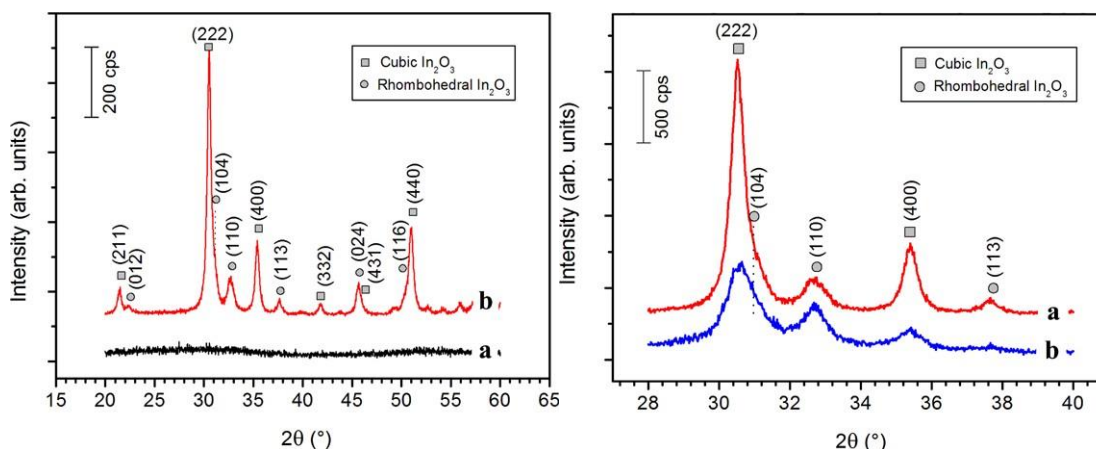


Figure 2 XRD patterns of (a) ITH-NA and (b) ITO-NA powders. The characteristic reflections of In_2O_3 with cubic and rhombohedral structures are indexed.

In the XRD pattern of the calcined ITH-NA at 550°C (hereafter designated ITO-NA), cubic (JCPDS No. 06-0416) and rhombohedral (JCPDS No. 22-0336) In_2O_3 can be identified (Fig. 2, curve b). Other crystal phases (e.g. SnO and SnO_2) could not be detected, indicating a homogeneous distribution of Sn^{4+} in the In_2O_3 host. The broadened XRD lines revealed that the ITO-NA was nanocrystalline. Due to this broadening, several reflections of the two crystal phases overlapped. The predominant crystal phase was cubic; the (104) reflection of the rhombohedral phase appeared only as a shoulder on the wide-angle side of the (222) peak.

To determine the average crystallite size, the broad peak in the range 29–32° was deconvoluted in accordance with the positions of (222) and (104) reflections. From the FWHM of the (222) and (110) reflections, the average sizes (determined via the Scherrer equation) were 19.5 and 11.6 nm for the cubic and rhombohedral crystallites, respectively. From a comparison of the line broadening it is clearly seen that the calcined ITH-A at 550°C (hereafter designated ITO-A) consisted of smaller crystallites than those of ITO-NA. For ITO-A, the sizes were 8.3 and 9.4 nm for the cubic and rhombohedral crystallites, respectively. The XRD patterns also revealed that the ratio of the cubic and rhombohedral phases was influenced by the aging. For ITO-NA, the intensities of the lines relating to the rhombohedral phase were significantly lower. Consequently, the aging of ITH favors the formation of rhombohedral ITO crystallites. However, it should be noted that the phase evolution may also depend on the pH during aging. Kim et al. [22] reported that lower pH (8) promotes the formation of rhombohedral ITO.

TEM picture of the ITH-NA (Fig. 3a,b) indicated an amorphous structure confirming the XRD results. The ITO-NA sample (Fig. 3c) was composed of round particles with a diameter of 8–26 nm. The estimated average particle size was 17 nm, although the precise particle size distribution could not be given because of the sintering, which caused the particles to assemble into large aggregates. The electron diffraction pattern of ITO-NA (inset in Fig. 3c) confirmed the presence of both cubic and rhombohedral phases. As may be seen from the TEM picture of ITO-A (Fig. 3d), the rectangular morphology remained after calcination; the cubes and columns were still present and only a minor coarsening of the round particles could be observed. It is clear from the TEM image of ITO-A that the large rectangular particles were composed of primary particles 5–10 nm in size, in accordance with the value (8.3 nm) calculated via the Scherrer equation.

ITH-NA thin films with different layer numbers were prepared on photosensitive glass from ITH-NA sol by a spin-coating technique. To obtain crystalline and conductive ITO films, the as-deposited ITH layers were calcined at 550°C. No heat treatment was applied between the film deposition steps. The surface morphology of the ITO-NA films obtained is presented in Fig. 4a. The SEM picture revealed that ITO-NA consisted of fine particles with uniform round-shaped morphology, resulting in lower surface roughness as compared with ITO-A. The SEM picture also revealed that the film was significantly porous. The cross-sectional view (Fig. 4b) of ITO-NA film made up of 3 layers showed a uniform thickness of 360 nm.

XPS measurements on the ITO-NA film yielded the high-resolution spectra of In 3d, Sn 3d and O 1s regions depicted in Fig. 5. Both the In 3d and the Sn 3d spectra were symmetric, indicating a single chemical state and the O–In–O

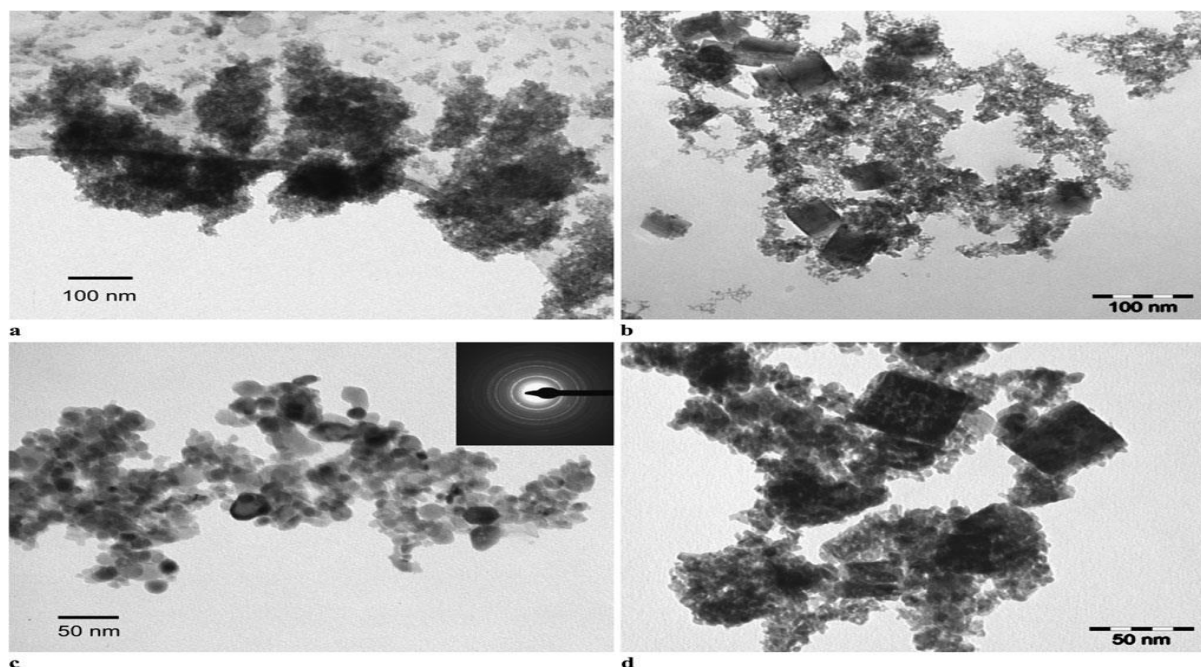


Figure 3 TEM images of (a) ITH-NA, (b) ITH-A, (c) ITO-NA and (d) ITO-A samples. The inset in (c) shows the corresponding electron diffraction pattern.

and O–Sn–O chemical environments. The In $3d_{5/2}$ and Sn $3d_{5/2}$ peaks were located at 444.3 and 486.6 eV, respectively. These binding energies reveal In and Sn oxidation states of 3 and 4, respectively [16, 23]. Table 1 lists the binding energies of In, Sn and O components in various ITO samples prepared by different synthesis methods.

Our XPS results are in good agreement with those reported for ITO films elsewhere [24, 25]. Quantitative analysis using the atomic sensitivity factors (ASF) of In (ASF 4.51) and Sn (ASF 4.89) resulted in an In:Sn atomic ratio of 8.73, a value slightly lower than the estimated theoretical atomic ratio In:Sn 10. While the In $3d$ and Sn $3d$ spectra are symmetrical, reflecting one chemical state, the O $1s$ spectrum has a shoulder on the high binding energy side at 531.6 eV, due to surface OH groups. Similar asymmetric O $1s$ spectra were observed for other OH-containing metal oxides (SnO₂ and TiO₂) [23, 26]. The main component of the O $1s$ spectrum is at 530 eV, which corresponds to the lattice oxygen. The atomic ratio (In Sn):O was found to be 0.664.

3.2 Optical and electrical properties

The UV-Vis transmittance spectra of ITO-NA films are presented in Fig. 6a. It is clearly seen that in the visible wavelength range the uncoated photosensitive glass has a lower transmittance (T) than that of the ITO-NA-coated substrate (Fig. 6a, inset). This phenomenon is due to the ITO layers on the substrate acting as an antireflection coating. After deposition of an ITO-NA monolayer, T increased from 91.6 to 95% throughout the whole visible wavelength range. In the UV range, T decreased slightly with increasing number of layers. The T spectra of the ITO-NA multilayers exhibited interference fringes, and hence the T values depended on the wavelength of the incident light. It should be noted that the ITH-NA layers

also exhibited higher transparency than that of the uncoated substrate. The T values of all ITO-A-coated Foturan glasses also exceeded the T of the uncoated substrate (Fig. 6b, inset). For ITO-A films, the transparency increased with increasing layer number in the whole UV-Vis range. The highest T was 96% after three deposited ITO-A layers.

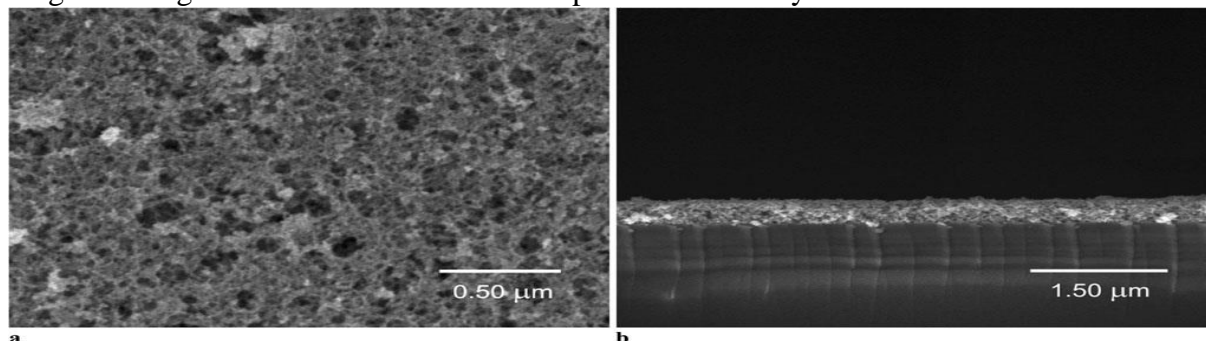


Figure 4 SEM images of (a) surface morphology and (b) cross-sectional view of ITO-NA thin film made up of 3 layers on Foturan glass.

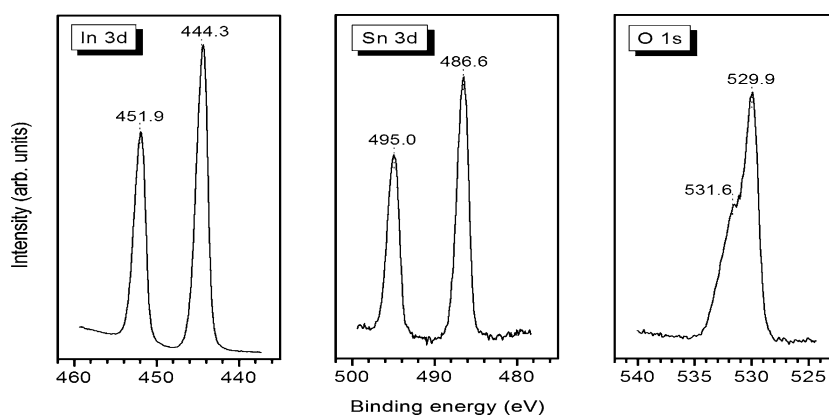


Figure 5 High-resolution XP spectra of In 3d , Sn 3d and O 1s regions for ITO-NA thin film Calcined at 550 °

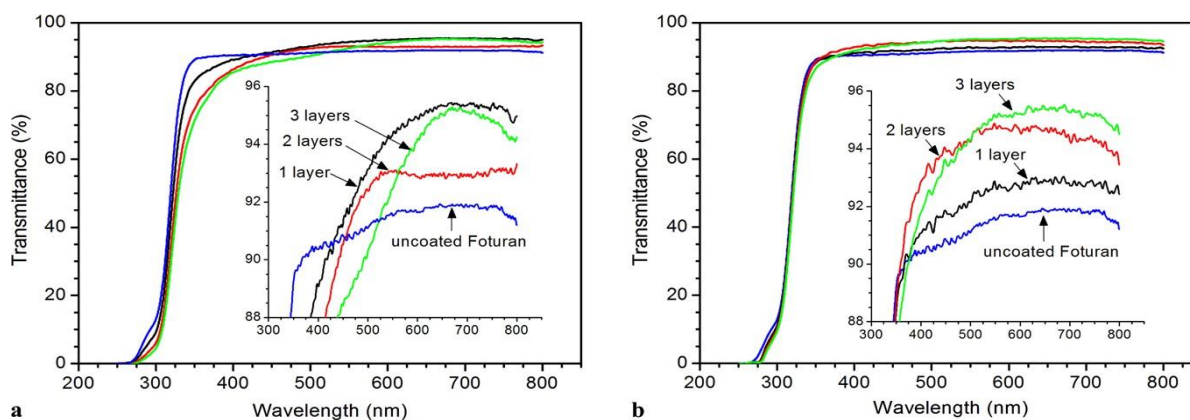


Figure 6 UV-Vis transmittance spectra of (a) ITO-NA and (b) ITO-A thin films composed of different numbers of layers on Foturan glass.

For the ellipsometric measurements, the wavelength range of high T (400–800 nm, see Fig. 6) was used because this allows application of a simple polynomial dispersion function for the refractive index [27] (in a broader range, complex oscillator models must be used [28]). The spectra could be fitted by using a linearly graded depth profile of the refractive index in the range 3–8% (graded models have also been described for RF sputtered ITO films [27]). Figure 8 shows the better fit with the graded model relative to non-graded one. We note that the application of a surface nano-roughness model did not improve the fit, which indicates that the thin films were of high surface quality, in agreement with the above SEM results. For the ITO-A samples, the thickness varied from 26 to 72 nm. The lower film thickness of ITO-A is due to the lower concentration of the ITH-A sol. The refractive indices at the He–Ne laser wavelength of 633 nm were in the range 1.3–1.4 and 1.1–1.3 for the ITO-NA and ITO-A samples, respectively. This is lower than the published values for evaporated and sputtered ITO films (in the range 1.7–2.0 [28, 29]), which is in agreement with the porous structure revealed by SEM (Fig. 3).

The measured sheet resistance (R_s) of ITO-NA films decreased significantly with increasing layer number. For film thickness of 166, 254 and 328 nm, R_s was 13.72 ± 0.04, 5.96 ± 0.05 and 4.02 ± 0.02 k Ω /sq, respectively, i.e. lower than the values measured earlier [10] for ITO-A at similar layer thickness. The differences may be due to the lower surface roughness and better particle-to-particle contacts in ITO-NA films.

4. CONCLUSIONS

ITO thin films were successfully prepared on photosensitive glass substrates by the combination of sol–gel and spin-coating techniques. For film deposition, an amorphous ITH sol in ethanol medium was used. Whereas the as-deposited films were amorphous, nanocrystalline ITO was formed after calcination at 550°C. These ITO nanoparticles displayed spherical morphology and high crystallinity. It was established that the aging process in aqueous medium promotes the crystallization of ITH and favors the formation of large (40–70 nm) particles with rectangular morphology. Without the application of aging, a lower surface roughness is achieved and the resulting ITO film on photosensitive glass acts as an antireflection coating. After deposition of an ITO monolayer, the transmittance in the visible wavelength range increased from 91.6 to 95%. As the thickness increased from 166 to 328 nm, the sheet resistance decreased from 13.7 to 4.0 k Ω /sq.

We believe that the developed ITO films, especially their successful processing on photosensitive glass, can find applications in diverse areas of micro- and nano-technology, such as the development of conductive and highly transparent 3D structures for microreactor applications.

References

- [1] C.G. Granqvist, A. Hultåker, *Thin Solid Films* 411 (2002) 1
- [2] C. Guillén, J. Herrero, *J. Appl. Phys.* 101 (2007) 073514
- [3] T. Ogi, F. Iskandar, Y. Itoh, K. Okuyama, *J. Nanopart. Res.* 8 (2006) 343
- [4] K. Maki, N. Komiya, A. Suzuki, *Thin Solid Films* 445 (2003) 224
- [5] Anissa A. Putri, S. Kato, N. Kishi, T. Soga, *Experimental and Theoretical NANOTECHNOLOGY* 3 (2019) 61
- [6] H. Mbarek, M. Saadoun, B. Bessais, *Mater. Sci. Eng. C* 26 (2006) 500
- [7] J.H. Kim, K.A. Jeon, G.H. Kim, S.Y. Lee, *Appl. Surf. Sci.* 252 (2006) 4834

- [8] S.R. Ramanan, *Thin Solid Films* 389 (2001) 207
- [9] A.C. Dippel, T. Schneller, P. Gerber, R. Waser, *Thin Solid Films* 515 (2007) 3797
- [10] L. Ko"rösi, S. Papp, I. Dékány, *Thin Solid Films* 519 (2011) 3113
- [11] Y. Djaoued, V.H. Phong, S. Badilescu, P.V. Ashrit, F.E. Girouard, V.V. Truong, *Thin Solid Films* 293 (1997) 108
- [12] C. Goebbert, R. Nonninger, M.A. Aegerter, H. Schmidt, *Thin Solid Films* 351 (1999) 79
- [13] T. Kanbara, M. Nagasaka, T. Yamamoto, *Chem. Mater.* 2 (1990) 643
- [14] A. Solieman, S. Alamri, M. Aegerter, *J. Nanopart. Res.* 12 (2010) 2381
- [15] E. Hammarberg, A. Prodi-Schwab, C. Feldmann, *Thin Solid Films* 516 (2008) 7437
- [16] J. Ba, D.F. Rohlfiing, A. Feldhoff, T. Brezesinski, I. Djerdj, M. Wark, M. Niederberger, *Chem. Mater.* 18 (2006) 2848
- [17] S. Beke, L. Ko"rösi, K. Sugioka, K. Midorikawa, I. Dékány, *Appl. Phys. A* 102 (2011) 265
- [18] Y. Cheng, K. Sugioka, K. Midorikawa, M. Masuda, K. Toyoda, M. Kawachi, K. Shihoyama, *Opt. Lett.* 28 (2003) 1144
- [19] M. Masuda, K. Sugioka, Y. Cheng, N. Aoki, M. Kawachi, K. Shi-hoyama, K. Toyoda, H. Helvajian, K. Midorikawa, *Appl. Phys. A* 76 (2003) 857
- [20] Y. Cheng, H.L. Tsai, K. Sugioka, K. Midorikawa, *Appl. Phys. A* 85 (2006) 11
- [21] M. Fried, T. Lohner, P. Petrik, in H.S. Nalwa (ed.) *Handbook of Surfaces and Interfaces of Materials* (Academic Press, San Diego, 2001)
- [22] B.C. Kim, J.Y. Kim, D.D. Lee, J.O. Lim, J.S. Huh, *Sens. Actuator B* 89 (2003) 180
- [23] L. Ko"rösi, S. Papp, S. Beke, A. Oszkó, I. Dékány, *Microporous Mesoporous Mater.* 134 (2010) 79
- [24] M.K. Jeon, M. Kang, *Mater. Lett.* 62 (2008) 676
- [25] X.S. Peng, G.W. Meng, X.F. Wang, Y.W. Wang, J. Zhang, X. Liu, L.D. Zhang, *Chem. Mater.* 14 (2002) 4490
- [26] L. Ko"rösi, A. Oszkó, G. Galbács, A. Richardt, V. Zöllmer, Dékány, *Appl. Catal. B* 77 (2007) 175
- [27] R.A. Synowicki, *Thin Solid Films* 394 (1998) 313
- [28] M. Losurdo, M. Giangregorio P. Capezzuto, G. Bruno, R. De Rosa, F. Roca, C. Summonte, J. Pla, R. Rizzoli, *J. Vac. Sci. Technol. A* 20 (2002) 37
- [29] J.A. Dobrowolski, L. Li, J.N. Hilfiker, *Appl. Opt.* 38 (1999) 489

Analysis and characterization of ZnO nanowires for sensing applications

*T. Philip, J. Maruc, K. Claire**

The University of Alabama, 101 Houser Hall, Tuscaloosa, AL 35487, USA
e-mail: kclaire@crimson.ua.edu

Received: 1/12/2019 / Accepted: 1/6/2020 / Published: 1/9/2020

In this work, we synthesize hierarchical ZnO nanowires in a customized atmospheric CVD furnace and investigate their surface modification behavior for prospective nitroaromatic sensing applications. The morphology and crystal structure of pristine nanowires are characterized through FE-SEM, TEM, X-ray diffraction and EDAX studies. Photoluminescence behavior of pristine nanowires is also reported. Surface modification behavior of synthesized nanowires on a ZnO–oleic acid system is studied by utilizing Raman and FT-IR spectroscopy. Based on these findings, 1-pyrenebutyric acid (PBA) has been identified as an appropriate fluorescent receptor for sensing *p*-nitrophenol. Fluorescence quenching experiments on a PBA–*p*-nitrophenol system are reported and a detection limit of up to 28 ppb is envisaged for PBA-grafted ZnO nanowire-based optical sensor.

Keywords: ZnO; Characterization; Sensing.

1. INTRODUCTION

Recently, one-dimensional (1D) mesoscopic systems such as nanowires, nanotubes and nanorods have attracted a great deal of attention due to their numerous potential applications in nanoscale electronics, optoelectronic devices, and sensor development [1–3]. ZnO, a relatively large band-gap (3.37 eV) semiconductor, has been particularly interesting to the research community due to its large exciton binding energy (60 meV), which facilitates room temperature lasing action based on exciton recombination. Due to its excellent optical properties, ZnO has versatile applications in short-wavelength-based optoelectronic devices such as Light Emitting Diodes (LEDs), Laser Diodes (LDs), nanocatalysis, photovoltaics, OLED-based displays and chemical gas sensors [4–11]. The aforementioned applications require ZnO nanostructures in different morphologies such as nanowires, nanorods and nanobelts and must be subjected to specific post-synthesis procedures to achieve desired functionality. Various methods for synthesizing ZnO nanostructures include Pulsed Laser Deposition (PLD), Molecular Beam Epitaxy (MBE), Vapor–Liquid–Solid (VLS) growth,

Chemical Vapor Deposition (CVD) and Metal Organic Chemical Vapor Deposition (MOCVD) [12–17]. Furthermore, template-based synthesis methodologies such as electrodeposition and sol–gel have also been investigated [18, 19]. Fortunately, among all the methods outlined above CVD-based synthesis is relatively cheap and scalable, producing high-quality, defect-free ZnO nanowires.

Most of the unique properties that these nanowires exhibit stem from their single crystalline structure with a significantly increased surface-to-volume ratio over bulk crystals. We therefore expect surface-based effects to be crucial for any electronic and optoelectronic devices based on ZnO nanowires. These surface-related effects, therefore, mandate rigorous investigation in order to control and optimize the nanowire characteristics for their efficient integration in optoelectronic and FET-based devices. The technological relevance of surface-modified ZnO nanowires has already been demonstrated in sensing devices, DSSCs (Dye Sensitized Solar Cells) for efficient light harvesting, and other hybrid photovoltaic devices [20–22]. The polar nature of ZnO and its ability to maintain high-symmetry *c*-axis orientation during growth has also facilitated the growth of densely packed nanowire arrays that are promising candidates for non-linear optical devices. Furthermore, at the surface there is some symmetry loss which can be expected to increase the non-linear optical response of these nanowires over that of bulk crystals. Coating these nanowires with additional organic or inorganic compounds should, therefore, allow the surface to be tailored to its non-linear signal, thereby enabling the design of an efficient nanoscale optical sensor.

Hence, in this paper we (a) demonstrate cost-effective synthesis of high quality ZnO nanowires by Atmospheric Pressure Chemical Vapor Deposition (APCVD), (b) present evidence for organometallic modification of ZnO nanowire surface by oleic acid, and (c) identify the appropriate fluorophore (1-pyrenebutyric acid) and its potential application for fabricating highly sensitive nitroaromatic sensor when grafted onto a ZnO nanowire surface.

2. EXPERIMENTAL DETAILS

2.1 Growth methodology

ZnO nanowires were synthesized utilizing the template-based CVD method reported by Lee and co-workers [23]. Briefly, Si (100) substrates (MTI corp.) were ultrasonically cleaned in acetone for 10 minutes, followed by IPA and DI water for the same amount of time. Subsequently, the substrates were N₂ blow-dried and placed in an E-Beam evaporator. A 4-nm gold coating was deposited onto the cleaned substrates to serve as a template for facilitating VLS growth. Equal amounts of ZnO powder (99.9 %, J.T. Baker) and graphite powder (99 %, 300 mesh, Alfa Aesar) were milled and the mixture was introduced in a customized CVD furnace. The powder mixture serves as a source for precursor vapors that react to form ZnO nanowires at 950 °C by VLS mechanism. Mixed gas (Ar 2 % O₂) was used as a carrier medium to bring the precursor vapors onto the substrate, placed 3 cm away downstream along the furnace. After 30 minutes of growth time a gray coating was observed on the substrate, which was further characterized through the techniques outlined in the next section.

2.2 Surface modification

For surface modification, pristine ZnO nanowire grown substrates were dipped in oleic acid (1 % v/v) solution prepared in hexane for 10 minutes. Subsequently, the specimens were copiously rinsed in pure solvent for 5 minutes to remove any non-covalently bonded residual oleic acid.

The morphological and compositional characterization of the synthesized ZnO nanowires was performed using Field Emission-Scanning Electron Microscopy (FE-SEM, JEOL 7000) and EDAX analysis (Oxford Instruments). For analyzing the crystal structure, Transmission Electron Microscopy (TEM, FEI-Tecnai) equipped with LaB₆ source operated at 200 kV and X-ray Diffraction (XRD) (Bruker AXS) were used. Surface modification of the pristine nanowires was probed using vibrational spectroscopic techniques such as Raman (Jobin Yvon HR800 UV) and Fourier Transform-Infra Red (FT-IR, Bruker Vertex-70) spectroscopy. Raman analysis was conducted with a 633-nm He–Ne laser, while for FT-IR measurements an IR transparent crystal was employed. Fluorescence measurements were obtained on FluoroMax-3, Jobin Yvon, with a standard 1-cm quartz cuvette.

3. RESULTS AND DISCUSSION

The FE-SEM images of the ZnO nanowires in Fig. 1(a) and (b) confirm that the synthesized nanowire ensembles have random orientations and lack vertical alignment with the Si substrate. This can be attributed to the relatively large lattice mismatch (ca. 40 %) between Si (100) and ZnO. Furthermore, Fig. 1(b) clearly indicates that the synthesized nanowires have a smooth and clean surface with a high aspect ratio, although a small amount of lateral hierarchical growth towards the base of the nanowires is evident. Zhang and co-workers empirically determined that such effects are present due to a high supersaturation of Zn vapor in the furnace or due to the depletion of catalyst from growth fronts [24]. The latter effect is expected to be dominant in our case, as confirmed by the absence of gold catalyst nanoparticles from the nanowire tip. EDAX analysis of the pristine nanowires, as presented in Fig. 1(c), shows that no contaminant phase is present in the synthesized wires. The atomic percentages of Zn and O were found to be in agreement with the stoichiometric ratio of the molecule indicating ZnO as the only constituent of the nanowires.

The orientational preference of the ZnO nanowire during growth was probed with XRD. Figure 2 shows the X-ray diffractogram of the synthesized nanowires. It was observed that the nanowires were preferentially oriented along the [101] direction with a significant proportion grown along the [002] direction. Furthermore, the crystal structure was determined using TEM to characterize a single nanowire. Figure 3(a) shows a typical low-magnification image of a ZnO nanowire that is fully consistent with FE-SEM investigations. The selected area electron diffraction pattern (SAED) of the corresponding nanowire in the inset of Fig. 2(a) confirms very high crystallinity (single-crystal nature) of the

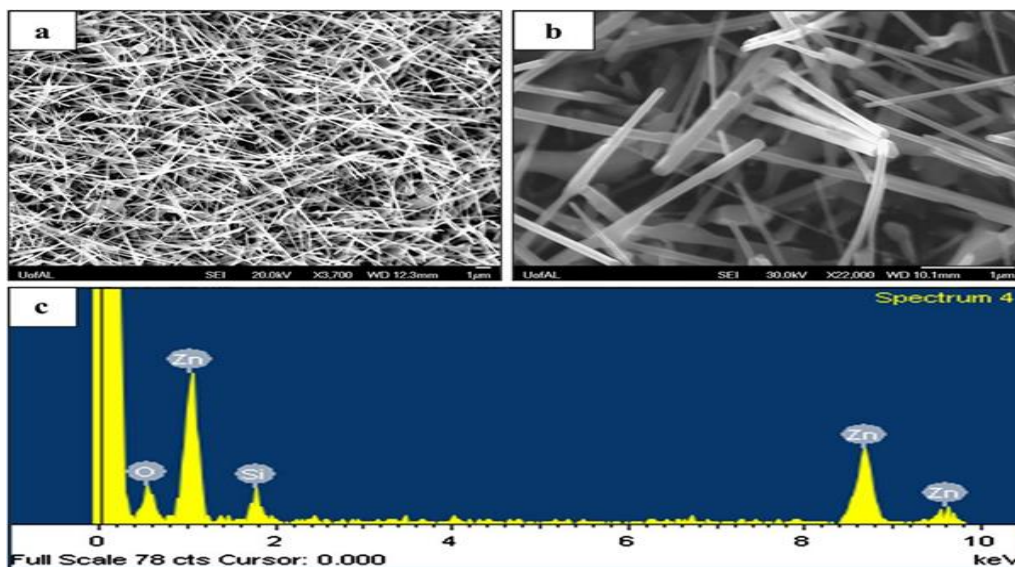


Figure 1 (a), (b) FE-SEM micrographs of as-synthesized ZnO nanowires, (c) EDAX spectrum of as-synthesized ZnO nanowires.

synthesized nanowires. In addition, Fig. 2(b) presents the HR-TEM (High-Resolution TEM) image of the as-grown nanowire, which conforms to the empirical observations of a preferential *c*-axis growth direction of ZnO nanowires via VLS process and typical inter-planar spacing of 0.52 nm.

As mentioned before, the binding of oleic acid was carried out as a proof-of-concept experiment for the functionalization of ZnO nanowires with a bifunctional fluorescence receptor, which can be covalently linked onto a ZnO nanowire surface while concomitantly maintaining its fluorescence characteristics. Since a carboxylic acid ($-\text{COOH}$) moiety is known to form covalent linkages onto metal oxides [25], it is pertinent to investigate the effect of a long chain carboxylic acid ($-\text{COOH}$) compound on our as-synthesized ZnO nanowires. Oleic acid was appropriate choice for this investigation due to its excellent surfactant properties as well as the potential for it to be reversibly replaced by pyrenebutyric acid (PBA) in a metal oxide nanoparticle solution [26]. The justification of utilizing PBA as an appropriate receptor on ZnO nanowire for nitroaromatic sensing is presented later in the paper. Consequently, Raman and FT-IR studies were conducted on modified- and unmodified ZnO nanowires to determine the surface structure information and nature of binding of oleic acid.

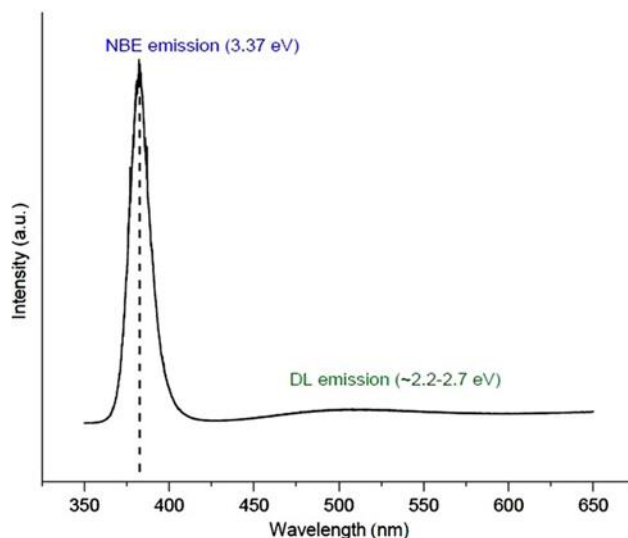


Figure 2 PL spectrum of as-synthesized ZnO nanowires showing band-edge emission.

In Fig. 3, curve A is the FT-IR spectrum of pure oleic acid, which serves as a control to identify peak changes post-modification. The broad peaks at 937 and 1464 cm^{-1} are attributed to out-of-plane and in-plane OH deformations, respectively. The peak at 1284 cm^{-1} is assigned to the C–O stretch, while the intense peak at 1710 cm^{-1} is typical of a bound carbonyl (C=O) moiety. The peaks at 2570 and 2673 cm^{-1} are indicative of oleic acid dimeric forms. The group of peaks at 2825 – 2950 cm^{-1} illustrates CH_2 and CH_3 asymmetric and symmetric stretches. The spectrum resulting from the oleic acid modification of pristine ZnO nanowires is depicted in Fig. 3, curve B. Changes in the spectrum occur mostly in features associated with carboxylic acid moiety ($-\text{COOH}$), which is indicative of bound surface carboxylate. The peaks at 2570 and 2673 cm^{-1} are weaker, which rules out presence of an oleic acid dimer. The C=O band at 1710 cm^{-1} , the C–O stretch at 1284 cm^{-1} and the O–H out-of-plane deformation no longer appear in the spectrum. Consequently, new features indicative of bonding via carboxylate moiety appear. Peaks at 1407 and 1589 cm^{-1} are attributed to $-\text{COO}$ symmetric and asymmetric stretching, respectively. The remaining peaks not previously mentioned are characteristic of a long hydrocarbon chain of oleic acid. The region from 1180 to 1350 cm^{-1} contains multiple weak bands that are evidence of fatty acids. The peaks at 1454 and 1465 cm^{-1} are due to CH_3 and CH_2 deformation modes, respectively.

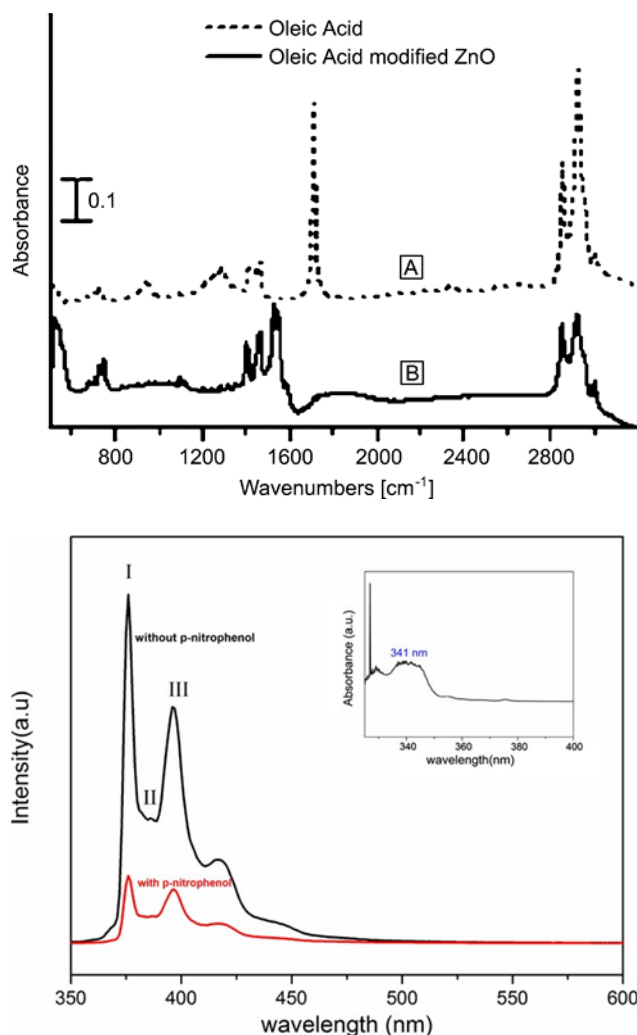


Figure 3 (A) FT-IR spectrum of pure oleic acid, (B) FT-IR spectrum of oleic-acid-modified ZnO nanowires.

All peaks beyond 2800 cm^{-1} , associated with CH_3 , CH_2 and C-C stretching modes, remain in the same positions pre- and post-modification. Based on these observations we investigated an appropriate receptor molecule that can then be grafted onto the ZnO nanowire surface through carboxylate bonding while retaining its optical properties to effectively sense nitroaromatic compounds with high sensitivity. Pyrene-based compounds have been used previously for luminescent oxygen sensing, metal-nanoparticle-based chemo-sensors, bio-electrocatalysis, etc. [27–29]. Furthermore, pyrene derivatives exhibit high quantum yield and strong affinity with analyte, which, coupled with an effective photosensitization process, could potentially be exploited to fabricate highly sensitive optical chemo-sensors. Therefore, we believe that ZnO nanowires are promising candidates that, when functionalized with pyrenebutyric acid (a pyrene derivative), have the ability to effectively sense nitroaromatics with detection limit up to ppb ranges. It was observed that when nitrophenol, the fluorescence of PBA was quenched considerably. Therefore, we firmly believe that a pyrene moiety, post-grafted on the ZnO nanowire surface, will retain its fluorescence characteristics and exhibit similar sensitivity towards nitroaromatics as in the solution phase. The detailed functionalization behavior of PBA on the nanowire surface as well as its mechanism will be the subject of an upcoming manuscript. Based on these preliminary findings, we suggest that ZnO nanowires are a rational choice for fabricating nitroaromatic sensors, if appropriately functionalized with PBA.

Furthermore, forced packing of PBA into films restricts analyte permeability, leading to slow the sensors' response rate.

We envisage that highly sensitive nitroaromatic sensors could be fabricated using PBA functionalized ZnO nanowires, and that fluorescence quenching characteristics such as those of the PBA-*p*-nitrophenol system, can be effectively tuned to sense a wide spectrum of similar analytes.

4. CONCLUSIONS

In this work, ZnO nanowires were synthesized in a customized atmospheric CVD furnace and characterized by FE- SEM, TEM and EDAX. The optical properties of the pristine nanowires were determined by photoluminescence analysis and it was determined that the synthesized nanowires were almost defect-free. Thereafter, surface functionalization studies were conducted with oleic acid, and mode-of- bonding and surface modification characteristics were deduced from Raman and FT-IR analysis. Based on these findings, pyrenebutyric acid (PBA) was identified as a receptor that could be grafted onto the ZnO nanowire surface and subsequently utilized to sense *p*-nitrophenol and other similar nitroaromatic compounds. A detection limit of 28 ppb was shown to be achievable on the ZnO-PBA-*p*- nitrophenol system through photosensitization and fluorescence quenching studies.

References

- [1] D.H. Cobden, Nature 409 (2001) 32
- [2] Y. Cui, C.M. Lieber, Science 291 (2001) 32
- [3] M. Gharaibeh, A. Obeidat, W. Al Awawdeh, A. Rousan, Experimental and Theoretical NANOTECHNOLOGY 3 (2019) 97
- [4] E. Comini, G. Faglia, G. Sberveglieri, Z. Pan, Z.L. Wang, Appl. Phys. Lett. 81 (2002) 1869
- [5] Q. Wan, K. Yu, T.H. Wan, C.L. Lin, Appl. Phys. Lett. 83 (2003) 2253
- [6] B.Y. Oh, M.C. Jeong, T.H. Moon, W. Lee, J.M. Myoung, J.Y. Hwang, D.S. Seo, J. Appl. Phys. 99 (2006) 124505
- [7] K. Nomura, H. Ohta, K. Ueda, T. Kamiya, M. Hirano, H. Hosono, Science 300 (2003) 1269
- [8] T. Yoshida, H. Minoura, Adv. Mater. 12 (2000) 1219
- [9] K. Önenkamp, R.C. Word, C. Schlegel, Appl. Phys. Lett. 85 (2004) 6004
- [10] H. Nanto, T. Minami, S. Takata, J. Appl. Phys. 60 (1986) 482
- [11] M.H. Sarvari, H. Sharghi, Tetrahedron 61 (2005) 10903
- [12] C.H. Bae, S.M. Park, S.C. Park, J.S. Ha, Nanotechnology 17 (2006) 381
- [13] J. Grabowska, K.K. Nanda, E. McGlynn, J.P. Mosnier, M.O. Henry, Surf. Coat. Technol. 200 (2005) 10
- [14] Y.W. Hoe, V. Varadarajan, M. Kaufman, K. Kim, D.P. Norton, F. Ren, P.H. Fleming, Appl. Phys. Lett. 81 (2002) 3046
- [15] M.H. Huang, Y.Y. Wu, H. Feick, N. Tran, E. Weber, P.D. Yang, Adv. Mater. 13 (2001) 113
- [16] J.B. Yi, H. Pan, J.Y. Lin, J. Ding, Y.P. Feng, S. Thongmee, T. Liu, H. Gong, L. Wang, Adv. Mater. 20 (2008) 1170
- [17] W.I. Park, Y.H. Jun, S.W. Jung, G.C. Yi, Appl. Phys. Lett. 82 (2003) 964
- [18] J.J. Wu, S.C. Liu, J. Phys. Chem. B 106 (2002) 9546
- [19] S. Öztürk, N. Tasaltin, N. Kilinc, Z.Z. Öztürk, J. Optoelectron. Biomed. Mater. 1 (2009) 15

- [20] M. Law, L.E. Greene, J.C. Johnson, R. Saykally, P.D. Yang, *Nature* 4 (2005) 455
- [21] D.C. Olson, Y.J. Lee, M.S. White, N. Kopidakis, S.E. Shaheen, D.S. Ginley, J.A. Voigt, J.W.P. Hsu, *J. Phys. Chem. C* 111 (2007) 16640
- [22] P. Ravirajan, A.M. Peiro, M.K. Nazeeruddin, M. Graetzel, D.D.C. Bradley, J.R. Durrant, J. Nelson, *J. Phys. Chem. B* 110 (2006) 7635
- [23] C.Y. Lee, T.Y. Tseng, S.Y. Li, P. Lin, *Tamkang J. Sci. Eng.* 6 (2003) 127
- [24] Z. Zhang, S.J. Wang, T. Yu, T. Wu, *J. Phys. Chem. C* 111 (2007) 47
- [25] Y. Zhang, E. Galoppini, *ChemSusChem* 3 (2010) 410
- [26] N.J. Turro, P.H. Lakshminarasimhan, S. Jockusch, S.P. O'Brien, S.G. Grancharov, F.X. Redl, *Nano Lett.* 2 (2002) 4
- [27] T. Ishiji, M. Kaneko, *Analyst* 120 (1995) 1633
- [28] W. Chen, N.B. Zuckerman, J.P. Konopelski, S. Chen, *Anal. Chem.* 82 (2010) 2
- [29] M.J. Niedziolka, A. Kaminska, M. Opallo, *Electrochim. Acta* 55 (2010) 8744

Morphology of electrospun PVA nanofibers enhanced with graphene oxide, poly (3,4-ethylenedioxythiophene): Polystyrene sulfonate (PEDOT:PSS) and multiwalled carbon nanotubes

Zayd Ahmad Shahizam¹, Abdel Mohsen Benoudjit¹, Nurnazihah Mohamad¹, Firdaus Abd-Wahab¹, Wan Wardatul Amani Wan Salim^{1,*}

¹Department of Biotechnology Engineering, Kulliyah of Engineering, International Islamic University Malaysia (IIUM), 50728 Gombak, Kuala Lumpur, Malaysia

*E-mail: asalim@iium.edu.my

Received: 17/10/2019 / Accepted: 8/7/2020 / Published: 1/9/2020

Morphology of poly(vinyl alcohol) (PVA) nanofibers was studied while varying needle-collector distance and concentrations of graphene oxide, poly (3,4-ethylenedioxythiophene):polystyrene sulfonate (PEDOT:PSS), and functionalized multiwalled carbon nanotubes. Most notably, we found that variations in PVA nanofiber diameter of ~ 34 nm exist in the radial area of electrospinning; the variation is believed to be the result of a fringing electric field effect at the edge of the collector plates. Needle-collector distance was varied between 10 and 17 cm, and FESEM images revealed average fiber diameter decreased from 173 nm to 144 nm with no obvious change in morphology at both nanofiber diameters. Similarly, electrospinning of PVA-GO solution at 17 cm resulted in nanofibers with decreased average diameter of 197 nm ($\sigma = 97$ nm), compared with PVA alone (349 nm, $\sigma = 87$ nm) with no obvious change in morphology. The average diameter of PVA nanofibers then increased with added PEDOT:PSS to 244 nm, $\sigma = 75$ nm. PVA-MWCNT samples at 2 wt% and 4 wt% showed no beading, while at 6, 8, and 10 wt%, beads were prevalent in the fibers. The presence of beads could be the result of re-agglomeration of MWCNTs in the electrospinning solution at higher wt%. No clear trend was found with increasing concentrations of MWCNTs, with average nanofiber diameters varying in the range of 115 – 206 nm.

Keywords Electrospinning; Morphology; PVA; graphene oxide; MWCNTs.

1. INTRODUCTION

Nanofibers have been utilized in various fields such as tissue engineering [1], electronics [2,3], pressure sensors [4], clothing [5,6], and medicine [7]. The attractive properties of nanofibers, including the high surface area-to-volume ratio and ability to be doped with other materials

that enhance its physical and electrical properties, warrant suitability for the aforementioned applications.

Electrospinning is a simple and inexpensive method for producing nanofibers. The method comprises oppositely charged syringe needle tip and collector surface (which alternatively can be grounded). Through the applied potential at the needle tip, a charged polymer solution in the form of a jet is drawn from the needle to the collector to produce nanofibers with diameters of 50 nm to 1 μm [8]. The process of electrospinning occurs in three stages: jet initiation, into a straight or stable jet, followed by instability mode or spinning of jet mode, and finally collector mode, where nanofibers are deposited at the collector. Although the process is straightforward, successfully obtaining uniform and homogeneous nanofiber morphology requires careful tuning of electrospinning parameters, such as needle tip diameter, applied voltage, solvent use, and physical and chemical properties of the polymer solution. These electrospinning parameters determine the morphology of the resultant nanofibers [8] [Add Ref].

Poly(vinyl) alcohol (PVA) is a synthetic water-soluble polymer that is often used in electrospinning, owing to its suitability for the electrospinning process and its low cost. Electrospun PVA nanofibers have been shown to be an attractive material for wound-healing applications, as embedding silver nanoparticles in the nanofibers induces antimicrobial properties [9]. Physical properties of electrospun PVA nanofibers can also be manipulated by altering the basic electrospinning setup. Efforts have been made to selectively deposit PVA nanofibers on electrode surfaces [10] in which the electric field was controlled, improving selectivity [11]. More so, modifications have also been made to deposit PVA nanofibers that are aligned, by electrospinning between two parallel collector plates or moving drums, an approach that also decreases nanofiber diameter [12]. These studies demonstrate how the electric field affects the morphology of nanofibers.

Furthermore, addition of materials can augment electrospun nanofibers. Among others, carbon-based nanomaterials such as graphene oxide (GO) [13] and carbon nanotubes added to PVA solutions have been shown to increase the conductivity of PVA nanofibers to $10.7 \times 10^{-6} \text{ S cm}^{-1}$ [14]. Likewise, the conductive polymer poly(3,4-ethylenedioxythiophene):polystyrene sulfonate (PEDOT:PSS) was shown to adjustably enhance the conductivity of electrospun PVA nanofibers to up to $1.7 \times 10^{-5} \text{ S cm}^{-1}$ [15].

Although previous studies primarily focused on characterizing the effect of solution and apparatus parameters on PVA nanofiber morphology [16-18], they did not include the effect of electrode-collector distance when polymers were enhanced with semiconductive carbon-based, or conductive polymer materials. In this study, we varied the needle-to-collector distance of the electrospinning apparatus to determine the effect on electrospun nanofibers in terms of diameter and morphology. We also studied the morphology of PVA-GO, PVA-GO-PEDOT:PSS nanofibers to understand the effect of each semiconductive material. Additionally, we studied the morphology of PVA nanofibers with multi-walled carbon nanotubes (MWCNTs) at varying concentrations. MWCNTs are known to be hydrophobic in comparison to GO and PEDOT:PSS, which can affect solution properties and nanofiber morphology.

The variation in electrical properties as a result of the modifications in our setup is beyond the scope of this study. It is not confirmed whether the electrical properties of these polymers remain the same with electrode distance. As for varying concentrations of MWCNTs on polymer solutions, the effects on electrical properties of electrospun nanofibers enhanced with MWCNTs have been investigated in [19], though not for PVA.

2. EXPERIMENTAL

2.1 Materials and Reagents

Poly (vinyl alcohol) (PVA, MW = 145,000, 98 % hydrolyzed, from Merck & Co, Kenilworth, New Jersey, USA) and poly (3,4-ethylenedioxythiophene):polystyrene sulfonate (PEDOT:PSS, 1.3 wt % dispersion from Sigma-Aldrich, St. Louis, Missouri, USA) were used throughout the experiments. Ultra-highly concentrated single-layer graphene oxide (UHC-GO-60, 6.2 mg/ml), was purchased from Graphene Supermarket, Calverton, New York, USA, and multiwalled carbon nanotubes (MWCNTs) were obtained from the School of Chemical Engineering, University Sains Malaysia (USM) in Penang. Sodium dodecyl sulfate (SDS) was obtained from Bendosen Laboratory Chemicals, Selangor, Malaysia. Distilled water was used throughout the experiment.

2.2 Preparation of PVA, PVA-GO, PVA-GO-PEDOT:PSS Solution

To prepare composite solutions, PVA was first dissolved in distilled water to form a polymer solution, before adding GO and PEDOT:PSS solution. The PVA solution was prepared at a concentration of 25 w/v % with 10 ml distilled water. PVA, PVA-GO, and PVA-GO-PEDOT:PSS solutions were prepared as shown in Table 1. The total volume of solution was fixed at 20 ml. The parameters were chosen to see the effect of PEDOT:PSS and GO on the morphology of PVA nanofibers.

Table 1 Parameters of PVA, PVA-GO, and PVA-GO-PEDOT:PSS solutions

No.	PVA [g]	GO [ml]	PEDOT:PSS [ml]	Distilled water [ml]
1.	2	0	0	18
2.	2	2	0	16
3.	2	2	2	14

2.3 Preparation of PVA-MWCNT Solution

MWCNTs were first functionalized to make them soluble in water [20]. SDS surfactant was used to increase MWCNT solubility and dispersion in water, followed by ultrasonication for 20 minutes at 50 kHz.

Table 2 Parameters of PVA-MWCNT solutions

No.	Mass in 8 ml H ₂ O			MWCNTs mass ratio [wt %]
	PVA [g]	SDS [g]	MWCNTs [g]	
1	0.9	0.072	0	0
2	0.9	0.072	0.018	2
3	0.9	0.072	0.036	4
4	0.9	0.072	0.054	6
5	0.9	0.072	0.072	8
6	0.9	0.072	0.090	10

2.4 Electrospinning Process

Figure 1 shows the electrospinning setup, which consists of a syringe-pump (NE-1010, New Era Pump Systems, New York, USA), a spinneret with a metallic needle, a collector (aluminum plate covered with aluminum foil), and a high-voltage supply (73030 series, Genvolt, United Kingdom). To study the morphology of nanofibers across the metal plate, the metal plate is divided into nine cells, each 2×2 cm, labelled 1 through 9. The needle is manually aligned to point to the middle of the collector plate.

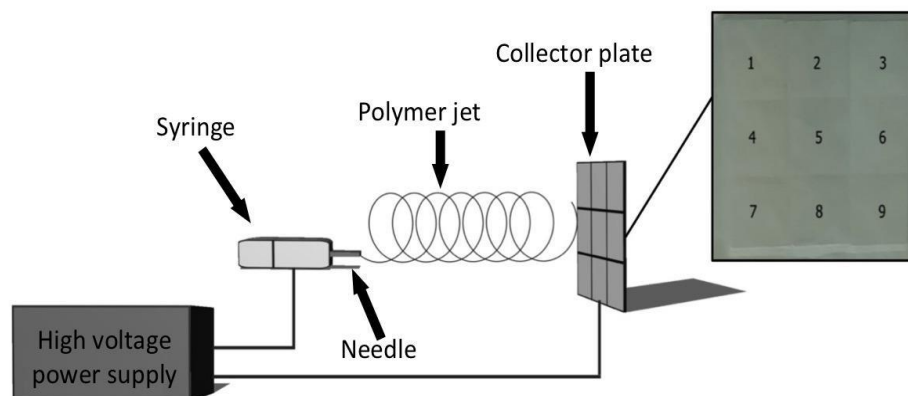


Figure 1 The electrospinning setup consists of a syringe pump, a spinneret with a metallic needle, and a metal plate collector. The collector plate is divided into 9 identical cells (2×2 cm)

To study the effect of the needle-to-collector distance on PVA nanofiber morphology, the distance was varied at 10, 15, and 17 cm, with a pump flow rate of 0.6 ml/h and an inner needle diameter of 0.6 mm (23.5 gauge). For PVA-GO and PVA-PEDOT:PSS, the needle-to-collector distance was 17 cm with a flow rate of 0.7 ml/h and an inner needle diameter of 0.7 mm (22 gauge). The voltage supply was kept constant at 20 kV.

2.5 FESEM Imaging

To achieve full coverage of the collector grid (6×6 cm) with nanofibers that can be mechanically removed from the collector without tearing the nanofiber structure, electrospinning was conducted for 45 minutes. The electrospun PVA samples were removed from the collector; each cell of the grid from 1 to 9 was cut out and observed with a scanning electron microscope (SEM, JSM-1T500HR, JEOL, Japan) available at International Islamic University Malaysia. To observe the morphology of PVA, PVA-GO, PVA-GO-PEDOT:PSS, and PVA-MWCNT nanofibers, each cell was observed with field emission scanning electron microscopy (FESEM, SU 8030, Hitachi) at MIMOS Semiconductor (M) Sdn Bhd, Seri Kembangan, Selangor, Malaysia. The average diameter of electrospun nanofibers was obtained using ImageJ software.

3. RESULTS AND DISCUSSION

3.1 Effect of Needle-to-Collector Distance on the Diameter and Morphology of PVA Nanofibers

Figure 2 shows the SEM images of pristine PVA nanofibers in the central grid cell (cell 5), alongside graphs showing the distribution of the diameters. SEM images, including analysis for the 9 grid cell system used in our study are attached in Appendix A. As can be seen from Figure 2, the PVA nanofibers were smooth with no formation of beads. Although there was no obvious change on the surface morphology of the PVA nanofibers, the increase in needle-collector distance from 10 to 17 cm caused a decrease in the mean diameter of the nanofibers from 173 to 128 nm. We believe this 45 nm reduction in diameter of the nanofibers from electrospinning at 10 to 17 cm to be a result of the additional distance available for the elongation of the nanofiber jet during the instability phase [7, 16, 21]. We found that this reduction in diameter was consistent in all cells of our grid.

The appendix A shows our full results, from which we found further trends. The 9-grid cell system we used reveals reductions (of about ~40 nm) in nanofiber diameter are present further away from the center of electrospinning. Sorting grid cells by order of increasing distance from the center of electrospinning

gives 3 groups: center (cell 5), adjacent (cells 2, 4, 6, 8), and edge (cells 1, 3, 7, 9). Since each grid cell was 2 x 2 cm, these categories were 0, 2, and 2.83 cm away from the electrospinning center, respectively. We found that among the three categories, nanofibers at the center of the collector plate (cell 5) had the highest mean diameter at each needle-collector distance. For comparison, Figure 3 shows SEM images and nanofiber diameter distributions of cell 1, an edge cell. The difference can be seen with Figure 2, which previously showed cell 5, the center cell. The observed diameters were 144, 140, and 94 nm, at cell 1, compared to 173, 144, and 128 nm at cell 5 (center). We suspect the reduction in diameter from the center cell to the edge cells could be explained by the fringing effect at the edge of the collector plate, which tends to have a higher electric field profile [10, 22].

Though morphology remained unaffected, nanofiber diameter reductions were seen both with increasing tip-collector distance and increasing distance from the center of electrospinning. These reductions in diameter (~30 nm) however, were notably small considering standard deviations were in the range of 18 – 56 nm. Nonetheless, we confirm the reduction in nanofiber diameter is linked to increasing needle-collector distance, since the effect was evident at each individual cell. Similarly, we confirm the reduction in nanofiber diameter linked to increased distance from the center of the grid, since this trend is consistently observed in the experiments at each needle-collector distance.

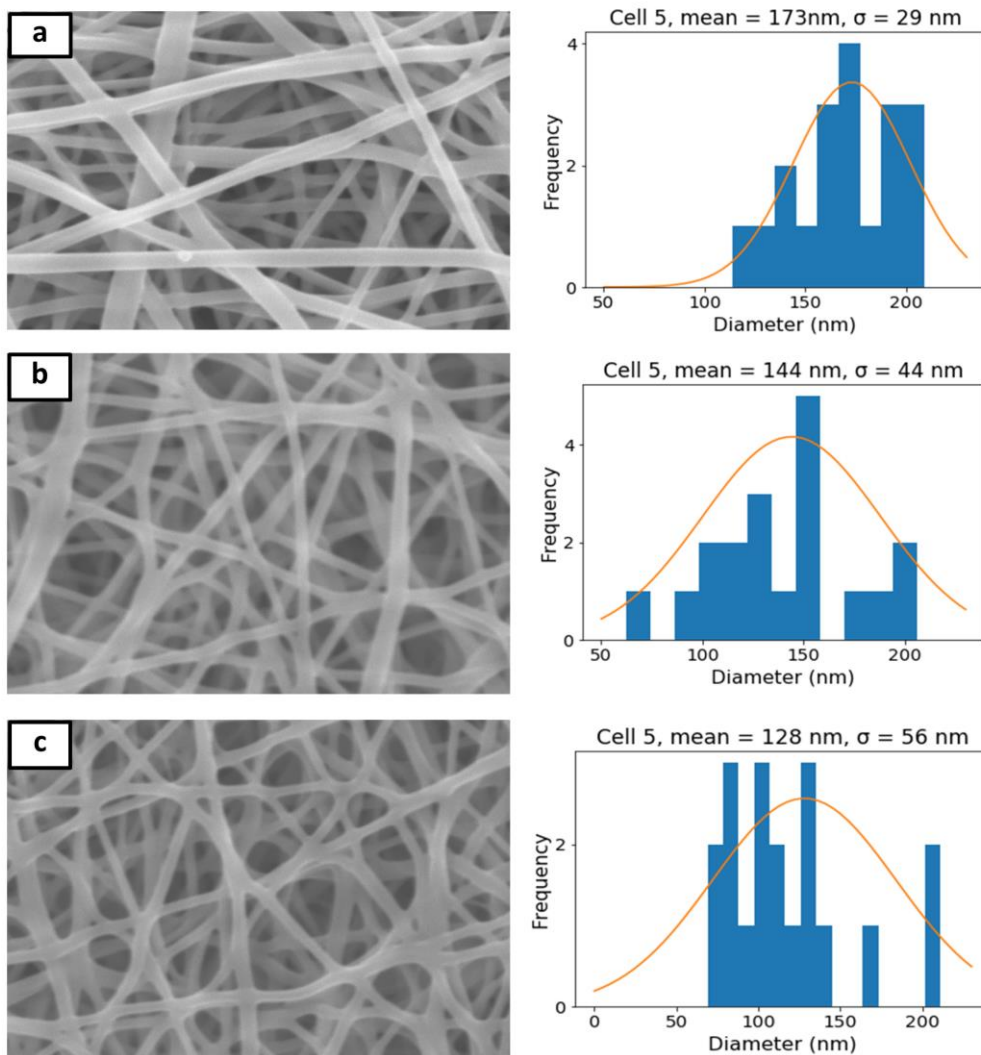


Figure 2 SEM images of nanofibers at 5 kV, 5 mm, 10 K magnification of 25 w/v% PVA electrospun nanofibers produced at a needle-collector distance of (a) 10 cm, (b) 15 cm, (c), 17 cm, at cell 5. Each alongside respective diameter distribution histograms, mean, and standard deviations

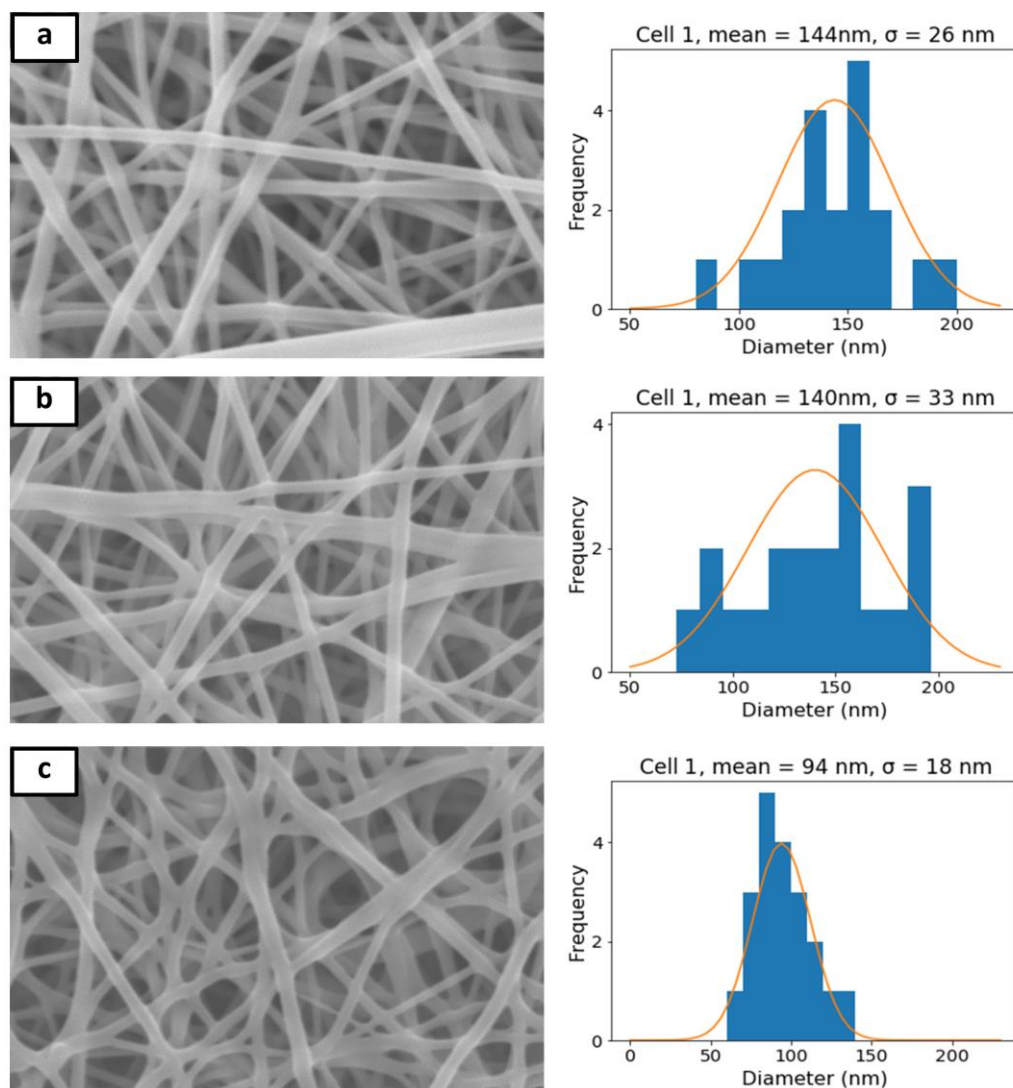


Figure 3 SEM images of nanofibers at 5 kV, 5 mm, 10 K magnification of 25 w/v% PVA electrospun nanofibers produced at a needle-collector distance of (a) 10 cm, (b) 15 cm, (c), 17 cm, at cell 1. Each alongside respective diameter distribution histograms, mean, and standard deviations

3.2 Morphology of PVA, PVA-GO and PVA-GO-PEDOT:PSS

The effect of GO and PEDOT:PSS on the morphology of PVA nanofibers was observed. The needle-to-collector distance was set at 17 cm with a pump flow rate of 0.7 ml/h. The flow rate was increased from 0.6 ml/h to 0.7 ml/h to shorten the deposition time. After the addition of GO, the PVA-GO nanofibers were thinner (197 nm, $\sigma = 97$ nm) in comparison to PVA alone (349 nm, $\sigma = 87$). Studies also showed that addition of GO produces thinner nanofibers owing to the increased charge density within the electrospun polymer jet [7, 23-25] This is caused by the extra ions made available in the solution by the addition of GO. Addition of ions increases charge density, which can result in a decrease of nanofiber diameter [8, 21]. Addition of PEDOT:PSS yielded PVA-GO-PEDOT:PSS nanofibers with mean diameter 244 nm and σ 75 nm (Figure 4 (c)); the nanofiber diameter was smaller than that of pristine PVA nanofibers under the same electrospinning conditions (mean diameter 349 nm and σ 87 nm). This

reduction in diameter is supported by prior research, which suggests that PEDOT:PSS is easily dispersed in aqueous solutions as a result of the available positive charge of p-type doped PEDOT, while the sulfonyl group of PSS acts as counter-ion [15], also increasing charge density.

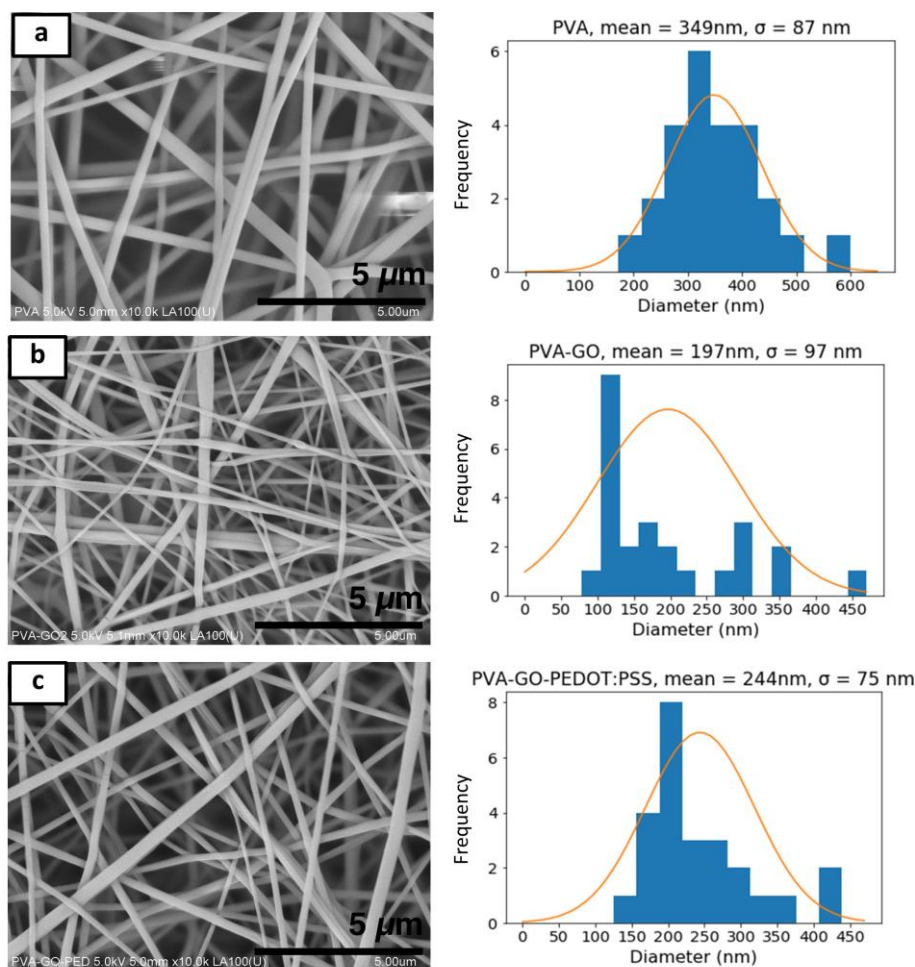


Figure 4 FESEM images of nanofibers at 5 kV, 5 mm, 10 K magnification of (a) PVA, (b) PVA-GO and (c) PVA-GO-PEDOT: PSS, each with respective diameter distribution histograms, mean, and standard deviations

3.3 Morphological Study of PVA-MWCNT

The effect of MWCNTs on the morphology of PVA nanofibers is shown in Figure 5. Needle-to-collector distance was 15 cm, voltage was 20 kV, flow rate was 0.40 ml/h, and needle-tip diameter was 1.1 mm (19 gauge). As seen in Figure 5, adding MWCNTs to PVA led to nanofibers of random diameters. Pristine PVA nanofibers were observed to have an average diameter of 180 nm and a σ of 67 nm. The observed diameters then decreased and increased in alternating fashion with increasing wt%, from 116 nm (2 wt %), to 206 nm (4 wt %), 115 nm (6 wt %), and 159 nm (10 wt %).

The pristine PVA nanofibers were beadless with diameters that appeared normally distributed (Figure 5(a)). In fact, the pristine PVA samples also showed the smallest percentage σ (mean/ σ = 37 %), meaning that the nanofiber diameters had least variation and were closest to uniformity. At 2 wt % MWCNTs, we observed thinner nanofibers with an average diameter of

116 nm, $\sigma = 61$ nm. However, many beads were visible among the nanofibers, as well as nanofibers that were twice as thick – ~ 250 nm. Correspondingly, in Figure 5(b), modal classes were seen around 90 nm, yet nanofibers from 175 - 275 nm were also observed six times from $n=50$ samples. At 4 wt % we observed the greatest average diameter of 206 nm and σ , 87 nm. The nanofibers, however, were almost beadless. The 4 % results were contrasted with the 6 wt % results; the latter had a smaller average diameter of 115 nm ($\sigma = 87$ nm), but beads of all sizes were predominant in the nanofiber structure.

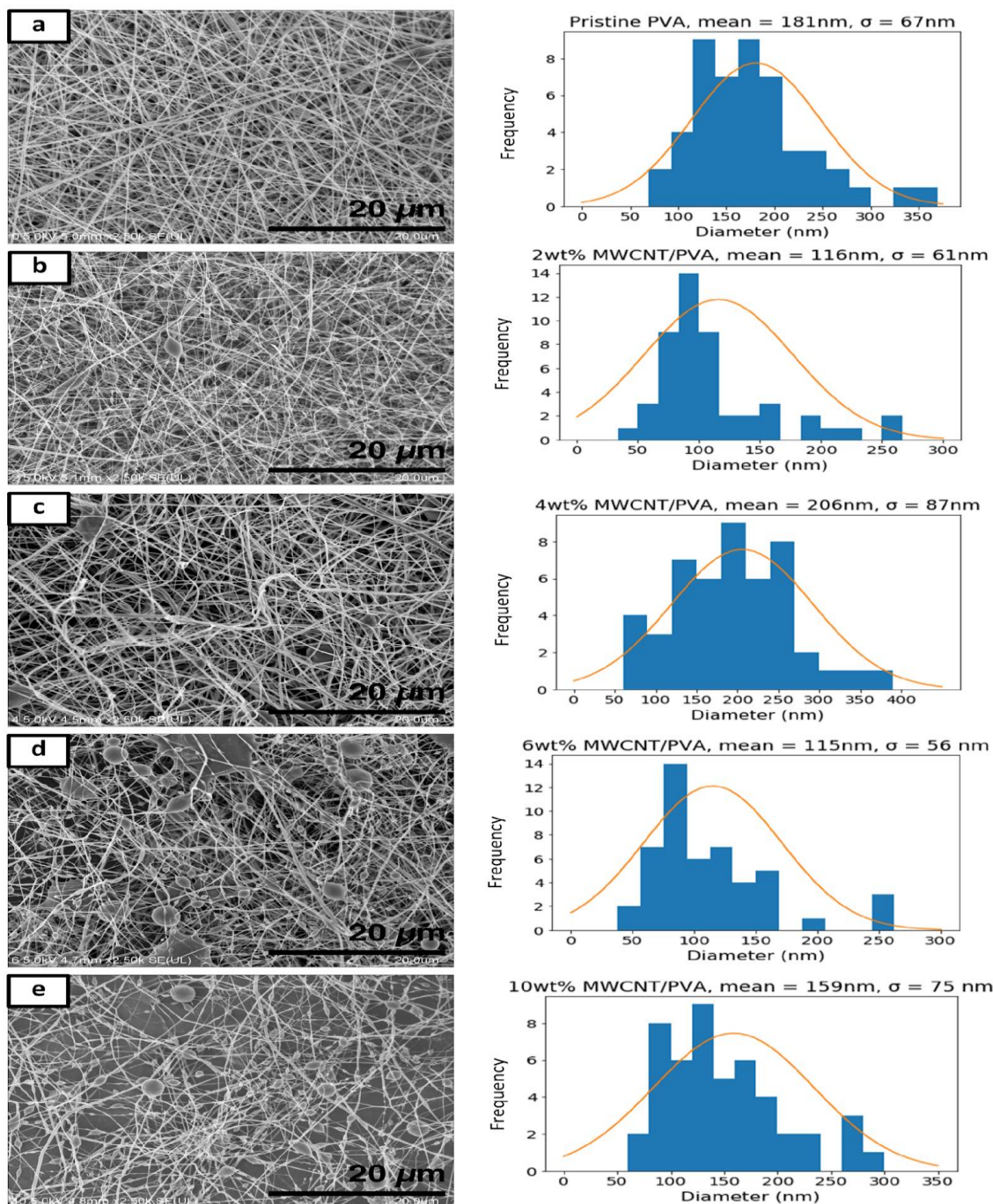


Figure 5 FESEM images of nanofibers at 2.5 K magnification of (a) pristine PVA, (b) 2 wt% MWCNTs (c) 4 wt% MWCNTs, (d) 6 wt% MWCNTs, (e) 8 wt% MWCNTs, (f) 10 wt% MWCNTs, each with respective diameter distribution histograms, mean, and standard deviations

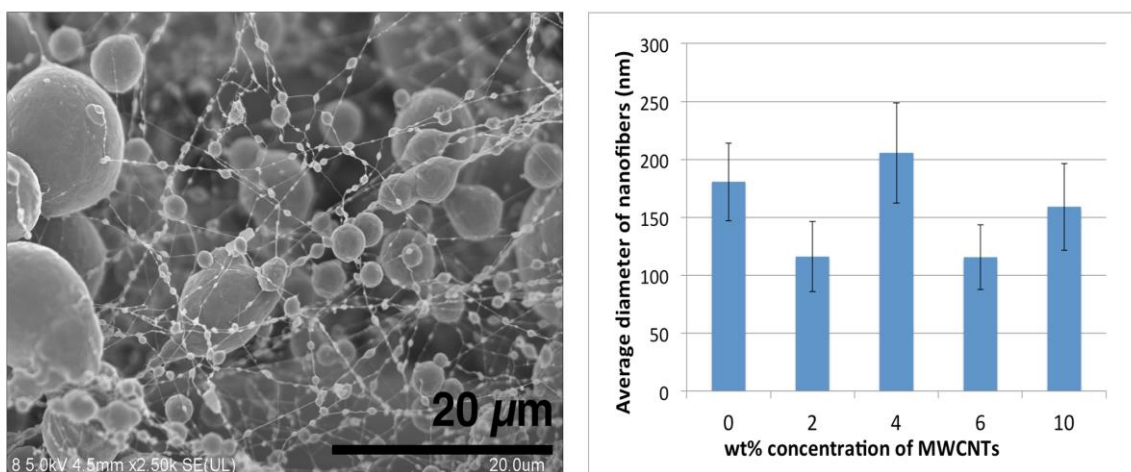


Figure 6 Trend of mean diameters of nanofibers across range of MWCNT concentrations; FESEM image of anomalous result of excessive beading at 8 wt% MWCNTs

Furthermore, at 8 wt %, as shown in Figure 6, the morphology of nanofibers was exceedingly bead-dominated; the beads observed were nearly spherical, with much thinner nanofibers between them. The much smaller scale of the nanofibers among the large beads made measuring the nanofiber diameter difficult at the FESEM magnification used. The presence of beads results from solutions of very low viscosity or low charge density, commonly described in the literature [7, 26]. Morphology at 10 wt%, however, appeared to contradict indications of low viscosity, since nanofibers were of comparable average diameter (159 nm, $\sigma = 75$ nm), as well as beads much smaller than were observed at 8 wt%, although individual nanofibers also had varying diameters along the length, indicating low viscosity.

The presence of beads in PVA-MWCNTs nanofibers could be due to MWCNT aggregation in PVA solution that resulted in PVA-MWCNT solutions of inconsistent viscosity and conductivity. In other studies, ultrasonication was performed for longer times of 1-2 hours [14, 27, 28].

4. CONCLUSIONS

Our study looked at the morphology of electrospun PVA nanofibers when combined with GO, PEDOT:PSS, and MWCNTs. The nanofiber composites showed no apparent differences in morphology, except in the case of PVA-MWCNT nanofibers, where existence of beads was obvious. Nevertheless, the addition of GO and PEDOT:PSS yields nanofibers comparatively thinner than PVA nanofibers. Our study also showed the slight (~25 nm) thinning of nanofibers at even a 2-cm radial distance from the center of a collector grid, a result of the fringing electric field. Future work should include investigation into the mechanical and electrical properties of the nanofiber composites.

Acknowledgments

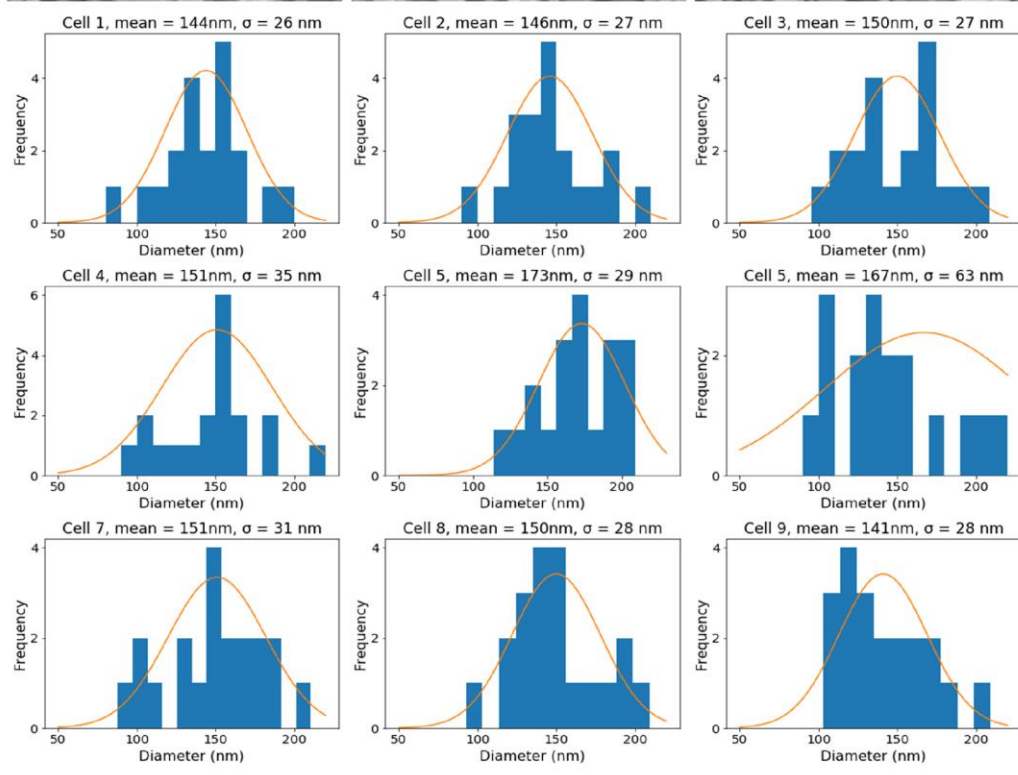
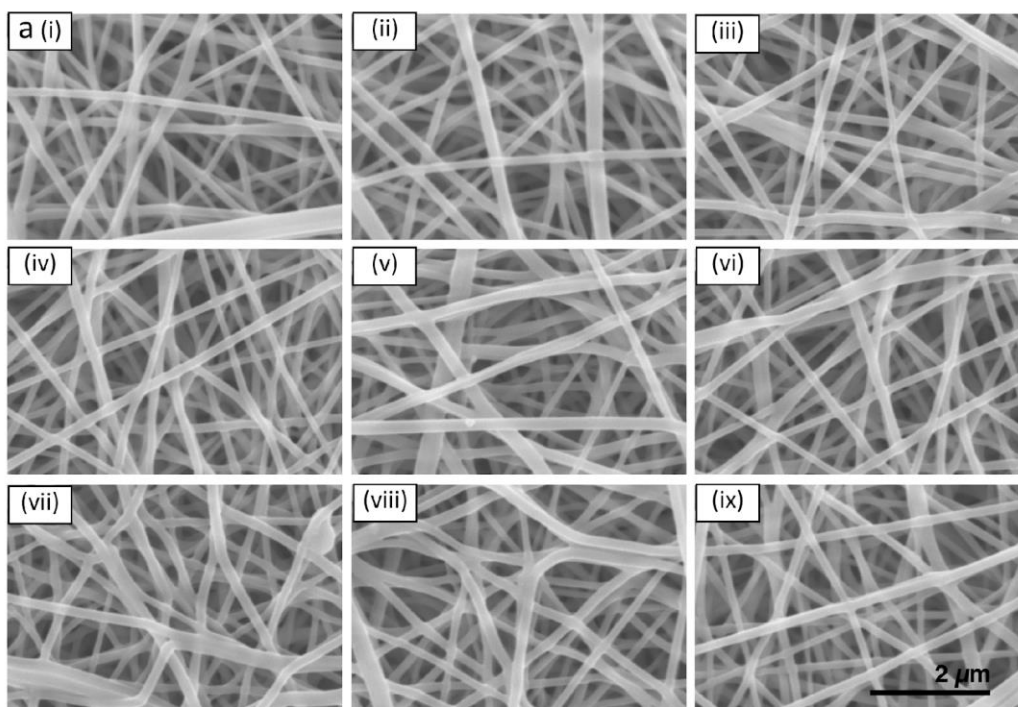
We would like to thank Final-Year Project students Muhammad Raziq Naim Ahmad Shukri and Nur Adiba Mohd Helmi for help with some experiments. Materials and equipment for the research work were funded by the Malaysia Ministry of Education, Fundamental Research Grant Scheme (FRGS17-037-0603). The publication fee was supplemented by the IIUM

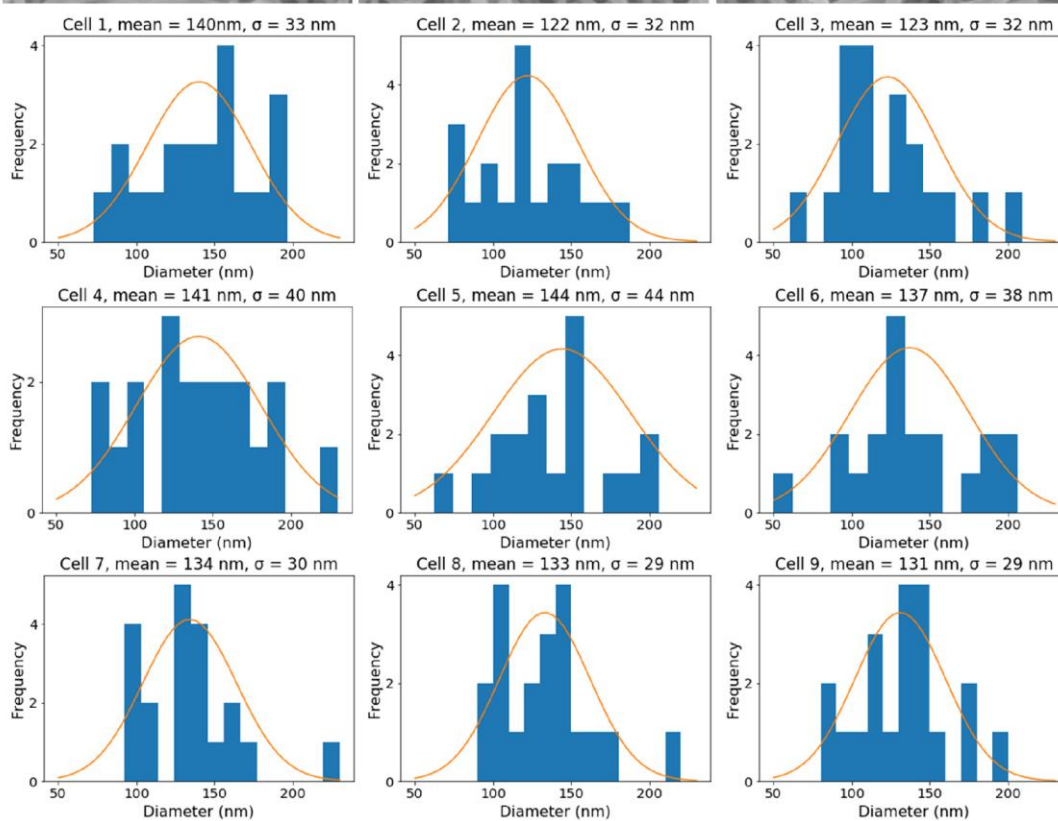
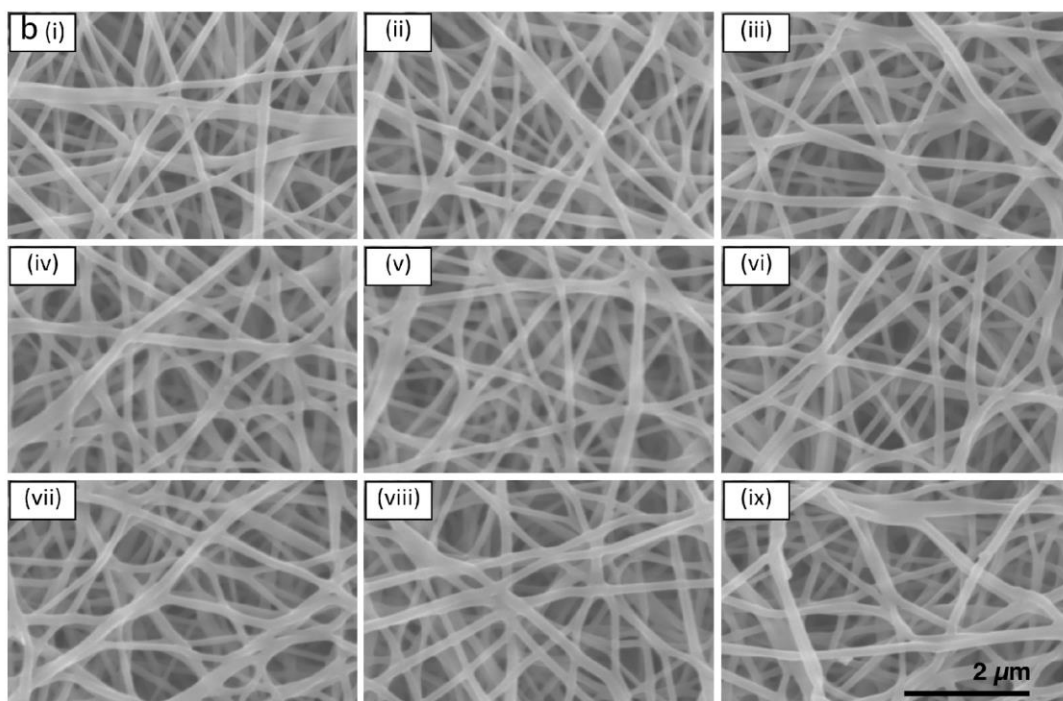
Research Postdoctoral Fellowship Scheme, grant number RPDF18-002-0002. Salary for the students working on the project was funded by FDNANO VENTURES LTD. contract research grant SP18-110-0372.

References

- [1] Q. Zhang *et al.*, (2017), *RSC Adv.*, 7 (2017) 28826
- [2] A. Luzio, E. V. Canesi, C. Bertarelli, and M. Caironi, *Materials (Basel, Switzerland)*, 7 (2014) 906
- [3] X. Liu *et al.*, *J. Power Sources*, 384 (2018) 264
- [4] O. Y. Kweon, S. J. Lee, and J. H. Oh, 10 (2018) 540
- [5] M. Gorji, R. Bagherzadeh, and H. Fashandi, *Electrospun Nanofibers* (2017) 571
- [6] T. Huang, C. Wang, H. Yu, H. Wang, Q. Zhang, and M. Zhu, *Nano Energy*, 14 (2015) 226
- [7] A. Haider, S. Haider, and I.-K. Kang, *Arab. J. Chem.*, 11 (2018) 1165
- [8] D. H. Reneker and A. L. Yarin, *Polymer (Guildf.)*, 49 (2008) 2387
- [9] A. Hassiba *et al.*, *Int. J. Nanomedicine*, 12 (2017) 2205
- [10] Z. Ding, A. Salim, and B. Ziaie, *Langmuir*, 25 (2009) 9648
- [11] S. Nivetha, R. Perumalsamy, A. Ayeshamariam, A. Mohamed Saleem, M. Karunanithy, M. Jayachandran, *Experimental and Theoretical NANOTECHNOLOGY* 3 (2019) 109
- [12] Y. Yusuf *et al.*, *AIP Conference Proceedings*, 1725 (2016) 020104.
- [13] K. J. Ramalingam, N. R. Dhineshababu, S. R. Srither, B. Saravanakumar, R. Yuvakkumar, and V. Rajendran, *Synth. Met.*, 191 (2014) 113
- [14] J. Wongon, S. Thumsorn, and N. Srisawat, *Energy Procedia*, 89 (2016) 313
- [15] Q. Zhang *et al.*, *Materials (Basel)*, 11 (2018) 1744
- [16] M. K. Leach, Z.-Q. Feng, S. J. Tuck, and J. M. Corey, *J. Vis. Exp.*, (2011) 47
- [17] T. J. Alwan, Z. Abdulahad Toma, M. A. Kudhier, and K. M. Ziadan, *Madridge J Nanotechnol Nanosci*, 1 (2016) 1
- [18] C. Mit-uppatham, M. Nithitanakul, and P. Supaphol, *Macromol. Chem. Phys.*, 205 (2004) 2327
- [19] Z. Spitalsky, D. Tasis, K. Papagelis, and C. Galiotis, *Prog. Polym. Sci.*, 35 (2010) 357
- [20] J. K. Y. Lee *et al.*, *Prog. Polym. Sci.*, 86 (2018) 40
- [21] C. J. Thompson, G. G. Chase, A. L. Yarin, and D. H. Reneker (2007) *Polymer (Guildf.)*, 48 (2007) 6913
- [22] A. Salim, C. Son, and B. Ziaie, (2008), *Nanotechnology*, 19 (2008) 375303
- [23] D. H. Reneker and I. Chun, *Nanotechnology*, 7 (1996) 216
- [24] F. Barzegar *et al.*, *J. Phys. Chem. Solids*, 77 (2015) 139
- [25] N. M. Thoppey, R. E. Gorga, J. R. Bochinski, and L. I. Clarke, *Macromolecules*, 45 (2012) 6527
- [26] H. Fong, I. Chun, and D. H. Reneker, *Polymer (Guildf.)*, 40 (1999) 4585
- [27] K. Nasouri, G. Salimbeygi, F. Mazaheri, R. Malek, and A. M. Shoushtari, *Micro & Nano Lett.*, 8 (2013) 455
- [28] O. Breuer and U. Sundararaj, *Polym. Compos.*, 25 (2004) 630

Appendix A





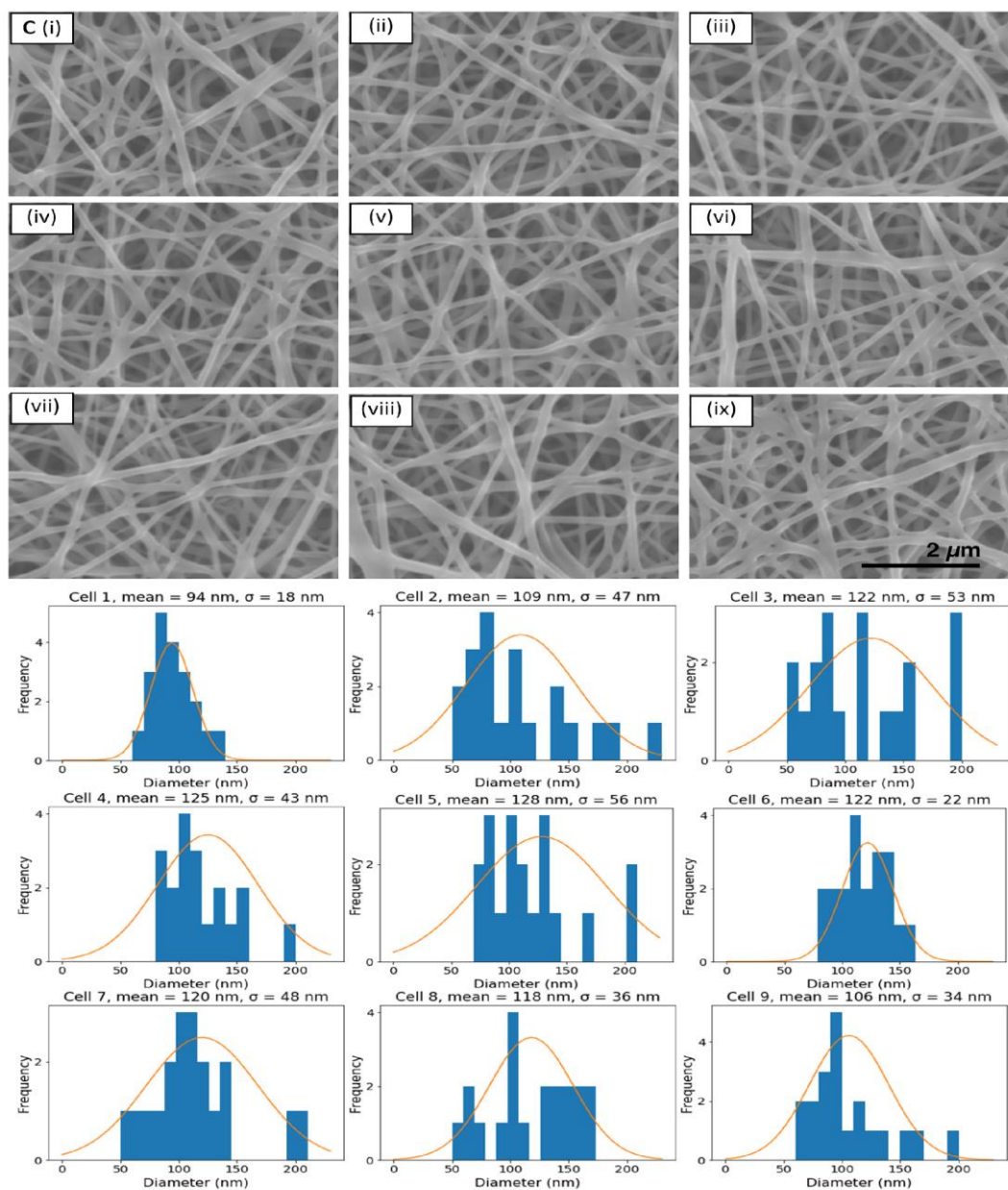


Figure Appendix SEM images of nanofibers at 5 kV, 5 mm, 10 K magnification of 25 w/v% PVA electrospun nanofibers produced at a needle-collector distance of (a (i-ix)) 10 cm, (b) (i-ix) 15 cm, (c) (i-ix) 17 cm. Each with corresponding diameter distribution histograms, mean, and standard deviation of nanofibers

Effect of some factors and variables on the frequency - time distribution of the otoacoustic emissions

Adnan AL-Maamury^{1,}, Dhifaf Ahmed²*

¹Department of Medical Physics, College of Science, Al-Karkh University of Science, Baghdad, Iraq

²Bilad Alrafidan University College, Baquba, Iraq

*E-mail: dr.almaamury@gmail.com

Received: 18/12/2019 / Accepted: 20/7/2020 / Published: 1/9/2020

The hearing process of the ear consists of two parts, the first part is related to the ear and its anatomy and the second part is related to the sound and its properties. Therefore, it is expected that there are a number of factors and variables, including those related to the ear, including sound related to the audio process. In this study, the effect of two of these factors on the otoacoustic emission is studied in general and in particular the frequency map. The relationship between frequency and quality factor is examined by changing the stimulus level.

Keywords: Hear process; Frequency map; Stimulus level; Sound.

1. INTRODUCTION

Due to high request of effective and accurate sensors, research is ongoing for new elements and methods to design and build biosensors that are based on capacitive electrodes. Common capacitive structures such as parallel plate and interdigitated electrodes (IDEs) are used widely in the literature, the first is distinguished by unpretentious design in terms of modeling [1], whereas, the second is more favored due to its effectiveness in acquiring stable and fixed temperature for the dielectric [2].

Four different electrodes models discussed thoroughly in the literature can be used as some capacitive sensors; interdigitated electrodes, spiral electrodes, meandered electrodes and serpentine electrodes. IDEs are considered for sensing; the signals have been detected by sensing materials. Analytical equations for the capacitance between electrodes fingers have been developed, which proposed a general model that can be used for any dimension and finger width as well as any number of layers with different permittivity and thickness [3]. The geometry of interdigitated schottky-barrier has been enhanced thus, the quantum efficiency and response time are analyzed and the optimum spacing for interdigitated photodetector has been identified [4]. The process of IDEs manufacturing consists of different steps of exposure, photoresist coating and etching processes using special instruments [5-10]. Therefore, many attempts have been done for simplifying the fabrication process by introducing some new and

different ones such as inkjet-printing [11-13], screen printing [14], micro fabrication [15] and stamp method [16]. IDEs have been explored extensively and used widely in many applications such as humidity sensing [17], gas sensing [18], bacteria sensing [19], pressure sensing [20], DNA sensing [21], pH sensing [22] and immunosensor [23].

The hearing process is very important to human communication in individuals [1]. Our auditory ability is due to the complex automated transmission that takes place within the inner ear that turns the waves caused by pressure into signals transmitted through the auditory nerve to the brain. Takes mechanical energy and produces electrical energy [2]. The inner ear contains an amplification system that leads to the generation of sounds within the cochlea and is transformed into the ear canal through the middle ear. These sounds are known as otoacoustic emissions (OAEs). OAE are acoustic signals generated from within the inner ear, which can be recorded in the ear canal using a sensitive microphone [3-4]. OAE are a consequence of the nonlinear and active pre-processing of sound in the cochlea [3]. OAE was first demonstrated by (David Kemp in 1978) [5]. Otoacoustic emissions have since been shown to arise through a number of different cellular and mechanical causes within the inner ear [6-7]. Studies have shown that OAEs disappear after the inner ear has been damaged, so OAEs are often used in the laboratory and clinic as a measure of inner ear health [3].

OAEs have been used to explore the differences in the auditory system between sexes, with a number of studies suggesting that females have larger OAEs than males [8-9]. There are several evidences to suggest that the outer hair cells in the human ear are enhanced by the sensitivity of the cochlea and frequency selectivity [10]. The mechanical process resulting from the transmission of sound through the ear to the movement of the tympanic membrane causes the transfer of the wave in the cochlea fluids along the basilar membrane. Therefore, the outer hair cells on the basilar membrane are part of this. This active process is emitted from an incoming signal to the auditory nerve and the incoming signal travels back to the outer ear canal through the middle ear where it can be detected¹¹. Each part of the basilar membrane has a maximum sensitivity to the frequency closer to the characteristic oval window with higher frequencies, so the high frequency responses will have the shortest time to move back to the outer ear canal.

Otoacoustic emissions are measured by a probe placed in the ear canal containing microphone that records sound in the external ear canal. TEOAE is brief acoustic stimulus with a wide frequency spectrum respond to a large part of the basilar membrane, the acoustic stimulus is used with the spectrum at a range of (1000- 4000 Hz) [11]. At high frequencies, spectroscopy of the TEOAE response can reveal cochlear damage due to noise or toxic drugs of the ear [12-13-14].

2. EXPERIMENTAL

We study here the otoacoustic emission of the ear using the nonlinear model by controlling two variables, the stimulus level and the quality factor, noting the effect of the factors on the distribution of frequency - time by studying a set of frequencies.

As in Adnan Al-Maamury (2018) [19], Adnan Al-Maamury (2015) [15] and Moleti et al. (2009) [17], we refer the nonlinear model is mathematically described as follows:

$$\frac{\partial^2 P(x, 0, t)}{\partial X^2} = \frac{2\rho}{H} \ddot{\xi}(x, t) \tag{1}$$

$$\ddot{\xi}(x, t) + \gamma_{bm} \dot{\xi}(x, t) + \omega_{bm}^2 \xi(x, t) = \frac{P(x, 0, t)}{\sigma_{bm}} \tag{2}$$

In the above equations, the fluid density is denoted as (ρ), the BM surface density is (σ_{bm}), BM transverse displacement at the longitudinal position is (x) and time is (t), and it is assumed that a cochlear duct of rectangular constant cross section of length (L) and half- height (H).

The dynamics of a passive oscillator driven by differential pressure is described by Equation (2).

The relation between longitudinal position (x), angular frequency and passive damping constant of the tonotopically resonant are set by Greenwood (1990) [18] as in Talmadge et al. (1998) [16].

$$\omega_{bm}(x) = \omega_0 e^{-k_\omega x + \omega_1} \tag{3}$$

$$\gamma_{bm}(x) = \gamma_0 e^{-k_\gamma x} + \gamma_1 \tag{4}$$

The quality factor is denoted as $Q(x)$ and the local passive quality factor is defined as:

$$Q(x) = \frac{\omega_{bm}(x)}{\gamma_{bm}(x)} \tag{5}$$

3. RESULTS AND DISCUSSION

There are some factors and variables have a clear effect on the hearing mechanism of these factors, anatomy of the ear and nature, age and other related to the sound such as the stimulus level of the sound and the quality factor.

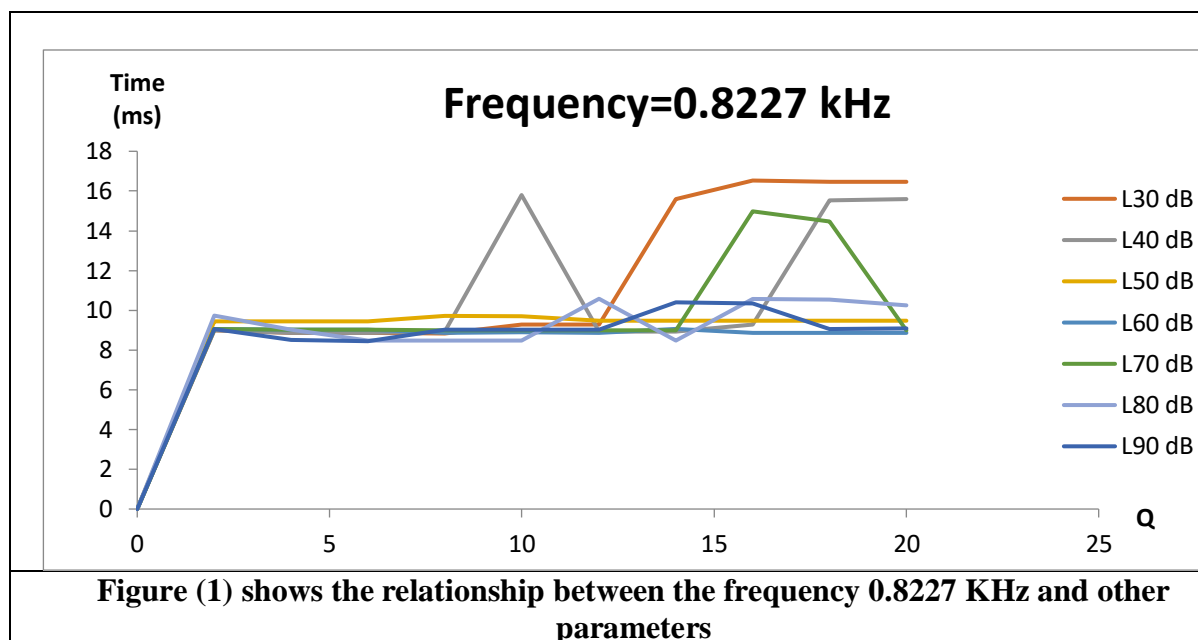
In this study, otoacoustic measurements of the ear were taken with two variables, namely the stimulus level and the quality factor to study the relationship between the auditory process represented by frequency - time distribution and the factors expected to affect the auditory process. This relationship was studied by a set of different frequencies (0.8227, 1.304, 2.067, 3.271, 4.134 and 5.197) KHz. The results of the research that obtained the of the otoacoustic emissions are presented in the form of steps and according to the selected frequencies, as follows:

First step: the frequency (0.8227 KHz)

In this case, the otoacoustic emission is studied for a different set of quality factors (2, 4, 6, 8, 10, 1, 14, 16, 18 and 20). Different stimulus levels (30, 40, 50, 60, 70, 80 and 90) dB are used for each value of the quality factor.

According to this method, arithmetic sets show the frequency-time distribution, this distribution shows the relationship between frequency and time and according to the method, it will be clear that there are some differences in time due to the effect of changing the stimulus level and the quality factor.

Figure (1) shows all the information for frequency 0.8227 KHz where it contains seven different curves each curve showing the relationship between time and quality factor. It refers to a single stimulus level, so the number of curves equals the number of stimulus levels used in the computations. It is generally concerned with frequency 0.8227 KHz and all its information. It shows the frequency-time distribution and shows the relationship between time and the quality factor. It also gives information for the frequency-time relationship by changing the quality factor and the stimulus level.

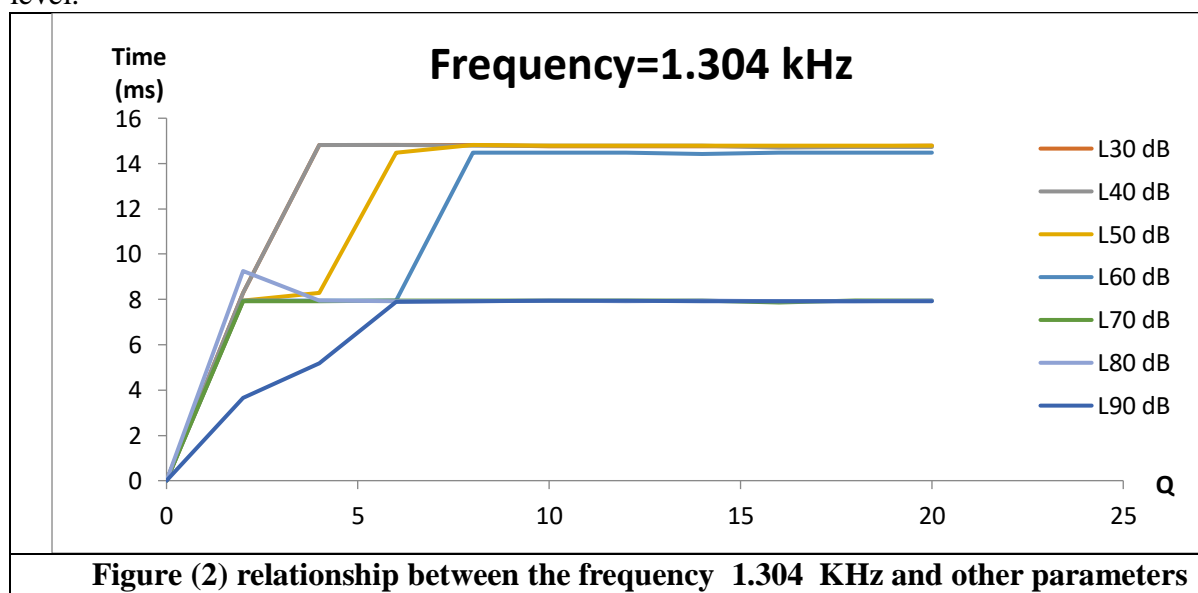


Second step: the frequency (1.304 KHz)

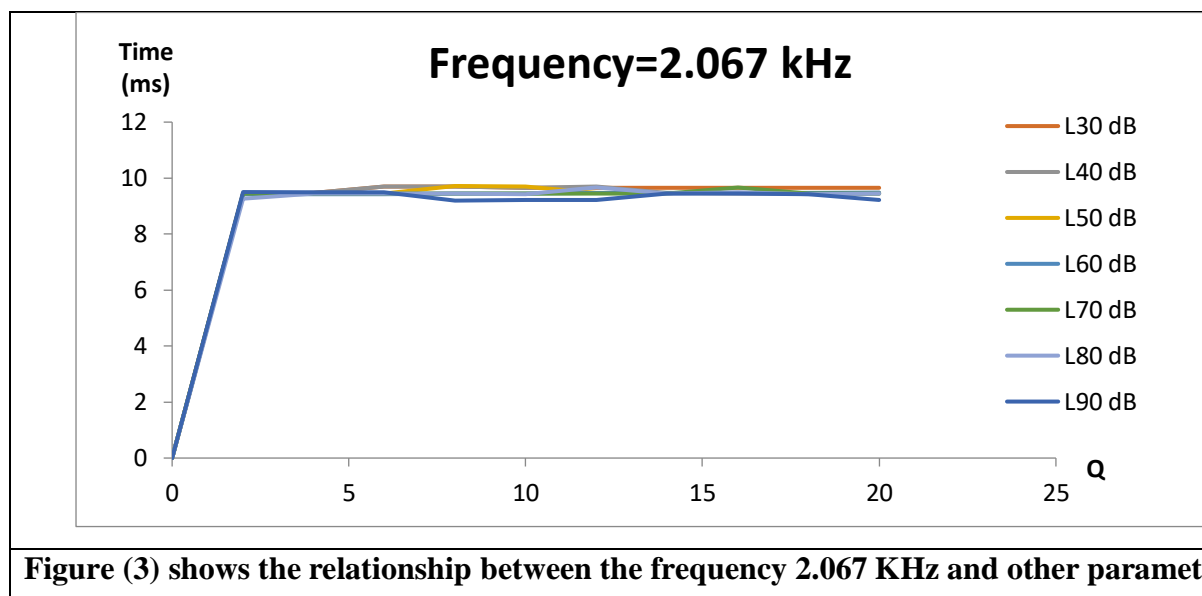
In this case and the following cases, the same technique is used in the first step to study the otoacoustic emission. The same values of the coefficient of quality and intensity levels are used in calculations.

According to the results, the frequency-time distribution shows the relationship between frequency and time and according to the method, it will be clear that there are some differences in time due to the effect of changing the stimulus level and the quality factor.

Figure (2) shows all the information for frequency 1.304 KHz where it contains seven different curves each curve showing the relationship between time and quality factor. It is generally concerned with frequency 1.304 KHz and all its information. It shows the frequency-time distribution and shows the relationship between time and the quality factor, and gives information for the frequency-time relationship by changing the quality factor and the stimulus level.



Third step: the frequency (2.067 KHz) In this case, Figure (3) shows all the information for frequency (2.067) KHz where it contains seven different curves each curve showing the relationship between time and quality factor. Each curve in the figure refers to a single stimulus level, so the number of curves equals the number of stimulus levels used in the computations. It is generally concerned with frequency (2.067) KHz and all its information. It shows the frequency-time distribution and shows the relationship between time and the quality factor. It also gives information for the frequency-time relationship by changing the quality factor and the stimulus level.



Fourth step: the frequency (3.271 KHz)

In this case, Figure (4) shows all the information for frequency (3.271 KHz) where it contains seven different curves each curve showing the relationship between time and quality factor. Each curve in the figure refers to a single stimulus level, so the number of curves equals the number of stimulus levels used in the computations. It is generally concerned with frequency (3.271 KHz) and all its information. It shows the frequency-time distribution and shows the relationship between time and the quality factor. It also gives information for the frequency-time relationship by changing the quality factor and the stimulus level.

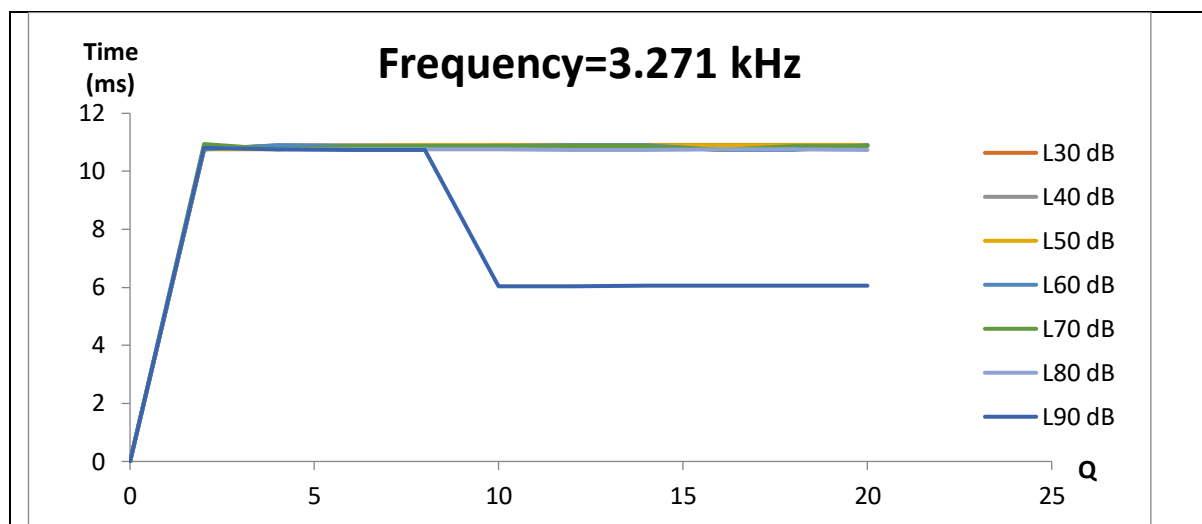
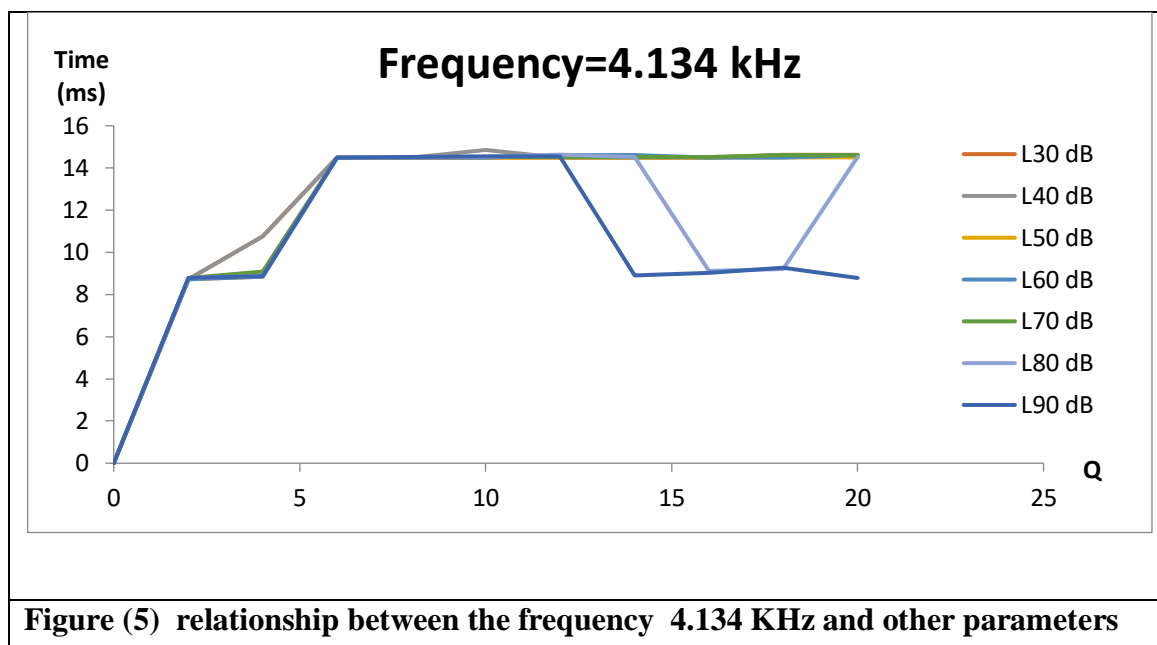


Figure (4) shows the relationship between the frequency 3.271KHz and other parameters

Fifth step: the frequency (4.134 KHz)

In this case the same technique is used to study the otoacoustic emission. According to this method, arithmetic sets show the frequency-time distribution, this distribution shows the relationship between frequency and time and according to the method, it will be clear that there are some differences in time due to the effect of changing the stimulus level and the quality factor.

Figure (5) shows all the information for frequency (4.134 KHz) where it contains seven different curves each curve showing the relationship between time and quality factor. Each curve refers to a single stimulus level, so the number of curves equals the number of stimulus levels used in the computations. It shows the frequency-time distribution and shows the relationship between time and the quality factor. It also gives information for the frequency-time relationship by changing the quality factor and the stimulus level.



Sixth step: the frequency (5.197 KHz)

The last case does not differ from all previous cases in terms of calculations, taking into account the use of two parameters, the stimulus level and the quality factor. In the otoacoustic emissions calculations, the stimulus level is changed according to the values (30, 40, 50, 60, 70, 80 and 90) dB, at the same time, the value of the quality factor (Q) is changed according to the values (2, 4, 6, 8, 10, 12, 14, 16, 18 and 20).

According to this method, arithmetic sets show the frequency-time distribution, this distribution shows the relationship between frequency and time and according to the method, it will be clear that there are some differences in time due to the effect of changing the stimulus level and the quality factor.

Figure (6) shows all the information for frequency (5.197 KHz) where it contains seven different curves each curve showing the relationship between time and quality factor. Each curve in Fig. 6 refers to a single stimulus level, so the number of curves equals the number of stimulus levels used in the computations. Finally, good information is available on the relationship between frequency, stimulus levels, quality factor and time for all cases.

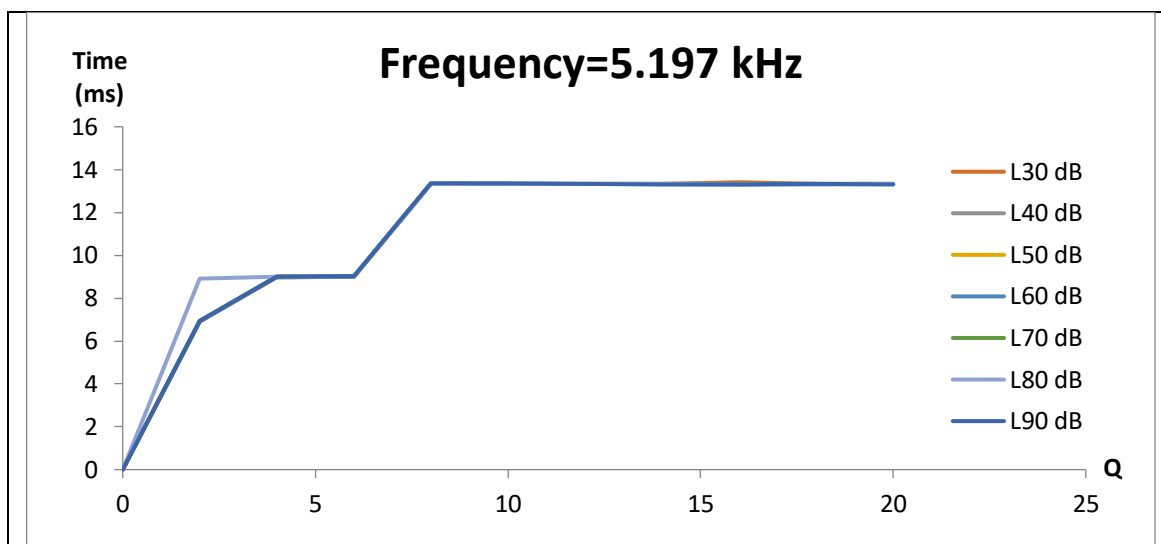


Figure (6) relationship between the frequency 5.197 KHz and other parameters

4. CONCLUSIONS

It is concluded that the quality factor and stimulus levels have a clear vary effect on the otoacoustic emission. The behavior of the quality factor and its effect on the otoacoustic emissions is based on the low and high values and the effect is clear to the low values, this result is consistent with previous studies [19-20]. In general, we believe that there are some variables have an effect on the auditory process as an example of these influential factors and variables roughness, As roughness has an effect on other transactions and variables [21]. As for the effect of the stimulus level, the behavior of the stimulus levels divided into two groups according to their effect on the otoacoustic emission, the first group is the low stimulus levels such as 30 dB and 40 dB and the second group is high stimulus levels such as 80 dB and 90 dB. For low frequencies such as 0.822 KHz, it is observed that the effect of the stimulus levels is clear, as the low levels such as 30 dB are different from the high levels in terms of the time value of the otoacoustic emission as the change in time is greater. The high stimulus levels such as 90 dB, the time of the otoacoustic emission ranges from 8 ms to 11ms for the quality factor values 2 to 20. While the time of the otoacoustic emission of the low levels ranges from 10 ms to 16 ms for the values 8 to 20 for the quality factor and similar to the high levels of values 2 to 8 for the quality factor, this situation is shared by a range of frequencies such as frequency 0.8227 KHz. As for frequencies 1.304 KHz the effect exists but is different from the previous group, the stimulus levels effect is different for the quality factor values less than 8, while the values greater than 8 have almost the same effect. The frequency 2.067 KHz is a characteristic frequency in terms of the behavior of the stimulus levels and their effect on the otoacoustic emission for all values of the quality factor. Through the results of all frequencies. For frequencies 4.134 KHz and 5.197 KHz, the change of time is from 9ms to 12ms for all levels and for almost all the values of the quality factor. According to the results obtained in this study, it is concluded that levels are classified into two categories, the first category is the low stimulus levels and the second category is the high stimulus levels. The quality factor in terms of its

values is classified into two categories: the first category is the low values and the second category is the high values. The frequencies are classified into three categories: Class I is the low frequencies; Class II is the intermediate frequencies and Class III the high frequencies. Where the frequency 2.067 KHz is the best frequency in terms of systematic results.

References

- [1] skjönsberg A. , "Hereditary susceptibility to inner ear stress agents studied in heterozygotes of the German waltzing guinea pig", Karolinska, Stockholm, Sweden (2006)
- [2] Christopher Lee Bennett, "Acquisition of Otoacoustic Emissions Using Swept-Tone Techniques", University of Miami, Scholarly Repository, PhD dissertation of Philosophy, (2010)
- [3] David I. H. Kuwano S.; Vorlander M., Handbook of signal processing in acoustics. New York, NY: Springer Verlag, (2008)
- [4] Mountain D. C., Hubbard A. E., *Hear Res.* 42 (1989) 195
- [5] Kemp D. T., *The Journal of the Acoustical Society of America* 64 (1978) 1386
- [6] J. Hamed, H. Abd, R. Muzahim, *Experimental and Theoretical NANOTECHNOLOGY* 3 (2019) 131
- [7] Kujawa S. G., Fallon M., Skellett R. A., and Bobbin R. P., *Hearing research* 97 (1996) 153
- [8] McFadden D., et al " Sex differences in distortion-product and transient-evoked otoacoustic emissions compared". *J. Acoust. Soc. Am* 125 (2009) 239
- [9] McFadden D., *Archives of Sexual Behavior* 31 (2002) 99
- [10] Lilaonitkul W. Guinan jr. *Journal of Neurophysiology.* (March 2009)
- [11] Kemp D. T., *British Medical Bulletin* 63 (2002) 223
- [12] Hoben R., Easow G., Pevzner S., Parker MA. *Front Neurosci*; 11 (2017) 157
- [13] Al-Noury K. *Laryngoscope*; 12 (2011) 1081
- [14] Inger Uhlén MD., OTOACOUSTIC EMISSIONS (OAEs), OPEN ACCESS GUIDE TO AUDIOLOGY AND HEARING AIDS FOR OTOLARYNGOLOGISTS, PhD. Department of Audiology & Otoneurology .Karolinska University Hospital & CLINTEC .Karolinska Institute, Stockholm, Sweden. (2017)
- [15] Al-Maamury A. M. *Elixir Phys. & Anatomy* 80 (2015) 31062
- [16] Talmadge C. L., Tubis A., Long G. R., and Piskorski P., *J. Acoust. Soc. Am.* 104 (1998) 1517
- [17] Moleti A., Paternoster N., Bertaccini D., Sisto R., and Sanjust F., *J. Acoust. Soc. Am.* 126 (2009) 2425
- [18] D. D. Greenwood, *J. Acoust. Soc. Am.* 87 (1990) 2592
- [19] AL-Maamury A. M., *International Journal of Applied Engineering Research* 13 (2018) 10205
- [20] AL-Maamury A. M. Dhifaf A. *Research in Otolaryngology* 6 (2017) 47
- [21] AL-Maamury A. M. Al-Rawi F. Q., Al-Rubaiee A. A, *Indian Journal of Public Health Research and Development* 10 (2019) 652

Thinning energy effect on the fluctuations of charged particles lateral distribution produced in extensive air showers

Hassanen Abdulhussaen Jassim, A. A. Al-Rubaiee*, Iman Tarik Al-Alawy

College of Science, Department of Physics, Mustansiriyah University, Baghdad, Iraq

*E-mail: dr.rubaiee@uomustansiriyah.edu.iq

Received: 11/11/2019 / Accepted: 1/5/2020 / Published: 1/9/2020

In this work, the effects of the extensive air showers (EAS) were described by estimating the lateral distribution function (LDF) at very high energies of various cosmic ray particles. LDF was simulate for charged particles such as the electron and positron pair production, gamma, muons and all charged particles at very high energies 10^{16} , 10^{18} and 10^{19} eV. The simulation was performed using AIRES air shower simulator system version 2.6.0. The effect of primary particles, energies, thinning energy and zenith angle (θ) on the charged LDF particles produced in the EAS was taken into account. The comparison of the estimated LDF of the charged particles such as the electron and positron pair production and muons with the simulated results by Sciutto and experimental results by Yakutsk EAS observatory gives good acceptance at 10^{19} eV for zenith angles 0° and 10° .

Keywords: Extensive air showers; Lateral distribution function; AIRES; Thinning; Fluctuations.

1. INTRODUCTION

Extensive air showers are a cascade of electromagnetic radiation and ionized particles produced in the atmosphere through the interaction of primary cosmic ray with the atom's nucleus in the air producing a huge amount of secondary particles such as X-ray, electrons, neutrons, muons, alpha particles, etc [1]. In 1930, Pierre Victor Auger, the French physicist, discovered the EAS by producing more and more particles in the atmosphere [2]. The LDF of the charged particle in the EAS is a quantity required for observations of Earth's cosmic radiation, which are often derived from EAS observables [3]. The parameter used to describe the shape of the lateral structure density is the lateral shape parameter in the NKG function "Nishimura-Kamata-Greisen function" [4, 5].-EAS develops in a convoluted way as a combination of electromagnetic and hadronic showers. It is important to achieve a detailed numerical simulation of the EAS to infer the properties of the primary cosmic radiation, produced by it. The number of charged particles in ultra-high energy EAS may be enormous and may exceed 10^{10} , so these processes require highly complex computing resources to

understand and simulate them [6]. Since the shower growth is a complicated random process, Monte-Carlo simulation is often used to design atmospheric showers [7]. Among the many ways to simplify the problem and to reduce computation time, the thinning approximation is the most common entirety of the importance. It's essential idea is to track only a representative set of particles. While they are highly effective in calculations and provide the right values for observation on average, this method offers artificial fluctuations because the number of tracked particles decreases by several orders of magnitude. These artificial fluctuations are combined with natural fluctuations and thus reduce the precision of determination of physical parameters [8]. In 2007, Kuzmin studied no-thinning simulations of EAS and small-scale fluctuations at ground level [9]. In 2009, Bruijn studied statistical thinning with a full simulated of air showers at very high energies [10]. In 2015, Alex Estupiñan studied the achievement of the de-thinning method order to simulate EAS for high-energy cosmic rays [11]. Ivanov recently (in 2018), studied the distribution of the zenith angle of cosmic ray showers measured with the Yakutsk array and its application to the analysis of access trends in the equatorial coordinates [12].

The results of the current calculations have shown the effect of thinning energy on the fluctuations in the density of charged particles reaching the Earth's surface, such as the pair production of electron and positron, gamma, muons and all charged particles, by simulating the LDF carried out using the Monte Carlo AIRES system at ultrahigh energies 10^{16} , 10^{18} and 10^{19} eV. The estimated LDF comparison of charged particles such as the electron and positron pair production and muons with simulated results by Sciutto and Yakutsk EAS observatories gives good approval at 10^{19} eV with thinning energies ($\epsilon_{th}=10^{-6}$ and 10^{-7})[13, 14].

2. LATERAL DISTRIBUTION FUNCTION

LDF of charged particles in the EAS is a significant amount of ground monitoring of cosmic radiations, through which most the cascade observables are deduced [15]. A study of EAS can be done experimentally on the Earth's surface, underground and in many mountains that rise by identifying some LDF quantities. i.e. the density of charged particles that originate in the EAS as a function of the basic distance of the shower core or in other words, the LDF is the shower structure of the cascade at different depths in the atmosphere [2]. The expression that is widely used to describe the LDF form is the NKG function that is presented through the forum [4]:

$$\rho(r) = \frac{N_e}{2*\pi*R_M^2} * C(s) * \left(\frac{r}{R_M}\right)^{(s-2)} * \left(\frac{r}{R_M} + 1\right)^{(s-4.5)} \tag{1}$$

Where $\rho(r)$ is the particle density on the distance r from the shower core, N_e is the total number of shower electrons, $R_M = 118$ m is Molier radii, s is the shower age parameter, and $C(s)$ is the normalizing factor of $0.366 s^2 * (2.07 - s)^{1.25}$ [16].

3. THINNING METHOD

The implementation of the thinning algorithm is used by simulating the shower on secondary particles if this condition is satisfied[11]:

$$E \circ \epsilon_{th} > \sum_{j=1}^n E_j \tag{2}$$

where E_j is the secondary particle energy, E_0 is the energy of the primary particle and $\epsilon_{th} = E_j/E_0$ is defined as the level of thinning. In this case, there is only one secondary particle i can survive. The survival probability is:

$$P_i = E_i / \sum_{j=1}^n E_j \tag{3}$$

Otherwise, if the total amount of secondary particles n is greater than the thinning energy threshold, i.e.:

$$E_0 \epsilon_{th} < \sum_{j=1}^n E_j \tag{4}$$

Then the secondary particle with energy below the thinning threshold will survive with a probability:

$$P_i = E_i / E_0 \epsilon_{th} \tag{5}$$

4. RESULTS AND DISCUSSION

4.1 Simulating of LDF using AIRES system

AIRES is an acronym for AIR-shower Extended Simulations, which is defined as a set of programs and subroutines that are used to simulate EAS particle cascades, which initiated after interaction of primary cosmic radiations with high atmospheric energies and the management of all output associated data. AIRES provides a complete space-time particle propagation in a real medium, where the features of the atmosphere, the geomagnetic field, and Earth's curvature are adequately taken into account [13].

The thinning algorithm (statistical sampling step) is used when the number of particles in the showers is very large. The thinning algorithms used in AIRES are localized, i.e. statistical samples never change the average values of the output observables. There are many particles that are taken into account through simulations using the AIRES system such as: "electrons, positrons, gammas, muons, and all charged particles". The primary particle of the incident in the EAS may be a primary proton or iron nuclei or other primaries mentioned in the AIRES guidance document with a very high primary energy that may exceed 10^{21} eV [13].

Figure 1 shows the density of several secondary particles as a function of the distance from the shower axis that reaches the Earth's surface by AIRES simulation. The effect of the primary particles (proton and iron), energies (10^{16} , 10^{18} and 10^{19} eV), zenith angles ($\theta = 0, 10, 30$ and 45 degrees) and the average of thinning energies ($\epsilon_{th} = 10^{-3}, 10^{-4}, 10^{-6}$ and 10^{-7}) on the density of charged particles produced in the EAS was taken into consideration. As shown in figure 1, the density of several secondary particles decreases with increasing distance from the shower axis. Finally, the statistical fluctuations of LDF of several secondary particles decrease while reducing the thinning energy.

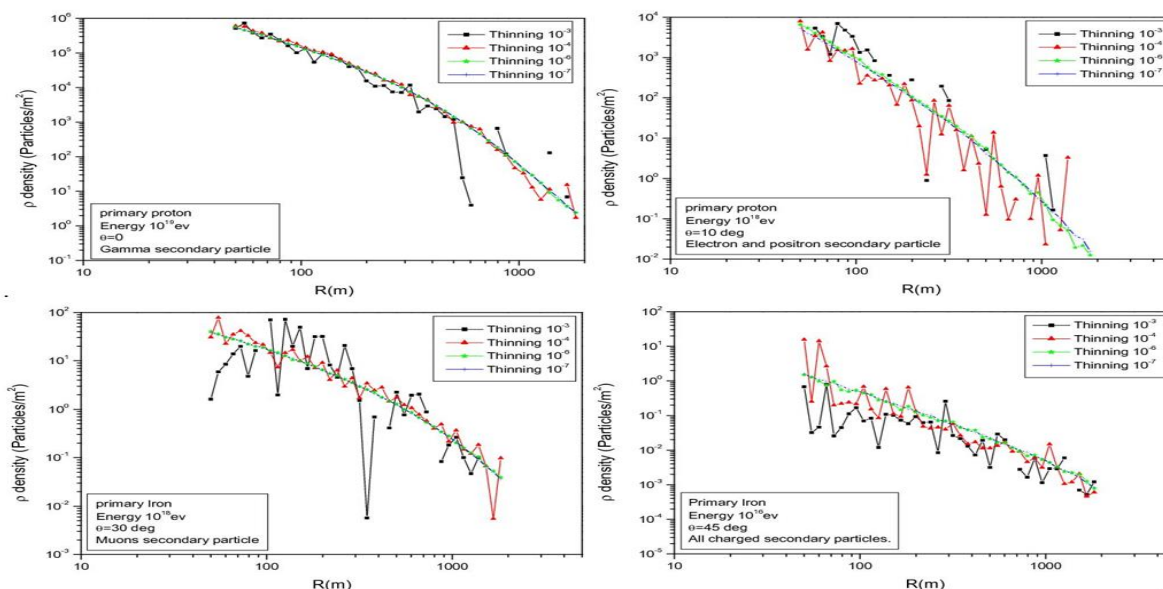


Figure 1 The effect of thinning energy on secondary particle densities of primary p and Fe at different zenith angles ($\theta = 0^\circ, 10^\circ, 30^\circ$ and 45°) and different energies ($10^{16}, 10^{18}$ and 10^{19} eV).

4.2 Comparison with the experience of Sciutto and Yakutsk Observatory

Figure 2 demonstrates the comparison between the present results of LDF that performed by AIRES simulation (solid lines) with the results simulated by Sciutto (triangle symbols) [13]. This figure displayed good agreement between the secondary particles (electron and positron) and the muons particles initiated by the primary proton at energy 10^{19} eV with thinning energies ($\epsilon_{th}=10^{-6}, 10^{-7}$) and the vertical EAS showers.

The Yakutsk EAS array studies the very high energy cosmic radiations, which occurs in the field of astrophysics, that is, an important area in physics. There are two main goals for construction of the Yakutsk EAS Observatory; the first is the elementary particles that verify the cascades that initiated by the primary particles in the atmosphere. The second goal is to reconstruct the astrophysical characteristics of primary particles such as: “mass composition, energy spectrum, intensity and their origin”[14].

Figure 3 shows the comparison between the present results and the experimental data obtained by the Yakutsk Observatory [14]. The curves in this figure displayed a good agreement for (electron and positron) and muons particles, which were initiated by primary proton at energy 10^{19} eV and a slanted EAS showers with $\theta = 10^\circ$.

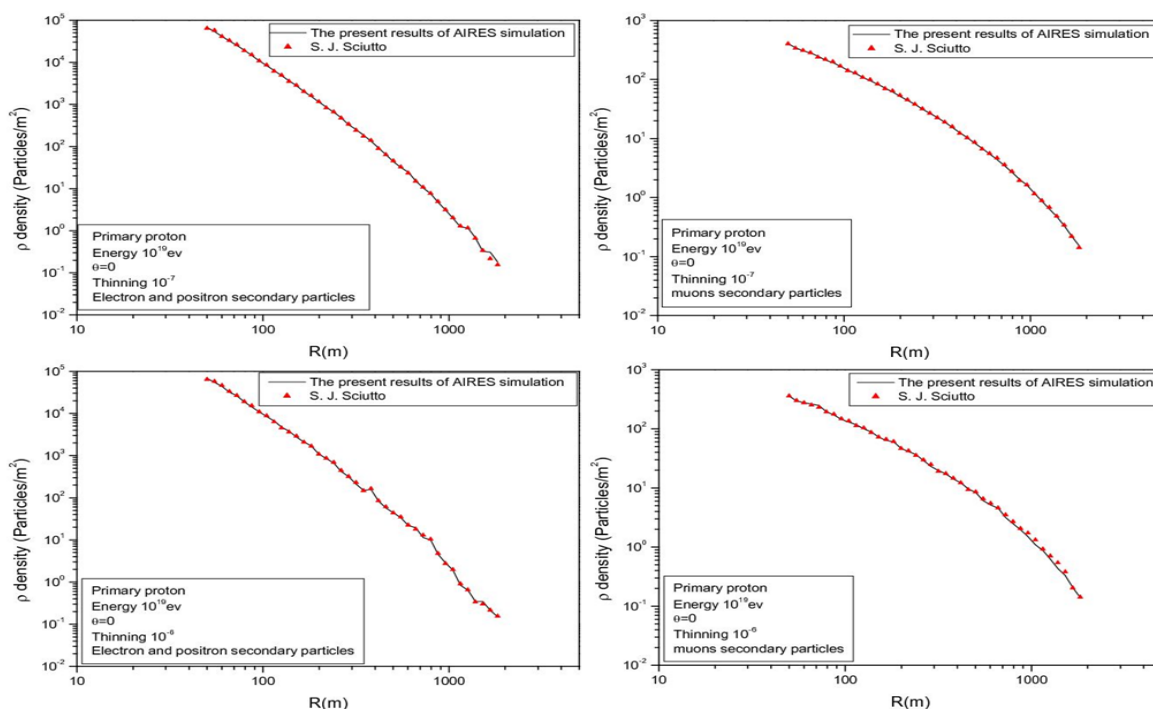


Figure 2 Comparison between the present results of LDF simulation by the AIRES system with the results simulated by Sciutto for primary proton at 10^{19} eV with ($\epsilon_{th}=10^{-6}$ and 10^{-7}) for secondary particles (electron and positron) and muons.

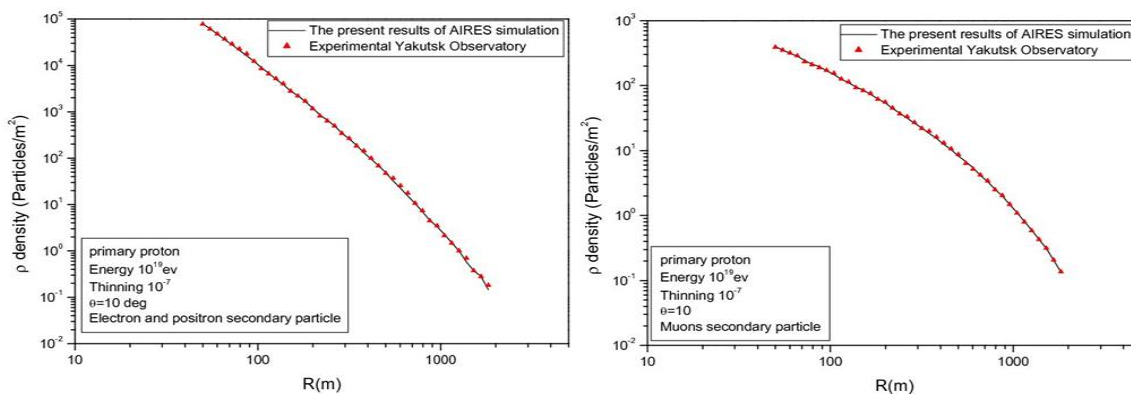


Figure 3 Comparison between the present results of LDF simulation by the AIRES system with the experimental data obtained by Yakutsk Observatory for primary proton at 10^{19} eV for secondary particles (electron and positron) and muons.

5. CONCLUSIONS

In the present work, the lateral distribution function of charged particles using the AIRES system for two primary particles (proton and iron nuclei) was simulated in different ultrahigh energies 1016, 1018 and 1019 eV. Simulation lateral structure of the charged particle demonstrates the ability for distinguishing the primary cosmic ray particle and its energy. The statistical fluctuations of LDF of several secondary particles decrease with decreasing the thinning energy. An important feature of the present work is the creation of a library of Lateral structure samples that can be used to analyze real EAS events that have been detected and registered in EAS arrays.

The introduced results using AIRES system are identified with Yakutsk experimental data, proving that AIRES provides an environment suitable for studying high-energy cosmic rays. Therefore, charged particles reaching the Earth's surface have many effects on weather, human health and other effects.

ACKNOWLEDGMENT

Authors would like to thank Mustansiriyah University (www.uomustansiriyah.edu.iq) Baghdad-Iraq for its support in the present work.

References

- [1] P. Billoir, *Astroparticle Physics*, 30 (2008) 270
- [2] S. Bhatnagar, *Physics Education* 33(2009) 249
- [3] A. Haungs, H. Rebel, M. Roth, *Reports on Progress in Physics* 66 (2003) 1145
- [4] K. Kamata, J. Nishimura, *Progress of Theoretical Physics Supplement* 6 (1958) 93
- [5] K. Greisen, *Annual Review of Nuclear Science* 10 (1960) 63
- [6] J. Matthews, *Astroparticle Physics* 22 (2005) 387
- [7] D. Gorbunov, G. Rubtsov, S.V. Troitsky, *Physical Review D* 76 (2007) 043004
- [8] Tagreed K. Hamad, Alaa H. Ali, Alaa J. Ghazai, Hussein T. Salloom, *Experimental and Theoretical NANOTECHNOLOGY* 3 (2019) 149
- [9] V.A. Kuzmin, G.I. Rubtsov, *JETP Letters* 85 (2007) 535
- [10] R. Bruijn, J. Knapp, I. Valiño, *Study of statistical thinning with fully-simulated air showers at ultra-high energies* (2009)
- [11] A. Estupiñán, H. Asorey, L.A. Núñez, *Nuclear and Particle Physics Proceedings* 267 (2015) 421
- [12] A. Ivanov, *Physical Review D* 97 (2018) 083003
- [13] S. Sciutto, *AIRES User's Manual and Reference Guide*, version 2.6, in, (2002)
- [14] S. Knurenko, A. Ivanov, M. Pravdin, A.V. Sabourov, I.Y. Sleptsov, *Nucl.Phys.Proc. Suppl.* 581 (2008) 175
- [15] A. Tapia, D. Melo, F. Sanchez, A.S. Croce, A. Etchegoyen, J. Figueira, R. Gamarra, B. GARCIA, N. González, M. Josebachuili, *Braz. J. Phys.* 44 (2014) 415
- [16] S. Hayakawa, *Cosmic Ray Physics*, Interscience Monographs and Texts in Physics and Astronomy, Wiley-Interscience (1969)

AUTHOR GUIDELINES FOR JOURNAL ARTICLE

Introduction

This document enables the user to have a better understanding of rules and regulations used for writing journals. However, each institute has its own template so it is advised that after writing any journal or publication, refer to your specific institute references for writing journals and publications.

Format

All files should be submitted as a Microsoft Word Document.

Article Length

Articles should usually be between **4000 and 10000 words** in length. This includes all text including references and appendices. Please allow roughly **280 words** for each figure or table.

Article Title

A title of not more than **16 words** is advised.

Article Title Page

An Article Title Page should be submitted alongside each individual article using the template provided.

This should include:

- Article Title
- Author Details (see below)
- Acknowledgements
- Author Biographies
- Structured Abstract (see below)
- Keywords (see below)
- Article Classification (see below)

Author Details

Details should be supplied on the Article Title Page including:

- Full name of each author
- Affiliation of each author, at time research was completed
- Where more than one author has contributed to the article, details of who should be contacted for correspondence
- E-mail address of the corresponding author

Structured Abstract

Authors should supply a structured abstract on the Article Title Page, set out under 4-7 sub-headings:

- Purpose (mandatory)
- Design/methodology/approach (mandatory)

- Findings (mandatory)
- Research limitations/implications (if applicable)
- Practical implications (if applicable)
- Social implications (if applicable)
- Originality/value (mandatory)

Maximum should roughly be **250** words in total (including keywords and article classification).

Keywords

You should provide up to **10 keywords** on the Article Title Page, which encapsulate the principal topics of the paper.

Article Classification

Categorize your paper on the Article Title Page, under one of these classifications:

- Research paper
- Viewpoint
- Technical paper
- Conceptual paper
- Case study
- Literature review
- General review.

Headings

Headings should be concise, with a clear indication of the distinction between the hierarchies of headings.

The preferred format is for first level headings to be presented in bold format and subsequent sub-headings to be presented in medium italics.

Notes/Endnotes

Notes or Endnotes should be used only if absolutely necessary and must be identified in the text by consecutive numbers, enclosed in square brackets and listed at the end of the article.

Research Funding

Authors must declare all sources of external research funding in their article and a statement to this effect should appear in the Acknowledgements section. Authors should describe the role of the funder or financial sponsor in the entire research process, from study design to submission.

Figures

All Figures (charts, diagrams, line drawings, web pages/screenshots, and photographic images) should be submitted in electronic form.

All Figures should be of high quality, legible and numbered consecutively Graphics may be supplied in color to facilitate their appearance on the online database.

□ Figures created in Microsoft Word, Microsoft PowerPoint, Microsoft Excel and Illustrator should be supplied in their native formats. Electronic figures created in other applications should be copied from the origination software and pasted into a blank Microsoft Word document or saved and imported into an Microsoft Word document or alternatively create a .pdf file from the origination software.

□ Figures which cannot be supplied in as the above are acceptable in the standard image formats which are: .pdf, .ai, and .eps. If you are unable to supply graphics in these formats then please ensure they are .tif, .jpeg, or .bmp at a resolution of at least 300dpi and at least 10cm wide.

□ To prepare web pages/screenshots simultaneously press the "Alt" and "Print screen" keys on the keyboard, open a blank Microsoft Word document and simultaneously press "Ctrl" and "V" to paste the image. (Capture all the contents/windows on the computer screen to paste into Microsoft Word, by simultaneously pressing "Ctrl" and "Print screen".)

Photographic images should be submitted electronically and of high quality. They should be saved as .tif or .jpeg files at a resolution of at least 300dpi and at least 10cm wide. Digital camera settings should be set at the highest resolution/quality possible.

Tables

Tables should be typed and included in a separate file to the main body of the article. The position of each table should be clearly labelled in the body text of article with corresponding labels being clearly shown in the separate file.

Ensure that any superscripts or asterisks are shown next to the relevant items and have corresponding explanations displayed as footnotes to the table, figure or plate.

References

References to other publications must be in Harvard style and carefully checked for completeness, accuracy and consistency. This is very important in an electronic environment because it enables your readers to exploit the Reference Linking facility on the database and link back to the works you have cited through CrossRef.

You should cite publications in the text, for example: (Adams, 2006) using the first named author's name or (Adams and Brown, 2006) citing either names of two, or (Adams et al., 2006), when there are three or more authors. At the end of the paper a reference list in alphabetical order should be supplied:

References for Books

For books you should follow below template:

Surname, Initials (year), Title of Book, Publisher, Place of publication.

References for Book Chapters

For book chapters you should follow below template:

Surname, Initials (year), "Chapter title", Editor's Surname, Initials, Title of Book, Publisher, Place of publication, pages.

e.g. Calabrese, F.A. (2005), "The early pathways: theory to practice – a continuum", in Stankosky, M. (Ed.), *Creating the Discipline of Knowledge Management*, Elsevier, New York, NY, pp. 15-20

References for Journals

For journals you should follow below template:

Surname, Initials (year), "Title of article", Journal Name, volume, number, pages.

e.g. Capizzi, M.T. and Ferguson, R. (2005), "Loyalty trends for the twenty-first century", *Journal of Consumer Marketing*, Vol. 22 No. 2, pp. 72-80.

References for Published Conference Proceedings

For journals you should follow below template:

Surname, Initials (year of publication), "Title of paper", in Surname, Initials (Ed.), Title of published proceeding which may include place and date(s) held, Publisher, Place of publication, Page numbers.

e.g. Jakkilinki, R., Georgievski, M. and Sharda, N. (2007), "Connecting destinations with an ontology-based e-tourism planner", in *Information and communication technologies in tourism 2007 proceedings of the international conference in Ljubljana, Slovenia, 2007*, Springer-Verlag, Vienna, pp. 12-32.

References for Unpublished Conference Proceedings

For unpublished conference proceedings you should follow below template:

Surname, Initials (year), "Title of paper", paper presented at Name of Conference, date of conference, place of conference, available at: URL if freely available on the internet (accessed date).

e.g. Aumueller, D. (2005), "Semantic authoring and retrieval within a wiki", paper presented at the European Semantic Web Conference (ESWC), 29 May-1 June, Heraklion, Crete, available at:<http://dbs.uni-leipzig.de/file/aumueller05wiksar.pdf> (accessed 20 February 2007).

References for Working Papers

For Working Papers you should follow below template:

Surname, Initials (year), "Title of article", working paper [number if available], Institution or organization, Place of organization, date.

e.g. Moizer, P. (2003), "How published academic research can inform policy decisions: the case of mandatory rotation of audit appointments", working paper, Leeds University Business School, University of Leeds, Leeds, 28 March.

References for Encyclopedia Entries (no author or editor)

For encyclopedia entries you should follow below template:

Title of Encyclopedia (year) "Title of entry", volume, edition, Title of Encyclopedia, Publisher, Place of publication, pages.

e.g. Encyclopaedia Britannica (1926) "Psychology of culture contact", Vol. 1, 13th ed., Encyclopaedia Britannica, London and New York, NY, pp. 765-71.

References for Newspaper Articles (non-authored)

For Newspaper Articles you should follow below template:

Newspaper (year), "Article title", date, pages.

e.g. Daily News (2008), "Small change", 2 February, p. 7.

References for Electronic Sources

If it is available online, the full URL should be supplied at the end of the reference, as well as a date that the resource was accessed.

e.g. Castle, B. (2005), "Introduction to web services for remote portlets", available at: <http://www-128.ibm.com/developerworks/library/ws-wsrp/> (accessed 12 November 2007).

Standalone URLs, i.e. without an author or date, should be included either within parentheses within the main text, or preferably set as a note (Roman numeral within square brackets within text followed by the full URL address at the end of the paper).

For more information

Contact us:

The Scientific Institute for Advanced Training and Studies

Email: publisher@siays.co.uk

Phone: (0060) 11 113 331 80

WhatsApp & viber

Facebook: <https://www.facebook.com/siats.mutamd?ref=bookmarks>

Experimental and Theoretical NANOTECHNOLOGY

<http://etn.siats.co.uk>

Guidelines link: <http://www.siats.co.uk/author-guidelines-for-journal-article/>

Content

1. TiO ₂ NANORODS WITH CDS QUANTUM DOTS FOR OPTICAL APPLICATIONS.....	167
2. SOLAR ENERGY HARVESTING EFFICIENCY OF NANO-ANTENNAS.....	179
3. SYNTHESIS AND CHARACTERIZATION OF ZNO NANOFLOWERS UNDERTEMPERATURE EFFECT.....	189
4. OPTICAL AND STRUCTURAL OF NANOCRYSTALLINE CDS.....	201
5. OPTICAL PROPERTIES OF REDUCED GRAPHENE OXIDE SHEETS.....	209
6. PREPARATION, ANALYSIS AND CHARACTERIZATION OF ITO NANOSTRUCTURES.....	217
7. ANALYSIS AND CHARACTERIZATION OF ZNO NANOWIRES FOR SENSING APPLICATIONS.....	227
8. MORPHOLOGY OF ELECTROSPUN PVA NANOFIBERS ENHANCED WITH GRAPHENE OXIDE, POLY (3,4-ETHYLENEDIOXYTHIOPHENE): POLYSTYRENE SULFONATE (PEDOT:PSS) AND MULTIWALLED CARBON NANOTUBES.....	235
9. EFFECT OF SOME FACTORS AND VARIABLES ON THE FREQUENCY - TIME DISTRIBUTION OF THE OTOACOUSTIC EMISSIONS.....	249
10. THINNING ENERGY EFFECT ON THE FLUCTUATIONS OF CHARGED PARTICLES LATERAL DISTRIBUTION PRODUCED IN EXTENSIVE AIR SHOWERS.....	259